

Magnetic trapping
for an atom-chip-based gravimeter

Von der QUEST-Leibniz-Forschungsschule der
Gottfried Wilhelm Leibniz Universität Hannover

zur Erlangung des akademischen Grades

Doktor der Naturwissenschaften

– Dr. rer. nat. –

genehmigte

Dissertation

von

Dipl.-Phys. Jonas Matthias

2020

Referent: Prof. Dr. rer. nat. Ernst Maria Rasel
Institut für Quantenoptik
Leibniz Universität Hannover

Korreferent: Dr. rer. nat. Dennis Schlippert
Institut für Quantenoptik
Leibniz Universität Hannover

Korreferent: Assoc. Prof. Dr. rer. nat. Rainer Helmut Dumke
Division of Physics and Applied Physics
Nanyang Technological University

Tag der Promotion: 4. November 2020

Abstract

In the past century, the development of gravimeters with low uncertainty and long-term stability has led to new fields of research in geodesy and geoscience. Decreasing the instrumental measurement uncertainty further will enable observations of previously inaccessible phenomena, for instance, mass transport in hydrology and volcanology. During the last decades, quantum sensors based on the interference of cold atoms have been developed. Using a cold atomic gas as test mass, the accuracy of these sensors is not limited by mechanical properties but by effects caused by the thermal expansion of the atomic ensemble. The application of ultra-cold atomic ensembles with lower expansion rates in atom interferometer gravimeters is projected to reduce the leading order uncertainties by more than an order of magnitude. At the same time, atom chip technology makes it possible to prepare ultra-cold atomic ensembles at a high repetition rate and to miniaturise the sensor size. These advancements promise the realisation of an absolute gravimeter with unprecedented accuracy.

This thesis describes the design considerations and the assembly of the transportable Quantum Gravimeter (QG-1) based on light-pulse atom interferometry of Bose-Einstein condensates (BEC) prepared on an atom chip. It is estimated, that the two leading order uncertainties of systematic biases governing the instrumental measurement uncertainty of current generation cold atom gravimeters are reduced to less than 1 nm/s^2 in the QG-1 apparatus. The established design of an atom-chip-based BEC source pioneered in the QUANTUS collaboration is modified to meet the requirements of QG-1. A free optical aperture of 18 mm for the interferometry laser beam is realised by changing the orientation of the atom-chip-based BEC source. Therefore, a new layout of the mesoscopic wire structure of the atom chip is required. The design described in this thesis enables atom interferometry with a free falling test mass with a baseline of 330 mm. The retro-reflection mirror is placed inside the vacuum chamber to eliminate optical elements in the atom interferometer beam path. It is mounted on a custom designed tip/tilt-stage with compact size and a large dynamic range of up to a hundredfold of the Earth's rotation rate for characterisation. Furthermore, a compact, robust and transportable fibre based laser system with modular electronics and a computer control system are set up.

The key result of this thesis is the reliable operation of the ultra-cold atomic source on the atom chip. After optimisation of the trap loading procedure for a high atom number and low excitation of oscillations, it was shown that the necessary design change of the atom chip allows for efficient operation. The compressed magnetic trap has a geometrically averaged trap frequency of $2\pi \cdot 256 \text{ Hz}$ and the trapped ensemble has a lifetime of 3.2 s. The evaporative cooling procedure starts with $3.3 \cdot 10^7$ atoms at a temperature of $166 \mu\text{K}$. Within 1.3 s, or 2.3 s for the complete sequence, 3000 atoms are prepared at a temperature of 160 nK close to the critical temperature for Bose-Einstein condensation.

Key words: atom chip, atom interferometry, gravimetry

Contents

1	Measuring gravity	1
1.1	Gravimeters in geodesy and geoscience	2
1.2	State-of-the-art classical gravimeters	2
1.3	State-of-the-art atom gravimeters	3
1.4	Next generation quantum gravimeter	4
1.5	This thesis	5
I	A transportable gravimeter with unprecedented accuracy	7
2	Considerations for the gravimeter design	9
2.1	Measurement principle	9
2.2	Measurement bias and measurement uncertainty	10
2.3	Sagnac effect and Coriolis bias	11
2.4	Wave front bias	12
2.5	Conclusions on the gravimeter design	14
3	Sensor head	17
3.1	In-vacuum reference mirror assembly	18
3.2	High-flux source of ultra-cold atoms	21
3.3	Mirror coating on the atom chip	22
3.4	Laser beam collimation for the interferometry light grating	23
3.5	Vacuum chamber	24
3.6	Absorption detection system	24
3.7	Magnetic shield	25
4	Laser system	27
4.1	Spectroscopy reference module	27
4.2	High-power laser and distribution module	29
4.3	Generation of laser frequencies for Bragg diffraction	30
4.4	Generation of laser frequencies for atom cooling	30

5	Control electronics	31
5.1	Electronic stack for the laser system	31
5.2	Temperature stabilisation	35
5.3	Current driver stack	35
5.4	FPGA for analogue signals	41
5.5	Transportable rack	41
5.6	Computer control	41
II	Magnetic trapping	43
6	Atom-chip-based magnetic traps	45
6.1	Magnetic trapping of neutral atoms	45
6.2	Atom chip	46
6.3	Simulation	47
7	Loading of the magnetic trap	51
7.1	Optical state preparation	51
7.2	Mode matching	52
7.3	Temperature in the magnetic trap	54
7.4	Loading efficiency and saturation of the magnetic trap	55
8	Trap characterisation	57
8.1	Lifetime of the trapped ensemble	57
8.2	Eigenfrequencies	58
8.3	Summary	60
9	Evaporative cooling	61
9.1	Radio frequency spectroscopy	62
9.2	Peak density of a Gaussian distribution	63
9.3	Optimisation of the forced evaporation procedure	64
III	Conclusion	69
10	Summary and outlook	71
	Bibliography	77
	List of Figures	85
	List of Tables	87

A Appendix	89
A.1 Mirror surface flatness measurements	89
A.2 Ultra-high vacuum initialisation	91
Publications	93
Curriculum Vitae	95

CHAPTER 1

Measuring gravity

Every child notices that loose objects fall towards the surface of the Earth. Galileo Galilei claimed that this effect is caused by a constant acceleration independent of the mass of the object. He measured this acceleration by letting spheres roll down a ramp and marking their position after equal time intervals. The distance travelled during a certain number of time intervals followed a simple rule, it was proportional to the square of the number of time intervals. Galilei empirically proved that spheres with different weights are subject to the same acceleration regardless of their mass [Dra73; Mac12]. Today, this law of nature is written as follows: For a body at rest at time $t = 0$ and under constant acceleration a , the position x after the elapsed time t is given as

$$x(t) = \frac{1}{2} a \cdot t^2. \quad (1.1)$$

From observations of the movement of the planets in the solar system, Sir Isaac Newton derived the law of universal gravitation. The gravitational attraction between two masses m_1 and m_2 with distance r is expressed as the force

$$F = G \frac{m_1 m_2}{r^2} \quad (1.2)$$

with the gravitational constant G . The gravitational acceleration a_{grav} of mass m_1 by the mass of the Earth $m_2 = m_{\text{Earth}}$ is given by

$$a_{\text{grav}} = \frac{F}{m_1} = G \frac{m_{\text{Earth}}}{r^2}. \quad (1.3)$$

It is inversely proportional to the square of the distance r^2 . Therefore, the value of local gravity is lower for larger distances to the centre of the Earth, e.g. on a mountain. Furthermore, gravity measurements are influenced by masses that are close to the test mass m_1 . Thus, environmental processes can be studied by observing gravity changes. The definition of gravity not only includes the gravitational acceleration but also inertial forces from the rotation of the Earth. It reads as follows:

Gravity is the magnitude of the gravity acceleration experienced by a body at the Earth surface resulting from the gravitational attraction of the Earth, the Sun, the Moon, and the planets and from the centrifugal effect associated with the Earth rotation. [Cam17]

A device to measure local gravity is called gravimeter.

1.1 Gravimeters in geodesy and geoscience

Since Galilei, measurement techniques improved over time and gravimeters became an important tool for various observations in geodesy and geoscience. To study local phenomena, tidal effects and polar motion are modelled and subtracted from the recorded gravity signal. A comprehensive overview can be found in [Cam17] including several examples: By measuring gravity one can study ice mass changes, ground deformation and ground water resources. The ability of gravimeters to record underground mass transport is for instance useful for volcanology and earth quake research.

Gravimetry is a unique tool for the verification of models of the dynamic Earth. One example is the fennoscandian land uplift area, which has been the subject of several studies. The land uplift is caused by the relaxation of the Earth's crust since the last ice age, when fennoscandia was covered by glaciers. After the ice melted and its weight has been released, the land is rising as studied by various means, e.g. observation of the sea level at the coast. Via measurements by the global navigation satellite system (GNSS) the rate of land uplift has been determined to be around 10 mm per year depending on the location. This would lead to a decrease of gravity of 3.1 nm/s^2 per mm. Dynamic Earth models predict a reflow of magma under the uplift region, which leads to an increase of gravity of 1.4 nm/s^2 per mm. Therefore, the gravity change predicted by these models is a decrease of 1.7 nm/s^2 per mm. This trend has been observed and verified by measuring gravity with a classical FG-5 gravimeter at several locations over the course of five years [Tim11].

1.2 State-of-the-art classical gravimeters

Gravimeters developed for applications in geosciences fall into one of two categories: absolute and relative gravimeters. *Absolute gravimeters* track the motion of a free-falling test mass and derive a value for the vertical acceleration, whereas *relative gravimeters* record the vertical force exerted by gravity. The following classical gravimeters represent the state-of-the-art.

In an *absolute gravimeter* of the type Micro-g LaCoste FG5-X, based on the JILAg gravimeter developed by Jim Faller et al. at JILA, the free-fall of a glass prism is tracked with a laser interferometer. At the end of the measurement the prism is decelerated by a cage which moves synchronously with the prism during free-fall and moves the prism to the starting position afterwards. The release of the prism is adjusted to avoid rotations as any tilting would introduce systematic errors in the measurement.

The setup of free-fall absolute gravimeters has been optimised over decades to reach a reproducibility¹ of 20 nm/s². But the accuracy is ultimately limited by the mechanical nature of the measurement principle. The mechanical mechanism also limits the measurement time. Since the device has to be serviced and re-calibrated every few thousand drops it cannot be operated continuously.

For a continuous recording of changes in gravity, *relative gravimeters* are employed in geodetic observatories worldwide. The test mass is either suspended by a spring or a diamagnetic superconductor is levitated by a magnetic field. As gravity changes, the position of the test mass inside the gravimeter housing will change. But it is held in place by either an electrostatic or a magnetic force controlled via a feedback loop. The exerted force follows and compensates the changing gravitational force. Therefore, the electronic output signal of the feedback controller is recorded as the gravimeter signal. Because the devices drift on longer timescales they need to be periodically calibrated with an absolute gravimeter and are thus called ‘relative’.

For the characterisation and correction of the instrumental drift of a relative gravimeter, an absolute gravimeter needs to periodically measure side-by-side. Superconducting relative gravimeters show a typical instrumental drift of 10 nm/s² per year. The uncertainty of the correction is governed by the uncertainty of the absolute gravimeter. Therefore the sensitivity to signals on timescales longer than one year is only as good as the best absolute gravimeter.

1.3 State-of-the-art atom gravimeters

Light-pulse atom interferometers [Kas91] represent a novel type of absolute gravimeter. Similar to classical absolute gravimeters the position of a free-falling atomic ensemble is tracked in terms of the wavelength of a laser light field. So far, atoms prepared by laser cooling in a magneto-optical trap (MOT) [Raa87] were mainly exploited. The atomic ensemble is released by switching off the magnetic and optical fields of the trap. A cloud of up to one billion rubidium atoms has a weight of less than one picogram which thus has a negligible mechanical influence on the device. This setup does not require any moving parts and therefore eliminates the main systematic effects of mechanical absolute gravimeters. It also allows long-term operation without mechanical wear. While in a classical absolute gravimeter the test mass acts as a mirror for a light wave, in an atom gravimeter the light field acts as a grating deflecting the wave function of the atomic ensemble.

Atom gravimeters are starting to become commercially available, e.g. the Muquans Absolute Quantum Gravimeter (AQG) [Mén18]. They combine the advantages of classical absolute and relative gravimeters in one instrument and promise to offer a simplification in operation for geodesists. While an FG5-X gravimeter needs to be set up by a trained operator during several hours, the manufacturer of the AQG states that it does not need manual alignment or

¹ The data sheet states this value as ‘accuracy’ defined as ‘observed agreement between FG5-X instruments’.

assembly and features an automatic alignment procedure that takes one hour [muQ19]. Atom gravimeters can operate continuously with low maintenance needs and they are currently deployed on relevant remote measurement sites [Ant18].

The uncertainty demonstrated by cold atom gravimeters of 40 nm/s^2 [Fan16; Fre16; Lou11] is comparable to that of state-of-the-art classical absolute gravimeters. It is, however, limited due to systematic effects caused by the horizontal velocity and the thermal expansion of the cold atomic gas used as test mass during the measurement with a typical temperature of $2 \mu\text{K}$ [Lou11; Sch15]. As a result, the current generation of atom gravimeters presents no improvement in accuracy compared to classical devices.

To improve accuracy, the obvious solution is to reduce the temperature of the cold atomic gas further. With temperatures of the atomic ensemble down to 50 nK , KARCHER et al. [Kar18] obtained a reduced uncertainty of 13 nm/s^2 in the evaluation of the wave front bias.

1.4 Next generation quantum gravimeter

Using the technique of evaporative cooling, trapped atomic ensembles have been cooled towards the quantum mechanical ground state of motion [And95; Bra95; Dav95]. In a Bose-Einstein condensate (BEC) the atomic ensemble does not have a thermal distribution of kinetic energy, as all particles occupy the ground state. The expansion rate after release from the trap is caused by the mean-field energy of the trapped ensemble which is defined by the trap geometry. The expansion rate can be reduced further by applying the so called "delta-kick" collimation method [Amm97; Myr00]. After release the trap potential is switched on for a period of time as short as $100 \mu\text{s}$. This transient potential acts like a three-dimensional lens for the expansion of the atomic ensemble and reduces the expansion rate further. The effect on the ballistic expansion is analogous to a lens collimating an expanding optical beam. Hence, this method is also referred to as magnetic lens. Expansion rates equivalent to effective temperatures as low as 1 nK have been demonstrated [Kru14].

The preparation of a BEC in a transportable device operating on geodetic measurement sites has been made possible by advances in atom chip technology. In the QUANTUS and MAIUS collaboration, miniaturised BEC machines have been developed for atom optical experiments in microgravity environments such as the Bremen drop tower at the Centre of Applied Space Technology and Microgravity (ZARM) [Mün13], sounding rockets [Bec18] or the international space station [Fry19]. These atom-chip-based BEC sources with cycle times as low as 1 s [Rud15] are an ideal platform for the development of a next generation quantum gravimeter.

1.5 This thesis

The subject of this thesis is the development, assembly and characterisation of the next generation quantum gravimeter QG-1.

Part I describes the setup of this gravimeter which is designed to reduce the systematic uncertainty compared to state-of-the-art atom gravimeters. In [chapter 2](#) the measurement principle of the gravimeter is summarised and it is estimated to which extent an ultra-cold atomic ensemble from an atom-chip-based source reduces the wave front bias and the Coriolis bias, the two major contributions to the systematic uncertainty. The design and assembly of the gravimeter sensor head employing an atom-chip is described in [chapter 3](#). [Chapter 4](#) introduces the laser system designed for this transportable device, while [chapter 5](#) features the electronic modules needed to power the laser system and to run a measurement cycle in the sensor head.

Part II details the preparation of ultra-cold atomic ensembles in a magnetic trap on the atom chip. In [chapter 6](#) methods for the trapping of atoms on an atom chip are introduced. The loading of the atom-chip-based trap is characterised in [chapter 7](#) while [chapter 8](#) examines the trap properties. The implementation and results of the evaporative cooling are described in [chapter 9](#). Finally, a conclusion and an outlook are given in [chapter 10](#).

Part I

A transportable gravimeter with unprecedented accuracy

CHAPTER 2

Considerations for the gravimeter design

The design of QG-1 aims to reduce the instrumental uncertainty compared to current-generation cold atom gravimeters. The thermal expansion and the transversal centre-of-mass motion of the atomic ensemble will be reduced by preparing an ultra-cold atomic ensemble in a magnetic trap on an atom chip. In this chapter it will be estimated, to which extent this improved concept reduces the Coriolis bias (section 2.3) and the wave front bias (section 2.4), the two major contributions to the instrumental uncertainty of state-of-the-art atom gravimeters.

2.1 Measurement principle

A constant acceleration of a test mass can be measured by recording its position at three points in time equally spaced by the duration T . This is the foundation of the atom interferometric measurement and was also used by classical absolute gravimeters in the 1960s [Coo65, pp. 102–106]. While state-of-the-art classical gravimeters record the interferometer signal continuously it is worthwhile to discuss the outdated measurement method because the implementation details, as for instance the influence of a gravity gradient and the effective measurement height, have been extensively studied on classical gravimeters and also apply to gravimeters based on atom interferometry [Rot12]. In a classical absolute gravimeter, gravity is measured by tracking the position of a glass prism in free fall with a laser interferometer. For a constant acceleration a the position is given as

$$z(t) = z_0 + v_0 \cdot t + \frac{1}{2} a \cdot t^2. \quad (2.1)$$

The acceleration of the test mass can be derived from position measurements at the points in time 0, T and $2T$ as

$$a \cdot T^2 = z(0) - 2z(T) + z(2T). \quad (2.2)$$

In this formula the initial position $z(0) = z_0$ and the initial velocity v_0 drop out. The position z is measured in terms of the laser wavelength λ . A movement in z direction Δz results in an

optical path length difference $2 \cdot \Delta z$. The phase of the laser interferometer changes as

$$\Delta\varphi = 2 \cdot \Delta z \cdot k \quad (2.3)$$

with the wave vector $k = 2\pi/\lambda$. The light intensity at one interferometer output is recorded with a photodiode resulting in a sinusoidal signal. The number of periodic fringes is counted and one complete fringe of the interferometer output intensity is a phase 2π . The acceleration can now be calculated from the accumulated phase

$$a \cdot 2k \cdot T^2 = \varphi(0) - 2\varphi(T) + \varphi(2T) \quad (2.4)$$

In gravimeters based on atom interferometry, position measurements of the free falling test mass are performed in terms of the wavelength of a laser light field, too. Two light fields with wave vectors k_1 and k_2 are retro-reflected on a reference mirror and form a light grating. The atomic wave function is diffracted on the grating by either a Bragg [Deb11] or Raman [Kas92] process. The atom interferometer is realised by three light pulses equally spaced by the duration T splitting, deflecting and recombining the atomic wave function. Each light pulse imprints a position dependent phase. The interferometer has two output states and each state consists of a combined wave function of the two paths. The occupation probability of the interferometer output states is modulated by the accumulated phase $\Delta\Phi$ in the interferometer which is given as [Kas92, eqn. 14]

$$\Delta\Phi = \varphi(0) - 2\varphi(T) + \varphi(2T) \quad (2.5)$$

By observing the number of atoms in both output states, the occupation probability and hence the accumulated phase $\Delta\Phi$ is derived. Analogous to the light interferometer follows from equation (2.2) that the atom interferometer phase is sensitive to a constant acceleration a

$$a \cdot k_{\text{eff}} \cdot T^2 = \Delta\Phi = \varphi(0) - 2\varphi(T) + \varphi(2T) \quad (2.6)$$

with the effective wave vector $k_{\text{eff}} = k_1 + k_2$. Hence, the acceleration due to gravity is derived from three position measurements, using the wavelength of the laser light as length reference.

2.2 Measurement bias and measurement uncertainty

The terms used in this chapter follow the definitions given in the *Guide to the expression of uncertainty in measurement* (GUM) [JCG08]. A gravimeter measures a *quantity value* for the acceleration due to local gravity g . A *measurement error* Δg_{sys} will cause the gravimeter to measure the value $g_{\text{meas}} = g + \Delta g_{\text{sys}}$. The estimate of a systematic measurement error is called *measurement bias* with the *standard uncertainty* of the bias $u(\Delta g_{\text{sys}})$. When the value of the bias is known, a correction $-\Delta g_{\text{sys}}$ can be applied to the measured value to derive a corrected

value $g = g_{\text{meas}} - \Delta g_{\text{sys}}$. The *instrumental measurement uncertainty* of g is then given by the uncertainty of the bias $u(g) = u(\Delta g_{\text{sys}})$. The target instrumental measurement uncertainty for the design of QG-1 is $u(g) \leq 1 \text{ nm/s}^2$.

2.3 Sagnac effect and Coriolis bias

While the centripetal force caused by the rotation of the Earth is included in the definition of gravity (see [chapter 1](#)), it excludes any inertial forces arising from a movement of the gravimeter. In the early 1900s Baron Roland von Eötvös noticed that gravity measurements on boats moving eastward were lower and those on boats moving westward were higher. This is caused by the vertical component of the Coriolis force and known as the Eötvös effect

$$\Delta g_{\text{Cor}} = 2\Omega \cdot v_{\text{west}} \cos \phi_{\text{lat}}, \quad (2.7)$$

with the rotation rate of the Earth Ω , the longitudinal velocity in west direction v_{west} and the latitude ϕ_{lat} .

An equivalent description of the same influence on the atom interferometer is the Sagnac effect. If an interferometer encloses an area in space, rotations around the normal vector of the area induce a phase. The resulting bias on the gravity measurement for the Earth's angular velocity vector $\vec{\Omega}$ is derived in [[Pet01](#), p. 54] as

$$\Delta g_{\text{Cor}} = 2\vec{\Omega} \cdot (\vec{v}_0 \times \hat{k}_{\text{eff}}), \quad (2.8)$$

with the horizontal velocity of the atoms \vec{v}_0 and the unit vector \hat{k}_{eff} pointing in the direction of the transferred momentum \vec{k}_{eff} of the atom interferometer pulses. For a \vec{v}_0 with the length v_{west} pointing westward in the Earth system and an angle ϕ_{lat} between $\vec{\Omega}$ and $(\vec{v}_0 \times \hat{k}_{\text{eff}})$, which is the latitude, the equation is equivalent to [equation \(2.7\)](#).

The horizontal velocity of an atomic ensemble released from an atom chip can typically be controlled with a statistical standard deviation $u(v_0)$ of less than $10 \mu\text{m/s}$. This uncertainty of the horizontal velocity leads to an uncertainty for the Coriolis bias of $u(\Delta g_{\text{sys, Coriolis}}) \leq 1 \text{ nm/s}^2$ at a latitude of 52°N (Hannover, Berlin [[Hau13](#)], London) and $u(\Delta g_{\text{sys, Coriolis}}) \leq 1.5 \text{ nm/s}^2$ at the equator.

To reduce the Coriolis bias, the Earth's rotation can be counteracted. The reference mirror for the interferometry pulses is mounted on a tip/tilt stage rotating the mirror at the same projected rate as the Earth's rotation. An active compensation of the Earth's rotation rate Ω by a factor of 100, which leads to a proportional reduction of the bias and its uncertainty caused by a horizontal velocity, has been demonstrated in [[Hau13](#)]. Employing a similar technique in QG-1 (see [section 3.1](#)) will lead to an uncertainty of the Coriolis bias smaller than 0.02 nm/s^2 .

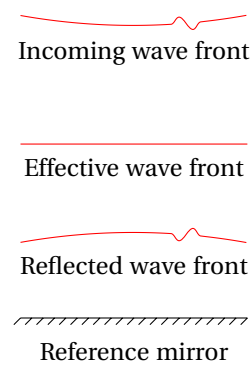
Another option for a passive compensation is enabled by the detection system of QG-1 by deriving the starting velocity of the atomic ensemble in every single measurement from the

absorption detection picture after 260 ms of free fall. With an estimated position resolution of $u(x_{\text{det}}) = 0.1 \mu\text{m}$ arising from the fit uncertainty of the evaluation method, a velocity resolution of $u(v_{\text{det}}) = 0.4 \mu\text{m/s}$ could be achieved. Additionally, the tip/tilt mirror mount can be used to induce faster rotation rates of e.g. 100 times the Earth's rotation rate to calibrate the imaging system by finding the position on the detection image where $v_0 = 0$. This initial calibration only needs to be performed once. Accordingly, the resulting Coriolis bias can be calculated with an estimated uncertainty of 0.06 nm/s^2 at the equator and smaller than this everywhere on Earth.

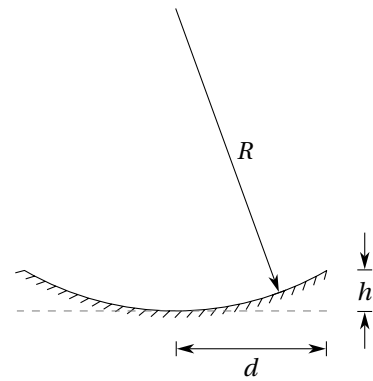
2.4 Wave front bias

The interferometry laser beam is retro-reflected on the reference mirror. The effective wave front, which is relevant for the atom interferometer phase, is a combination of the incoming wave front and the retro-reflected wave front [Kas92]. In this approach, wave front aberrations from the collimation optics (see figure 3.6) and the reflective coating on the atom chip are assumed to cancel out, because they are common to both beams [Lou11]. However, any nonplanarity of the reference mirror introduces an aberration on the effective wave front. A simple case is a parabolic curvature of the reference mirror. The following description follows the case study detailed in [Lou11, pp. 8–9]. When the surface height changes by Δh over an area with radius d the mirror introduces a parabolic curvature to the reflected wave front with the radius of curvature

$$R = \frac{(d - \Delta h)(d + \Delta h)}{2\Delta h}, \quad (2.9)$$



(a) Wave front aberrations.



(b) Modelled curvature of the reference mirror.

Figure 2.1: (a) Common mode wave front aberrations cancel out in the effective wave front, which is defined by the reference mirror surface. (b) Simple model for the radius of curvature R of the reference mirror.

which depends quadratically on the distance on the surface d (see [figure 2.1\(b\)](#)). the curvature can than be expressed as a phase shift of

$$\Delta\Phi(r) = K \cdot r^2 = \frac{k_{\text{eff}}}{2R} \cdot r^2, \quad (2.10)$$

with the radial position r in the interferometry beam. The atomic density of the thermal ensemble has a Gaussian distribution with the standard deviation σ and is presumed to be centred at the optical axis in this simple model. Considering a thermal expansion $\sigma(t) = \sigma_v \cdot t$ with the expansion rate $\sigma_v = \sqrt{k_B T_{\text{at}} / m_{\text{Rb}}}$, the atomic mass of Rubidium m_{Rb} and the Boltzmann constant k_B , [equation \(2.6\)](#) describes the bias phase introduced to the atom interferometer output [[Lou11](#), eqn. 6]

$$\Delta\Phi_{\text{Ab}} = 2K \cdot (\sigma_v)^2 \cdot T^2 = \frac{k_{\text{eff}}}{R} \cdot \frac{k_B T_{\text{at}}}{m_{\text{Rb}}} \cdot T^2, \quad (2.11)$$

with the evolution time T of the interferometer. According to [equation \(2.6\)](#), the bias on the gravity measurement is given as

$$\Delta g_{\text{Ab}} = \frac{(\sigma_v)^2}{R} = \frac{k_B T_{\text{at}}}{R \cdot m_{\text{Rb}}}. \quad (2.12)$$

It should be noted, that the wave front aberration bias Δg_{Ab} is independent of the evolution time T . To keep the bias on the gravity measurement smaller than 10 nm/s^2 (similar to [[Lou11](#)]) for a given temperature T_{at} , a minimum radius of curvature R is required. For laser-cooled atom gravimeters with a typical temperature of the atomic ensemble $T_{\text{at}} = 2 \mu\text{K}$, R has to be bigger than 20 km. Therefore, the flatness of the reference mirror has to be $\Delta h \leq \lambda/300$ over a distance of $d = 10 \text{ mm}$. This is the limit of technical feasibility. To further reduce the wave front bias by more than one order of magnitude to less than 1 nm/s^2 , the average expansion rate σ_v needs to be reduced by more than two orders of magnitude. Expansion velocities equivalent to a temperature of 1 nK have already been demonstrated with collimated BECs from an atom-chip-based source [[Kru14](#)]. This low expansion rate relaxes the requirement on the wave front curvature. For example, a radius $R \geq 0.5 \text{ km}$ will limit the bias on the gravity measurement to a value smaller than 0.2 nm/s^2 . This radius corresponds to a flatness of the reference mirror of $\Delta h < \lambda/13$ over a distance of $d = 10 \text{ mm}$ or a height difference of $\Delta h < \lambda/1266 \approx 1 \text{ nm}$ over a distance of $d = 1 \text{ mm}$. This can be achieved with the typical polishing quality P4 according to DIN ISO 10110 with a roughness of less than 1 nm over distances of 0.002 mm to 1.0 mm. While wave front aberrations on smaller scales are averaged out in atom gravimeters employing thermal ensembles with a Gaussian width on the scale of a few mm to a few cm, a smaller test mass is more sensitive to small scale aberrations of the wave front. The smaller size of a collimated BEC on the order of $100 \mu\text{m}$ requires a knowledge of the mirror surface on smaller length scales. On the other hand, it allows to probe the wave front using the atomic ensemble itself.

Wave front mapping

The wave fronts introduced by typical optical components are more complex and require a more sophisticated evaluation. In [Sch17], the surface profiles of the reference mirror and additional optical components in the beam path of their apparatus have been measured using optical methods and the influence on the interferometer phase has been simulated for the GAIN gravimeter. The results of the simulation have been verified with experimental results. For an additional view port introduced in the beam path, the bias on the gravity measurement could be predicted with a stated uncertainty of the method of 3.8 nm/s^2 . The bias introduced by the reference mirror in the GAIN gravimeter was calculated as $(4.0 \pm 1.9) \text{ nm/s}^2$ for an ensemble with a temperature of $3 \mu\text{K}$. This was mainly caused by a parabolic deformation of the mirror surface.

Using a BEC, the smaller size enables a mapping of the wave front using the test mass itself. With the atom chip a precise control of the start position and the horizontal velocity is possible. The magnetic lens enables the tuning of the expansion velocity of the ensemble. By these means the wave front can be probed using different trajectories. This also allows to test the theoretical model and to reduce the uncertainty of the bias.

2.5 Conclusions on the gravimeter design

The following mitigation strategies and solutions have been developed to reach a target instrumental measurement uncertainty of $u(g) \leq 1 \text{ nm/s}^2$ in a transportable gravimeter:

Stability The statistical uncertainty is a measure for the stability of the gravimeter. Both, the per-shot statistical uncertainty and the statistical uncertainty reached after averaging, are important characteristics. The per-shot statistical uncertainty is given by the self noise of the instrument and environmental noise. The shot noise in the interferometer read out will be reduced by a high atom number and a high contrast. To achieve a high-contrast interferometer signal with Bragg diffraction on a light grating, a low velocity spread and therefore an ultra-cold ensemble is needed [Szi12]. To keep the external noise level low, the sensor head needs to be magnetically decoupled from the environment with a magnetic shield (section 3.7). Seismic noise is suppressed by a vibration isolation platform and the residual vibrations can be tracked by a low self-noise seismometer and compensated actively [Lau14] or in post-correction [Far14]. For uncorrelated noise, the statistical uncertainty of an average over N single shots reduces to $1/\sqrt{N}$ of the per-shot statistical uncertainty. Short averaging times are beneficial both for the characterisation of the various systematic effects as well as for geodetic measurement campaigns. Thus, a low per-shot statistical uncertainty and a high repetition rate are required. BEC sources with cycle times on the order of 2 s have already been demonstrated using atom-chip-based magnetic traps [Rud15].

Accuracy The accuracy is limited by the statistical uncertainty and the uncertainty of the instrumental bias. While the statistical uncertainty can be reduced by averaging over a number of measurements, the instrumental bias needs to be characterised with a low uncertainty to ensure instrumental drifts will not affect long-term measurements over years and to be able to compare the results of two independent gravimeters. The strategy to reduce the wave front bias (see [section 2.4](#)) and its uncertainty in QG-1 is two-fold: (i) The expansion rate of the test mass is decreased by the implementation of an ultra-cold atom source and subsequent magnetic lensing ([section 3.2](#)) and (ii) the wave front aberrations are minimised by placing the reference mirror inside the vacuum chamber ([section 3.1](#)). Furthermore, to lower the Coriolis bias and its uncertainty, the atom-chip-based source ([section 3.3](#)) provides control of the horizontal velocity. The residual horizontal velocity will be measured using spacial detection with absorption imaging ([section 3.6](#)) and additionally a compensation of the Earth's rotation is possible with a built-in tip/tilt mirror mount ([section 3.1](#)).

Transportability To measure gravity at relevant locations for geodesy, the QG-1 apparatus needs to be transportable in a van. To keep the size small and the weight low compared to laboratory-sized BEC experiments, an atom-chip-based source of ultra-cold atoms is a necessity. For transportability, the QG-1 apparatus is split into two units: The first unit is the sensor head ([chapter 3](#)), where the measurement of gravity is performed. And the second unit is a rack containing the laser system ([chapter 4](#)) as well as the electronics ([chapter 5](#)) to drive the measurement. As the laser system and the electronics produce heat, mechanical and electro-magnetic noise, the rack has to be spatially separated from the sensor head. For a speedy set up at remote measurement sites, the two units are self-contained and only need to be connected by electrical and optical fibre cables. And finally, the apparatus has to be operable outside a temperature stable laboratory requiring a temperature stabilisation of the laser and electronics rack.

CHAPTER 3

Sensor head

The measurement of gravity is performed in the sensor head. It houses the source of the ultra-cold atomic test mass, the optical components to perform atom interferometry with a light grating and a detection camera to record the interferometer output. [Figure 3.1](#) shows the setup of the sensor head developed within the frame of this thesis. The important aspect in the design process was the laser beam path for atom interferometry, which is highlighted in red in [figure 3.1](#) and shown schematically in [figure 3.6](#). The reference mirror for the light grating is

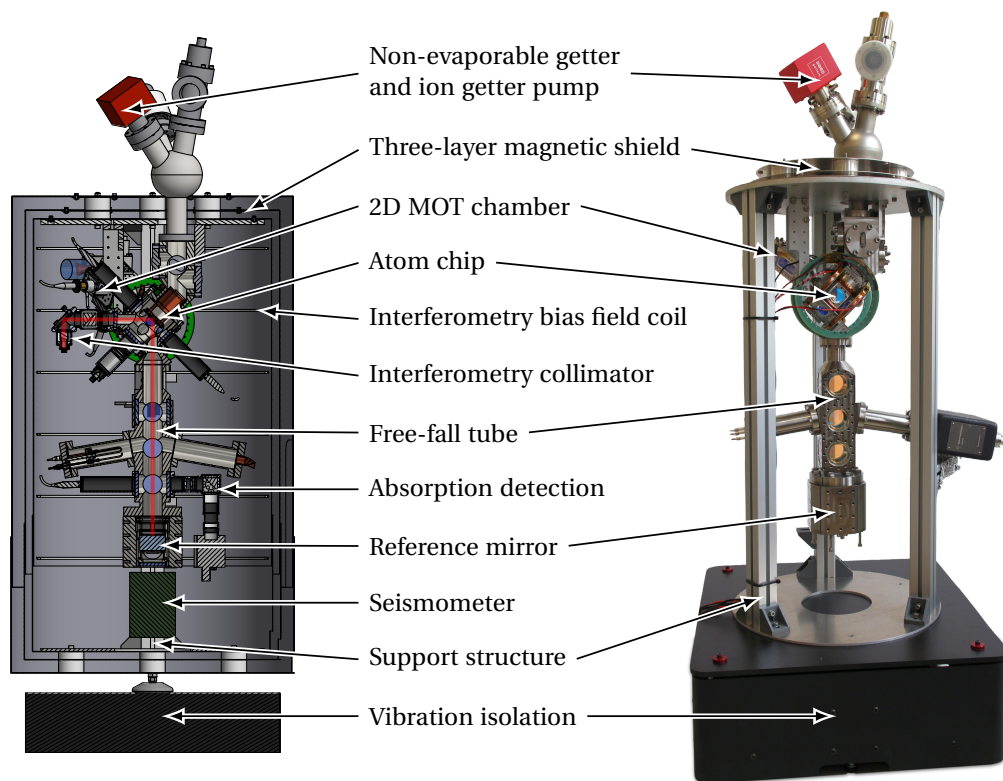


Figure 3.1: A section view (left) of the sensor head with the interferometry laser beam path depicted in red and a picture (right) of the assembled vacuum system on top of the vibration isolation platform.

placed inside the vacuum chamber with no additional optics between the mirror surface and the atomic test mass. The atom interferometer baseline is positioned at the central axis of the vacuum tube and the cylindrical magnetic shield. All components inside the magnetic shield are non-magnetic. The sensor head is spatially separated from the laser system ([chapter 4](#)) and electronics ([chapter 5](#)) to realise a low-noise measurement environment and seismically decoupled from the environment with a vibration isolation platform. It is foreseen to record residual vibrations with a seismometer. In this chapter, each component of the sensor head will be introduced starting with the elements necessary for atom interferometry.

3.1 In-vacuum reference mirror assembly

Schkolnik et al. showed, that wave front aberrations in their apparatus are mainly caused by the vacuum view port and the quarter wave retardation plate located between the reference mirror and the probed atomic ensemble [[Sch17](#), pp. 74–82]. For the QG-1 apparatus, the reference mirror is consequently placed inside the vacuum chamber to eliminate the need for a vacuum view port. With the employment of Bragg diffraction instead of Raman diffraction the need for a quarter wave retardation plate is omitted. In QG-1, the retro-reflection mirror is the only reference for the wave fronts in the atom interferometer as described in [section 2.4](#).

High-quality mirror surfaces with low deformation can be easily achieved with standard manufacturing techniques on thick glass substrates. The reference mirror is made from an etalon substrate [Laseroptik Garbsen, S-05487-01] with 30 mm height and 50.8 mm diameter. The mirror substrate meets a surface form tolerance of 3/0.1 after standard ISO 10110-5, which corresponds to a surface flatness of $\lambda/20$ at 633 nm over the diameter of the substrate of 50.8 mm. A high reflective (HR) dielectric coating [Laseroptik Garbsen, 26015ke2] has been applied using ion beam sputtering. This coating technology has the lowest number of defects or cavities compared to other typical production methods. The substrate features an anti-reflective (AR) coating [Laseroptik Garbsen, 23015ke2] on the backside to reduce reflection of residual transmitted light, that can be measured by a photodiode at the AR coated vacuum view port underneath the mirror. This can be used to monitor the intensity and the beat note of the interferometry grating. To maintain the surface flatness after mounting the mirror, the mirror holder is designed with special care to safely fix the mirror substrate without deforming it. Therefore, the substrate is resting on three titanium spheres close to the outer edge and is clamped by another three spheres on top of the substrate (see [figure 3.2](#)). A Kalrez o-ring is used instead of a spring to apply a small force for clamping similar to the setup described in [[Mer10](#), p. 99]. To prevent horizontal movement, three screws keep the substrate in place but exert no force.

A mirror substrate from the same batch as the mirror placed inside the QG-1 vacuum chamber has been mounted in an identical mirror mount and the surface flatness has been characterised by *Laseroptik Garbsen* with an optical interferometer [TRIOPTICS, μ Phase

plano down]. The measurement wavelength of 633 nm is phase shifted by the HR coating for 780 nm. This influences the measurement and can lead to a phase jump in the observed fringe pattern. Therefore these areas have been excluded and only an area of 35 mm diameter has been evaluated. The peak/valley height difference was measured as 42 nm or $\lambda/15$. Additionally, an area of interest in the centre with a diameter of 10 mm was evaluated and showed a peak/valley height difference of 16 nm or $\lambda/40$ (see [appendix A.1](#)). Therefore, the evaluated substrate exceeds the requirement of a height difference of less than $\lambda/13$ over a distance of $d = 10$ mm (see [section 2.4](#)).

Tip/tilt mirror mount for Coriolis compensation and self alignment

Tip/tilt actuation of the reference mirror is realised by three piezo actuators [PI Ceramic, PICMA Stack P-885.90] in the mirror holder. This enables active stabilisation of the parallelism of the wave vectors for interferometry in a similar manner to [Hau13] ensuring a stable effective wave number k_{eff} . To compensate the Coriolis effect, the rotation of the Earth with a rate of 2π per day or $73 \mu\text{rad/s}$ has to be counteracted by rotating the mirror with the same rate as the projection of the Earth's rotation on the local horizontal north axis. The three piezo stacks are arranged in an equilateral triangle rather than the classical L-shape for mirror holders with a right-angled triangle. One reason is the tight space, given by the diameter of the mirror substrate of 50.8 mm and the design choice to insert the mirror mount through a CF 63 flange with an inner diameter of 64 mm. The design is furthermore advantageous, as the rotation point for tip/tilt actuation can be placed in the centre of the mirror not changing the position of the mirror surface centre, where the interferometry beam is reflected.

The setup of the tip/tilt mirror holder is shown in [figure 3.2](#). The vacuum compatible piezo

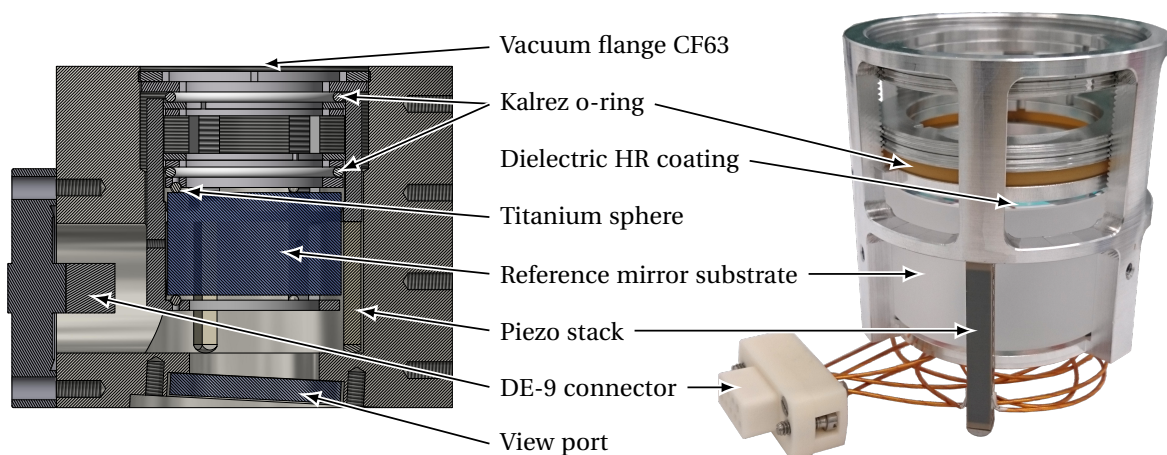


Figure 3.2: A section view (left) of the reference mirror inside the bottom vacuum chamber and a picture (right) of the mirror holder assembly.

stacks have an all-ceramic isolation of the piezo layers, therefore no polymer isolation with a high outgassing rate is needed. This leads to a better vacuum compatibility. One end of the stacks is glued to the mirror holder frame using the same metal-to-ceramic glue [Epoxy Technology, Epo-Tek H77] as for the atom chip. To prevent lateral forces on the stack, the opposing end features a spherical tip which has been custom made of titanium. To keep the mirror holder in position and to mechanically preload the piezo actuators, instead of a mechanical spring a synthetic rubber o-ring typically used as UHV seal [DuPont, Kalrez] presses on the assembly. When the piezo stacks expand, they squeeze the rubber of the Kalrez ring (see figure 3.2).

The tilt of the mirror was measured as 1.3 mrad after applying a voltage of 150 V to a single piezo stack. According to its datasheet, the length change of the piezo is 320 nm/V resulting in a tilt of 1.1 mrad at a voltage of 150 V. In the following, the more conservative value from the datasheet is used. For a rotation with an angle η around the H axis and an angle ρ around the P axis through the centre of the mirror (see figure 3.3), the piezo stacks 1, 2, 3 need to be driven with voltages

$$\begin{pmatrix} U_1 \\ U_2 \\ U_3 \end{pmatrix} = 90 \text{V/mrad} \cdot \begin{pmatrix} \eta \\ -\frac{1}{2}\eta + \frac{\sqrt{3}}{2}\rho \\ -\frac{1}{2}\eta - \frac{\sqrt{3}}{2}\rho \end{pmatrix}, \quad (3.1)$$

with the approximation $\sin(\alpha) \approx \tan(\alpha) \approx \alpha$ for small angles. While operation in the range of -20 V to 120 V is possible, the low voltage range -15 V to 15 V is sufficient and gives a tilt range of 0.33 mrad . This corresponds to a maximum rotation rate of 1.67 mrad/s during the maximum interferometer evolution time $2T = 200 \text{ ms}$, which is more than 20 times the rotation rate of the Earth. For the characterisation of the instrumental uncertainty (see section 2.3)

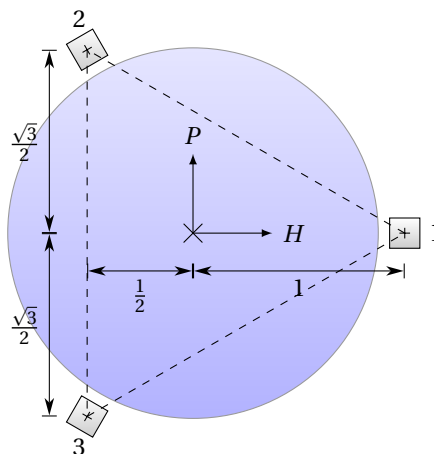


Figure 3.3: The arrangement of the three piezo stacks (squares) and the reference mirror (circle) with the rotation axes P and H .

the rotation rate can even be as high as a hundredfold of the Earth's rotation rate during $2T = 40\text{ms}$.

3.2 High-flux source of ultra-cold atoms

The design of the source is based on the atom chip source developed in the QUANTUS collaboration, which was pioneered in the QUANTUS-2 apparatus [Her13; Rud15] and improved in the MAIUS-A apparatus [Bec18; Sei14]. The design of the high-flux source of ultra-cold atoms in QG-1 has been described already in detail in [Sah19] and will only be summarised here.

The source has to produce ultra-cold ensembles with a high number of atoms and a fast repetition rate, while maintaining good ultra-high vacuum (UHV) quality in the main vacuum chamber. The loading time of the magneto-optical trap (MOT) from the low Rubidium vapour pressure in the UHV chamber typically dominates the preparation time in an atom-chip-based source. In the presented design, the mirror MOT on the chip [Wil04] is loaded from a 2D MOT, which is located in a separate chamber with two-orders of magnitude higher Rubidium vapour pressure. The 2D MOT provides confinement and cooling in two dimensions with a magnetic field gradient produced by four coils in racetrack configuration and retro-reflected transversal cooling laser beams. The circular Gaussian beams are divided at a 50/50 beam splitter into two beams passing the vacuum chamber providing a longer trapping region. A pusher and retarder beam in $2D^+$ MOT configuration [Cha06] provide additional cooling in the longitudinal direction and give the atomic beam a forward velocity towards the MOT in the main chamber. The resulting laser cooled atomic beam has a flux of $2.2 \cdot 10^9$ atoms/s [Sah19].

The main chamber features the atom chip and three Helmholtz coil pairs with orthogonal axes mounted on the outside. These coils create a homogeneous magnetic field with precise control over the field strength and direction. Combined with the field from the current-

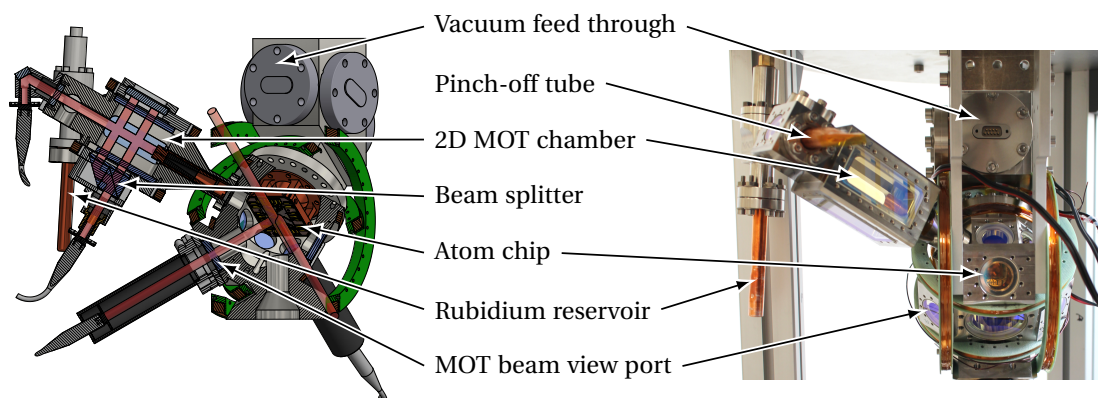


Figure 3.4: A section view (left) of the 2D MOT chamber and the main chip chamber with the cooling laser beams depicted in red and a picture (right) of the assembled vacuum chambers. For illustration purposes the laser beams are sketched as cylinders with a diameter of 8 mm.

carrying structures on the atom-chip the magnetic fields for trapping and cooling of the atomic ensemble are created. For collimation of the ultra-cold atomic ensemble after release from the trap, the magnetic fields need to be switched fast. For this purpose the coils are connected such, that one quarter of the coil windings can be used as a smaller coil with lower inductance leading to faster switching times (see also [section 5.3](#)).

3.3 Mirror coating on the atom chip

Atom-chip-based magnetic traps with strong confinement are located close to the current carrying wires limiting the optical access. If an optically transparent chip is used, the wires would partially block the Gaussian laser beams for interferometry. Another option is aligning the laser beam parallel to the atom chip, which would result in a clipped beam profile. For a collimated Gaussian beam with a waist w or a $1/e^2$ diameter of $2w = 4$ mm, 99 % of the optical power is transmitted through an aperture with radius $3w$ or a diameter of $6w = 12$ mm. For an undisturbed Gaussian beam profile, the atomic ensemble would need to be transported 6 mm away from the chip surface. A common solution for laser cooling is the mirror magneto-optical trap (mirror MOT) which "hides" the chip behind a mirror reflecting the laser beams [[Rei99](#); [Wil04](#)]. The same approach was adopted in QG-1 not only for the MOT (see [figure 3.5\(b\)](#)) but also for the interferometry beam (see [figure 3.5\(c\)](#)). As the ensemble drops away from the chip surface, this configuration obviates the need for disturbance-free transportation of the trapped ensemble. The coating covers at least 18 by 18 mm of the chip surface (see [figure 3.5\(a\)](#)). This results in a clear aperture with a diameter of $18\text{ mm}/\sqrt{2} = 12.8\text{ mm}$ due to the 45° angle.

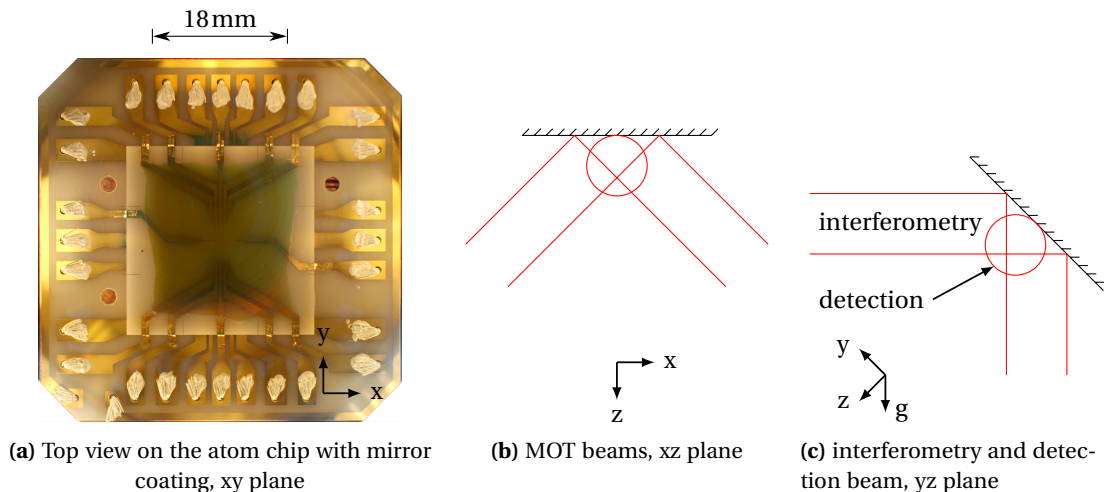


Figure 3.5: Reflection of optical laser beams on the atom chip surface. For this illustration the laser beams are sketched with a diameter of 8 mm. The optical axis of the beams parallel to the atom chip surface has a distance of 4 mm to the chip surface. The coordinate axes represent the chip coordinate system, which is used throughout this thesis.

By reflecting the interferometry beam on the atom chip, undisturbed Gaussian beam $1/e^2$ diameters of 4 mm with $6w = 12$ mm are feasible.

The dielectric mirror layers have been coated onto an transfer glass substrate [OIB Jena] and glued to the surface of the atom chip using epoxy glue [Epoxy Technology, Epo-Tek 353ND]. After curing the glue, the transfer substrate is carefully ripped off the atom chip leaving the dielectric mirror coating with the same surface quality as the transfer substrate. Special care has been given to increase the viscosity of the epoxy glue to prevent it from entering small gaps in the dielectric coating which would lead to bigger defects. The surface roughness has been specified as a peak-to-valley height of 30 nm over the width of a wire on the science chip [Sah19].

3.4 Laser beam collimation for the interferometry light grating

The laser light used for the Bragg grating pulses is guided to the sensor head in a polarisation maintaining fibre optic cable [Schäfter+Kirchhoff, PMC-780]. After exiting the fibre facet the light intensity shows an expanding Gaussian profile. It is collimated by a single achromatic lens. The Gaussian beam diameter has to be large enough to give a flat intensity distribution over the extend of the atomic ensemble. Otherwise the contrast of the atom interferometer is reduced as the diffraction is less effective for atoms with higher distance to the optical axis due to the smaller intensity and lower Rabi frequency.

In atom interferometers with thermal ensembles Gaussian beam diameters of 20 mm to 30 mm are common; e.g. 29.5 mm in [Sch15]. In [Lou11] the atomic ensemble has an $1/e^2$

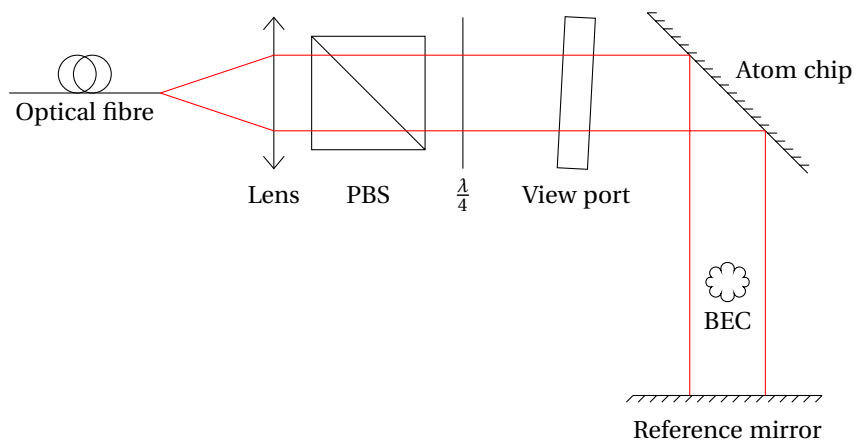


Figure 3.6: Interferometry laser beam path inside the sensor head with the laser beam depicted in red. The collimation optics consist of the fibre tip, a collimation lens, a polarisation-beam splitter (PBS) for polarisation cleaning and a quarter wave plate ($\frac{\lambda}{4}$). The wave plate is aligned to the PBS such that circular polarised light is attained. The laser beam passes a vacuum view port and is reflected on the HR coating of the atom chip before it interacts with the atoms, is reflected on the reference mirror and interacts with the atoms again.

diameter of 4 mm in the detection zone and Gaussian beams with an $1/e^2$ diameter of 24 mm are used for interferometry. With the small size of a magnetically collimated BEC on the order of $100\ \mu\text{m}$ and an expansion rate below 1 mm/s a considerably smaller Gaussian beam diameter is feasible. A Gaussian beam with an $1/e^2$ diameter of 4 mm ensures an intensity variation smaller than 1 % over a diameter of $280\ \mu\text{m}$.

3.5 Vacuum chamber

The QG-1 vacuum chamber has been manufactured by the precision engineering workshop of the Institute of Quantum Optics from a Ti6Al4V titanium alloy¹. Titanium was selected because of its low remanent magnetisation and low density similar to aluminium and its mechanical rigidity. The vacuum view ports feature an AR coating [Laseroptik Garbsen, 22104Ma1, 22104Ma2] on both sides of a wedged N-BK7 substrate. The small angle of $30'$ between both surfaces eliminates interference from residual reflections. Additionally to the wedged substrate, the vacuum view port for interferometry and the view port underneath the reference mirror are installed with a 3° tilt with respect to the optical axis to prevent the forming of a parasitic cavity from residual reflections. N-BK7 glass is transparent for wavelengths up to $2.5\ \mu\text{m}$. This enables the measurement of the atom chip temperature with an optical infrared pyrometer to characterize the black body radiation in the future. The AR coating is optimised for the laser wavelengths $780\ \text{nm}$ for laser cooling and $1,56\ \mu\text{m}$ for the operation of an optical dipole trap.

The vacuum pumps needed for UHV operation are attached at the top². The commercial [SAES, NEX Torr D 200-5] pump is a combination of a 200 l/s non-evaporable getter (NEG) and a 5 l/s ion-getter pump (IGP). Additional CF flanges are located close to the pump which feature an UHV pressure sensor [Pfeiffer, IKR 270] and a valve [VAT, Series 541 Easy close all-metal angle valve DN40] for initialisation of the vacuum using a turbomolecular pump.

3.6 Absorption detection system

On the free-fall tube of the vacuum chamber, detection view ports are placed at different heights. They are located 179 mm, 250 mm and 321 mm below the atom chip and have a free optical aperture of 38 mm. These positions amount to times-of-flights of 191 ms, 226 ms and 256 ms. For the mapping of the Bragg grating wave fronts, ensembles with high expansion rates might be used. In this case it is advantageous to detect after a shorter time-of-flight. There are view ports located on all four sides of the vacuum chamber enabling 3D imaging schemes with two crossed detection axes. Another absorption detection system is installed at the main atom

¹ Also known as Grade V Titanium

² An additional IGP (see [appendix A.2](#)) is provisionally attached to the side of the free-fall tube.

chip chamber to characterise the atomic ensemble in the magnetic trap. It has been assembled and characterised within the scope of the Bachelor's thesis of Jannik Wesche [Wes17].

3.7 Magnetic shield

The sensor head, except for the vacuum pump system at the top, is completely enclosed by a three-layer magnetic shield. It is made of a mu-metal alloy with a high magnetic permeability μ which allows the magnetic flux to stay inside the shield leaving the shielded volume free of any magnetic flux. Each layer consists of three parts as illustrated in figure 3.7. The tube extends over the complete atom interferometer baseline and the length of the vacuum system and shields the sensor head from radial magnetic field components. The tube can be unmounted by pulling it upwards and has an end cap at the top with a centred hole to fit over the vacuum pump system. This hole is closed by the second part: the top disk is fixed on the support structure and has a 7 cm off-centre hole for the vacuum tube connecting the pump system with the main vacuum chamber. The bottom end cap features a tube overlapping with the first tube and is long enough to integrate the seismometer inside the magnetic shield. The tube can be retracted inside the bottom part as depicted in figure 3.7(b) to shorten the shielded volume when the seismometer should be attached outside the shield. For this purpose, the bottom end cap has three mounting holes to mount the seismometer directly to the vacuum chamber containing the reference mirror.

The magnetic shield has been designed and manufactured by Magnetic Shields Ltd. as a three-layer shield. During characterisation by the same company it was shown, that the

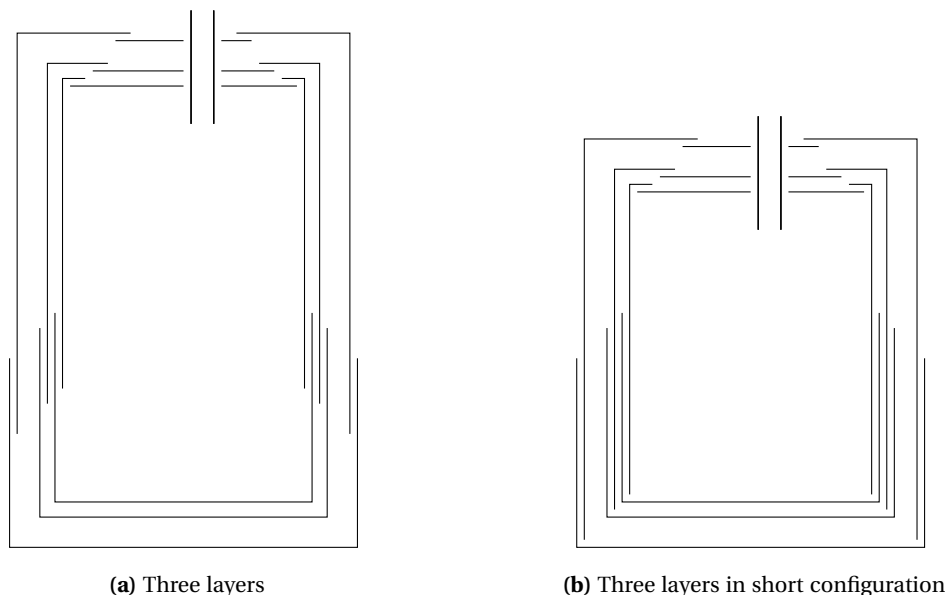


Figure 3.7: Simplified sketch of the magnetic shield design, not to scale.

three-layer shield has no significant improvement in shielding performance than using only the inner two layers of the shield. **Figure 3.8** shows the residual magnetic field strength in radial and in axial direction. To calculate the shielding factor, the total field strength in 3D is compared to the strength of the Earth's magnetic field outside the magnetic shield which was measured as $41 \mu\text{T}$. Excluding the top and bottom 5 cm inside the 83.5 cm high shield (marked grey in **figure 3.7**), the shielding factor is better than 180 in both variants. The residual magnetic field strength gradient will be compensated using the quantisation magnetic field coils for the atom interferometer baseline.

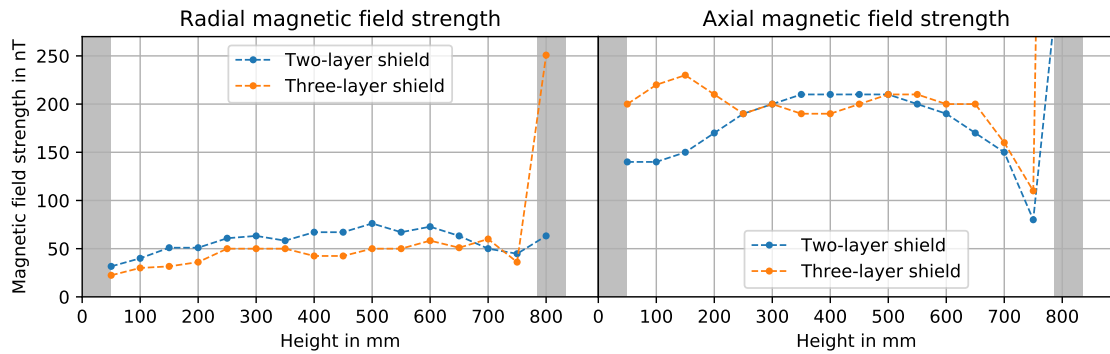


Figure 3.8: Measurement of the magnetic field components inside the magnetic shield. The height is measured from the bottom support disk inside the shield. The magnetic field strength outside the shield was measured to be $41 \mu\text{T}$ caused by the magnetic field of the Earth. Marked in grey are the topmost and bottommost 5 cm inside the shield which are excluded from the evaluation.

CHAPTER 4

Laser system

Given the need for a robust laser system with few mechanical parts and high output power, the main parts are implemented using fibre coupled components operating at a wavelength of 1560 nm in the telecom C-band. Due to the use of this wavelength in telecommunication networks, reliable, fibre-coupled components are commercially available. The laser frequency is then doubled using second harmonic generation in a non-linear crystal and distributed using free-space optics to several optical fibres guiding the laser light to the sensor head. The laser system and distribution module has been set up during the Master's thesis of Nina Heine, née Grove, [Gro17] and is running since then with low maintenance for years. The cold laser system is operational 2 minutes after being switched on. During the warm up time of 90 minutes an intensity drift can be observed. The optical alignment of the free-space distribution module and the fibre couplers has been optimised about once a year. A detailed description of all components and the complete setup can be found in [Gro17] therefore only a brief summary is given in this section.

4.1 Spectroscopy reference module

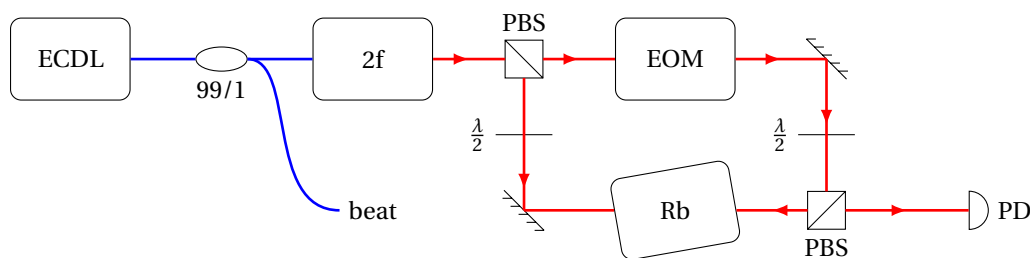


Figure 4.1: Simplified diagram of the ECDL laser and spectroscopy module.

The spectroscopy reference module has been set up within the scope of the Master's thesis of Matthias Gersemann [Ger16, p. 31]. A spectroscopy cell with rubidium vapour provides a stable reference for the laser frequencies needed for atom cooling and interferometry. Spectroscopy of the rubidium D2 line at 780.24 nm is performed with a fibre coupled external cavity diode laser (ECDL) [Thorlabs, SFL1550P] running at 1560.48 nm. The laser light is frequency

doubled before entering a Doppler-free saturation spectroscopy setup. A pump beam saturates the Doppler broadened atomic transitions whereas a low power probe beam with good spatial overlap passes the vapour cell in opposite direction and its intensity is recorded on a photodiode. The resulting spectrum is shown in figure 4.2. The blue line represents the photodiode signal of the transmitted probe beam intensity while changing the laser diode current which controls the laser frequency. A dispersive signal for a lock-in laser frequency stabilisation scheme is generated by modulating the pump beam with an electro-optical modulator (EOM) at 7 MHz and demodulating the photodiode signal with the same frequency shifted in phase. Frequency generation, demodulation and lock-in amplifier are all realised digitally on a field programmable gate array (FPGA) described in section 5.1. The laser frequency is locked on the ^{85}Rb $|5S_{1/2}, F=3\rangle$ to $|5P_{3/2}, F=4\rangle$ transition which provides the highest reference signal. The ECDL is temperature stabilised using an internal peltier element and a digital feedback controller [Meerstetter, TEC-1091]. It is operating at a stable temperature setpoint untouched for months at lab temperatures of 23 °C to 27 °C. This is an important prerequisite for the implementation of an auto-lock routine enabling autonomous operation in field. The free-space optical setup in the spectroscopy module has been stable and needed no realignment for years.

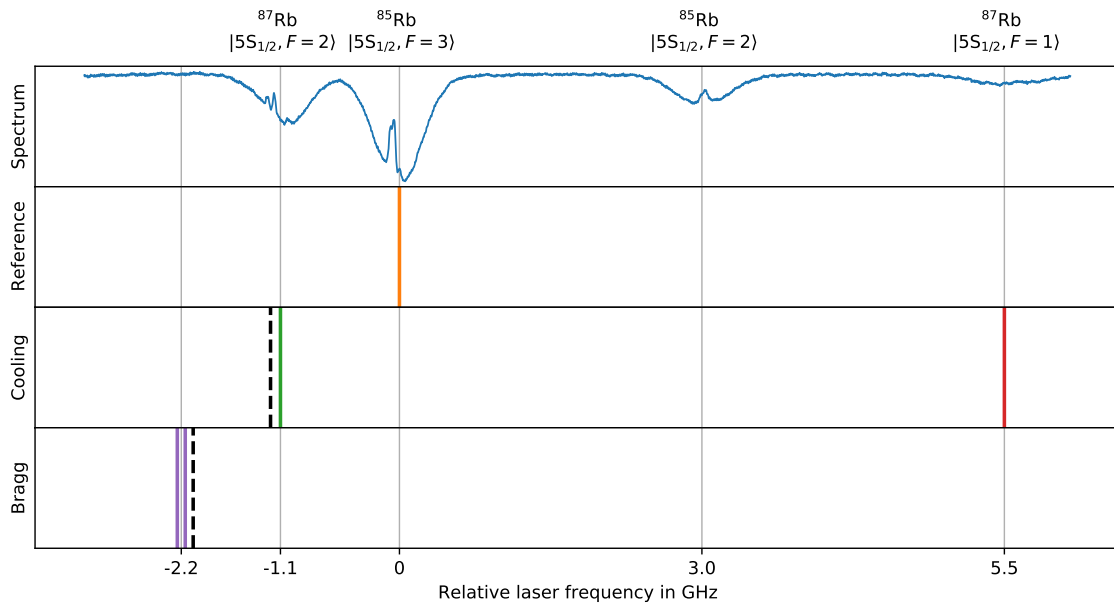


Figure 4.2: Overview of the laser frequencies needed for the operation of the QG-1 gravimeter. The frequency spacing is not to scale to improve legibility. (i) An absorption spectrum of the Rubidium D2 line recorded with the spectroscopy module is depicted in blue. The ground states of each transition are denoted in the diagram. (ii) The frequency of the reference laser locked onto the Rubidium spectroscopy is shown in orange. (iii) The frequency of the DFB laser is marked as dashed black line. The resulting laser frequencies in the sensor head for laser cooling are illustrated in green and red. (iv) The frequencies of the Bragg grating for diffraction of the atomic ensemble are depicted in purple.

4.2 High-power laser and distribution module

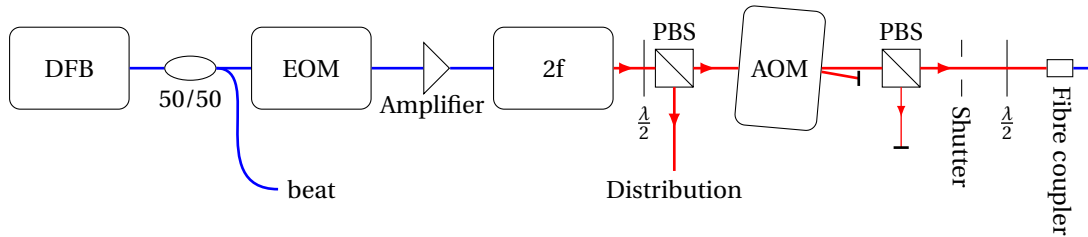


Figure 4.3: Simplified diagram of the laser system and one exemplary beam path in the distribution module.

Only a single laser is used for cooling and manipulation of the atomic ensemble. The fibre coupled distributed feedback laser (DFB) diode [Toptica, LD-1550-0080-DFB-1] is locked on the aforementioned reference laser by measuring and stabilising the beat note of the two laser sources. The two light fields are superimposed at 1560.48 nm using an evanescent wave fibre beam splitter [Thorlabs, PN1550R5A2]. Therefore, the beat frequency is only half of the difference after frequency doubling. The beat note is recorded using a fibre coupled photodiode [Thorlabs, FGA01FC] providing a stable signal without need for optical alignment.

On the laser frequency of the DFB diode, a fibre coupled EOM generates sidebands via phase modulation. In the experimental sequence, the first sideband is needed to drive the repump transition for laser cooling and is switched off subsequently. The modulated light is used as seed for a fibre amplifier [Keopsys, CEFA-C-PB-HP-PM-42-ML1-OM-B301-FA-FA] which provides up to 15 W stabilised output power. All components and fibres are polarisation maintaining for linear polarised light. The output fibre of the fibre amplifier guides the laser light to a free-space frequency doubling module [Toptica, SHG Smart] with a PPLN bulk crystal for second harmonic generation (SHG) in single-pass configuration. One lens focuses the input beam at 1560.48 nm with the focal point inside the crystal and a second lens collimates the output beam at 780.24 nm. The residual light power at the fundamental wavelength is filtered out using two subsequent dichromatic mirrors. At the output of the frequency doubling module up to 3 W optical power in the second harmonic wavelength 780.24 nm are available as free-space beam.

In the distribution module, the laser light power is splitted between the paths for atom cooling, detection and interferometry. For fast switching and control of the laser intensity, each path features an acousto-optic modulator (AOM) [A.A. Opto-Electronic, MT80] with 80 MHz modulation frequency. Slow switching and full blocking of the laser light is provided by bi-stable mechanical shutters [Uniblitz, ES6B]. The polarisation state is filtered using a polarisation beam splitter (PBS) filtering out the unwanted polarisation axis. The linear polarised light is then coupled in the polarisation maintaining fibres [Schäfer und Kirchhoff, PMC-780] guiding the laser light to the sensor head.

4.3 Generation of laser frequencies for Bragg diffraction

The light grating used for Bragg diffraction of the atomic ensemble is a moving grating created by two light frequencies with frequency difference δ_{Bragg} in the range of 1 kHz to 10 MHz. The two light frequencies are generated by modulating the AOM in the interferometry path with two frequencies centred at 80 MHz. Here the first negative diffraction order is used to reduce the laser frequency by $80\text{ MHz} \pm \delta_{\text{Bragg}}/2$ (purple lines in [figure 4.2](#)). The maximum detuning of the DFB laser (dashed black line in [figure 4.2](#)) from the ^{87}Rb cooling transition $|5S_{1/2}, F=2\rangle$ to $|5P_{3/2}, F=3\rangle$ possible with the current electronic setup is 1.1 GHz. However, the detuning can easily be increased to 3.3 GHz using an additional frequency divider for the beat note. A larger detuning is advantageous as it further reduces the rate of excitation to the $|5P\rangle$ manifold. Another option for a large detuning is free running operation as has been shown by [\[Abe16\]](#). The beat note can then be monitored to derive the exact k_{eff} . The detuning is fundamentally only limited by the laser current tuning range. For the DFB laser diode, it is specified as more than 100 GHz.

4.4 Generation of laser frequencies for atom cooling

Laser cooling of ^{87}Rb is performed red-detuned from the $|5S_{1/2}, F=2\rangle$ to $|5P_{3/2}, F=3\rangle$ transition. This transition has a frequency of 1126 MHz lower than the reference transition described earlier. The DFB laser (dashed black line in [figure 4.2](#)) is locked at a beat note of $(-1126\text{ MHz} + \delta_{\text{cool}} - f_{\text{AOM}})/2$ before frequency doubling with a typical detuning of $\delta_{\text{cool}} = -18\text{ MHz}$ and an AOM frequency of $f_{\text{AOM}} = 80\text{ MHz}$. A fibre coupled EOM modulates sidebands on the laser frequency. The first sideband with +6.6 GHz is on resonance with the repump transition $|5S_{1/2}, F=1\rangle$ to $|5P_{3/2}, F=2\rangle$. Both laser frequencies are shifted by the AOM by +80 MHz as the first positive diffraction order is used.

CHAPTER 5

Control electronics

To power the laser system and the sensor head, various electrical voltages, currents and RF signals are generated, monitored and stabilised by the control electronics. Several feedback loops are implemented to stabilise frequencies, light intensities, magnetic fields and temperatures. For a measurement on an ensemble of ultra-cold atoms, an experimental sequence must be executed to prepare the ensemble and to acquire the measurement data. For example, the set-point of the feedback loop stabilising the laser frequency is first red-detuned from the atomic transition and for the acquisition of an absorption image set on resonance. In synchronisation with the laser system, the CCD camera needs to get a trigger signal to record an image of the atomic ensemble. This sequence is edited on a control computer. The experiment is controlled by dedicated modules which have their own local memory for a sequence of parameters. Most of the modules used in the QG-1 electronic system are parts of the *TBUS Modulsystem* and can be put together as compact electronic stacks. They have been developed in the Institute of Quantum Optics by Dr. Thijs Wendrich and the LASUS team for the use in micro-gravity experiments with ultra-cold atoms in the QUANTUS collaboration. The QG-1 electronic system consists of two TBUS stacks, one additional FPGA module with analogue-to-digital converters (ADC) [National Instruments, NI USB-7855R] and a separate temperature controller module. At the start of the sequence one stack triggers the other stack and the FPGA module. The timing in all three units is synchronised with a common 20 MHz clock. All components are connected via Ethernet or USB to the central control computer for sequence uploading and for data acquisition. The components of the electronics system will be introduced in the following subsections.

5.1 Electronic stack for the laser system

The TBUS stack controlling the laser system fits into a 19" rack mount with a height of 3 units or 13 cm. Air cooling is provided by fans in the back of the chassis. The modules along with their connections to the laser system have been described in [Gro17] and will only be summarised here.

Power module and Ethernet interface module

The power module provides an electrical connector for the input voltages provided either by laboratory power supplies or batteries. The specified voltages are multiples of the voltage of one standard lithium polymer battery cell of 3.3 V to 4 V. The module provides monitoring of the voltages and the current drawn by the stack.

The Ethernet interface module allows to read or write to register addresses on the TBUS with a simple protocol. It also generates a 24 MHz bus clock to synchronise the timing of the modules which is locked on a 20 MHz reference clock input.

Laser current driver module

This module has two output channels to drive laser diodes. Each channel features a low noise current driver circuit similar to [Lib93] which actively stabilises the output current. The setpoint is controlled by an analogue-to-digital converter (ADC). Each channel also has a modulation input via the analogue connector of the TBUS stack. It is connected to the frequency control module for the stabilisation of the laser frequency.

Frequency control module

The frequency control module provides all functions that are necessary to stabilise laser frequencies on a reference a.k.a. “to lock lasers“. The signal processing and feedback control is implemented on a FPGA. It has four channels of which one channel is dedicated to stabilise a laser on an atomic transition with spectroscopy and three are dedicated to stabilise the beat note of two lasers onto a radio frequency (RF) reference. Each channel has an output with a fast DAC to control the laser current.

Spectroscopy The EOM in the spectroscopy module (see figure 4.1) is driven by a 7 MHz signal which is generated on the FPGA, analogue converted and then amplified by an external amplifier [Mini-Circuits, ZHL-32A-S+]. The photodiode in the spectroscopy module is operated with a trans-impedance amplifier circuit [Kna13] with two output ports. The low pass filtered output signal is recorded using a slow input of the frequency control module. This was used to record the spectrum shown in figure 4.2. The high pass filtered and amplified photodiode signal is digitised by the fast ADC in the fast input channel of the frequency control module. On the FPGA, it is demodulated by a 7 MHz signal phase shifted with respect to the signal that drives the EOM to derive a dispersive signal which is used as the error signal to stabilise a laser on an atomic transition. This concept is also known as lock-in amplifier.¹

¹ The circuit can probably also be used for the Pound–Drever–Hall technique to stabilise a laser on a cavity, but this has not been tested yet. A reference cavity and spectroscopy on ultra-cold atoms would be an option to reduce the uncertainty of the effective wave vector further.

Beat note Having one laser stabilised on an atomic reference another laser can be stabilised with a frequency offset to the first laser. The optical beat note of the two lasers is recorded using a fast photodiode. This setup for QG-1 is described in [Gro17]. The frequency control module has programmable frequency dividers to keep the beat signal frequency within the limit of the frequency counters implemented on the FPGA. The difference between the frequency counter signal and the set point is the error signal for the digital feedback controller on the FPGA.

The module has a memory for a sequence of set points for all three channels. In each step the set point can either jump to a specified new value or linearly change the value at a given rate. With this technique, precise jumps and sweeps of the laser frequency can be controlled.

Digital oscilloscope and spectrum analyser The outputs of the feedback controller feature a triangle signal generator. A digital oscilloscope is implemented with a memory for the signal inputs. This is e.g. used for the acquisition of an atomic spectrum in the reference spectroscopy module to choose an appropriate atomic transition to lock the reference laser.

The signal memory enables the recording and read out of a continuous signal in a first in first out (FIFO) mode. From this signal a linear spectral density is calculated on the control computer. For example, this is used to characterise the in-loop frequency noise to optimise the feedback controller parameters. Figure 5.1 shows the in-loop noise spectral density for different values of the integrator gain and the proportional gain. The beat note signal has been recorded with the reference laser locked on the spectroscopy and the feedback controller parameters state in the legend for the slave laser stabilisation. The upper limit of the frequency range is given by the sampling rate. Currently, it is limited by the software and can be improved

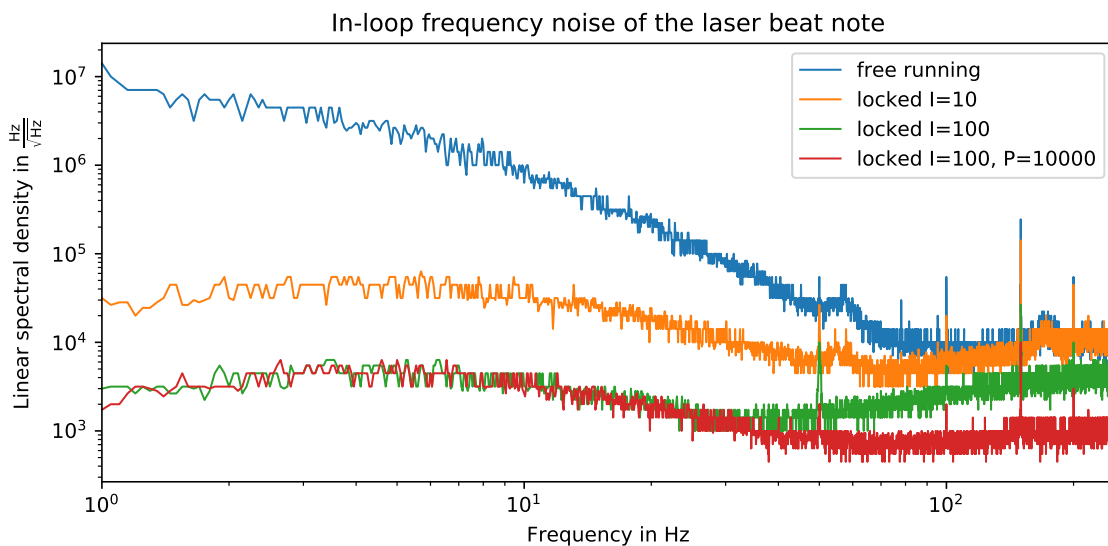


Figure 5.1: Linear spectral density of the in-loop beat note frequency signal for varied feedback controller parameters.

significantly.¹

DDS module

The DDS module features a DDS chip [Analog Devices, AD9958] with two independent output channels. Every 4 μ s it receives updated values for frequency, phase and amplitude over a serial interface from a FPGA. The FPGA has a memory for a sequence of values for frequency, phase and amplitude for each channel. In each step it can either jump to a new value or sweep at a constant rate. The AD9958 DDS chip has itself a sweep function for the frequency, but it is in the current version of the FPGA firmware not accessible. For the future use in accelerated Bragg gratings for atom interferometry this function should be activated with an FPGA firmware update.

The laser system electronic stack contains three DDS modules with in total six channels. Four channels are used to drive the AOMs in the distribution module (see [chapter 4](#)). For the AOM in the interferometry laser beam path, the output signals of two channels are combined using a RF mixer [Mini-Circuits, ZX05-11X+] to modulate the light field with two frequencies needed for a moving Bragg grating. The output stage of the DDS module provides 1 mW RF output power, which is amplified to a RF power of 1 W to drive the AOMs. One channel provides a 50 MHz reference to a phase-lock-loop (PLL) stabilising a VCO [Hittite, HMC834] at 6.6 GHz. This signal is used to modulate a sideband for repumping during MOT operation with a fibre coupled EOM (see [chapter 4](#)). By shifting the reference frequency, the VCO frequency can be shifted in the range of 6586 MHz to 6748 MHz. The sixth channel is operated for RF induced evaporation. It is connected via an 8 dB attenuator, a low pass filter [Mini-Circuits, SLP-30+] with a cut-off frequency of 32 MHz and a 25 dB amplifier [Mini-Circuits, ZHL-32A+] to a U-shaped RF antenna on the base layer of the atom chip.

Shutter driver module

The shutter driver module is based on a design for the MAIUS project. It features a FPGA with a memory for a sequence of shutter states: either open or closed. However, the output stage to drive the shutters has been custom designed by Nina Heine to drive the bi-stable shutters [Uniblitz, ES6B] implemented in QG-1 (see [chapter 4](#)). The FPGA firmware shares code and remains compatible with the MAIUS shutter driver. A specialised timing generator for the pulses needed for the operation of bi-stable shutters has been programmed by the author.

¹ The Labview user interface calls an external DLL library for the generation of the TBUS commands. The invocation of the external library consumes the most time and has to be repeated for every sample. If the TBUS commands are generated in Labview directly, the acquisition time for the single samples will be shortened. This would enable a faster sampling rate.

Photodiode module

The photodiode module monitors the light intensity of up to 25 connected photodiodes. The photodiodes are placed at relevant locations in the laser system and in the collimators at the sensor head. Monitoring data of the photodiodes is saved for every run of the experimental sequence. The photodiode signal is also used for intensity stabilisation of the laser cooling light. The instrumentation amplifier for each photodiode is located on the TBUS module and the photodiodes are connected with long cables which can pick up electromagnetic noise. To suppress the noise, a custom FPGA firmware with a digital low pass filter with a cut-off frequency of 22 Hz has been implemented.

5.2 Temperature stabilisation

The diode lasers and the crystals for frequency conversion need to be temperature stabilised. The temperature is regulated with peltier elements based on the thermo-electric effect. The control electronic is based on a commercial temperature controller [Meerstetter, TEC-1091]. On each module, a digital feedback controller is implemented on a micro controller. The feedback parameters can be set via a serial RS485 interface. The serial interfaces of all temperature controllers are connected to an Ethernet interface [Lantronix, XPort]. Parameters are set from a graphical user interface on the the experiment control computer which also provides monitoring and an autotune function for the feedback parameters. The temperature controllers and the Ethernet interface are mounted in an Eurocard enclosure which fits into a 19" rack mount together with the laser system stack.

5.3 Current driver stack

For the operation of the magneto-optical and magnetic traps, precise control of the currents in the atom chip structures and offset coils is required. The current driver electronics need to be able to provide currents up to 10 A while keeping the current noise level below $1\mu\text{A}/\sqrt{\text{Hz}}$. The design goal for the magnetic field switching time is shorter than 2 ms for the operation of the magnetic traps. However, for the application of a magnetic lens, a shorter switching time is beneficial. For a transportable experiment, a small mechanical footprint is required as well as keeping the heat dissipation of the electronic system low. These goals are in line with the design goals of the current drivers for the MAIUS mission. Therefore the same electronics modules based on the TBUS stack system have been implemented in QG-1. The electrical setup of the the MAIUS current drivers is described in detail in [Pop18]. In a test setup operating on a battery voltage supply a current noise spectral density below $1\mu\text{A}/\sqrt{\text{Hz}}$ has been demonstrated. With the same setup operating on a laboratory power supply the same noise floor could be achieved but with additional peaks with a spectral density on the order of $10\mu\text{A}/\sqrt{\text{Hz}}$ at certain frequencies e.g. at multiples of 50 Hz and at 3 kHz (cf. [Pop18, p. 103]).

Chip current drivers

For the realisation of magnetic traps within the scope of this thesis, the structures on the atom chip need to be supplied with a unipolar current. The design of the unipolar chip current driver (UCCD) is self regulating and employs a single ended class B stage [Pop18, p. 72] for the control of the output current. For the atom chip structures in QG-1, fast switching shorter than $400\mu\text{s}$ for output currents larger than 1.5A have been measured (see figure 5.2). The step response can be optimised further, as it is visible for the mesoscopic U current driver with a switch-on time of shorter than $100\mu\text{s}$.

Coil current drivers

For complete control over the strength and direction of the the homogeneous offset magnetic field generated by Helmholtz coils pairs (see section 3.2), bipolar coil current drivers (BCCD) capable of driving inductive loads are needed. A self regulating design was chosen which controls the output current with a MOSFET based H-bridge [Pop18, p. 76]. For this circuit, only a single unipolar current supply is needed for bipolar operation.

The BCCD's feedback controller is based on discrete proportional, integral and differential (PID) stages with individual configurable gains to tune the response of the feedback loop. The switching time of the output current depends on the setpoint and is ultimately limited by the inductance of the coils. For short switching times the feedback controller should be configured as fast as the inductance of the coil allows, but not faster as this would induce oscillations. Therefore, the electronic circuit has been optimised using the simulation software TINA-TI [Tex08] based on the SPICE algorithm [Cox92; Nag73]. To verify the simulation results, the actual switching time of the current drivers connected to the QG-1 apparatus has been characterised with a current measurement on the connection cables using a magnetic field probe [Aim-TTi, I-Prober 520]. The measurement has been performed for various output currents. The setpoint is set to the desired output current during the time $0\text{ms} < t < 100\text{ms}$. For time $t < 0\text{ms}$ and $t > 100\text{ms}$ the setpoint is 0A . Figure 5.3 shows the measured output current of the Y coil current driver. For currents smaller than 2.5A the switch-on time is faster than 2ms and the switch-off time is faster than 0.5ms . For magnetic lensing, shorter switching times are required. As the switching time is ultimately limited by the inductance of the coil, a

Table 5.1: Number of windings for different configurations of the Helmholtz coil pairs.

	Inner windings per coil	Outer windings per coil	Combined windings per coil
X coil pair	17	51	68
Y coil pair	15	45	60
Z coil pair	-	-	35

special configuration with smaller coils with one fourth of the total number of windings (see [table 5.1](#)) can be used. An additional current driver tuned for a lower inductance is connected via an additional tap to the two innermost layers of windings of the X coil pair and Y coil pair. The resulting switching times shorter than 400 μs are depicted in [figure 5.4](#).

Power module and Ethernet interface module

These modules are the same as for the laser system stack (see [section 5.1](#)). However, in this TBUS stack, the bus synchronisation clock is set to 10 MHz as it is required for the latest version of the current driver FPGA firmware.

Chip safety board

To protect the atom chip wire structures from failures of the electronic system, a chip safety electronic board [[Pop18](#), p. 90] disconnects the structures when not in use. During operation the current as well as the operation time is monitored. When the current exceeds the configured limit, the switches disconnect the atom chip and the safety board switches into an error state which needs to be manually reset. An additional limit is set for the operation time. When the timeout duration is reached, the atom chip will be disconnected.

Alternating control of small and big coils

The same safety electronic board is installed at the coil connections to connect them to alternating current drivers. A current driver tuned for large inductance will be connected to all windings of each coil pair for large magnetic field strengths and a current driver tuned for low inductance will be connected via additional taps to the inner windings of the X and Y coils pairs to allow fast switching of the magnetic field for magnetic lensing. The safety limits are also in place to prevent the coils from overheating. Additionally, disconnecting the coils when not in use ensures that the coils are current-free during the interferometry phase of the sequence.

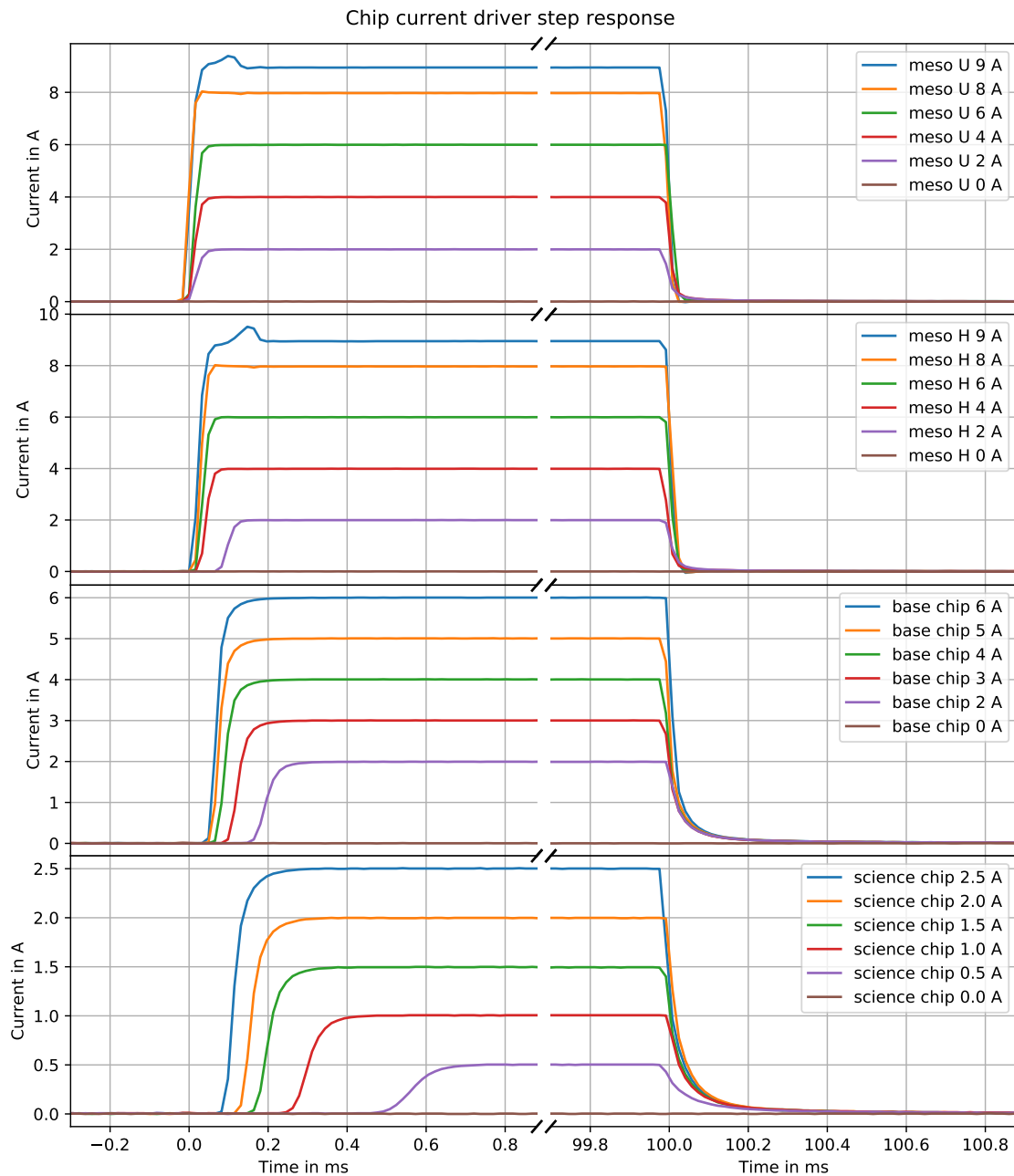


Figure 5.2: Step response of the respective unipolar chip current driver for the atom chip structures for different output current setpoints. The setpoint is non-zero for times $0\text{ms} < t < 100\text{ms}$. The switch-on times for all current drivers for output currents larger than 1.5 A are shorter than 400 μs . For a setpoint of 9 A, the current drivers show an instability after switch-on. However, it reaches a stable state within 200 μs after the trigger.

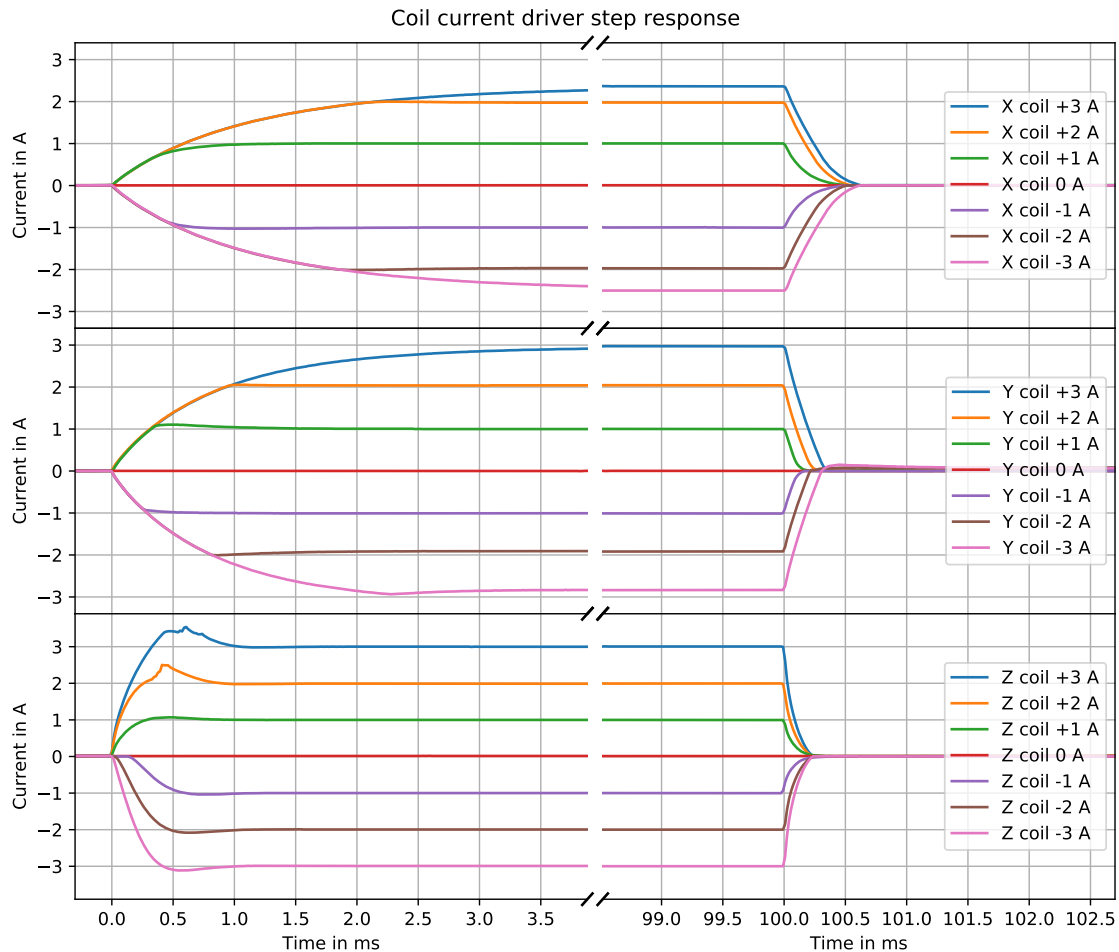


Figure 5.3: Step response of the respective bipolar coil current driver for different output current setpoints. The setpoint is non-zero for times $0\text{ms} < t < 100\text{ms}$. For each setpoint, the switch-on time until the setpoint is reached and the output is stable can be derived from the measurement. All measurements have the same calibrated zero offset. As the output current is never true 0 A, for the X and Y coil current driver a small negative output current is flowing before the trigger. This is apparent in the shorter switch-on time for negative output currents. For the Y current driver, the zero offset is a small positive value and the switch-on time for positive output currents is shorter. By a variation of the zero offset this behaviour can be reversed.

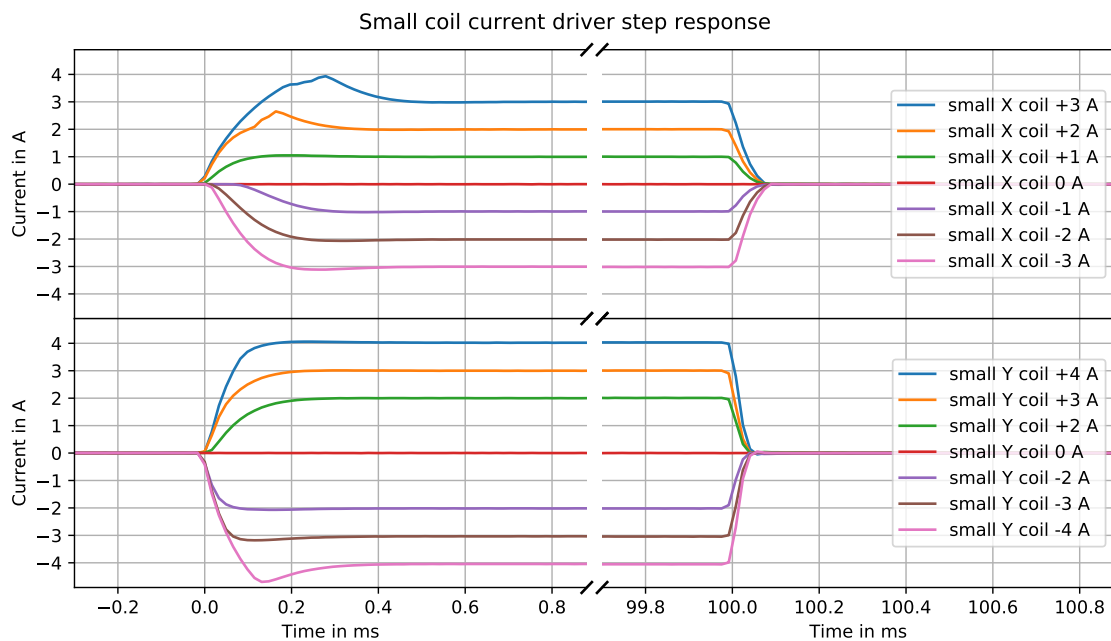


Figure 5.4: Separate bipolar coil current drivers are tuned for lower inductance and connected to one fourth of the windings of the X and Y coil pairs respectively. The output current setpoint is non-zero for times $0\text{ms} < t < 100\text{ms}$. The step response is depicted for various setpoints. All measurements have the same calibrated zero offset. As the output current is never true 0A, for the small Y coil current driver a small negative output current is flowing before the trigger. This is apparent in the shorter switch-on time for negative output currents. For the X current driver, the zero offset is a small positive value and the switch-on time for a positive output current of 1 A is shorter. By a variation of the zero offset this behaviour can be reversed.

5.4 FPGA for analogue signals

A FPGA module with high resolution ADCs and DACs [National Instruments, NI USB-7855R] is used to record analogue signals synchronised with the experimental sequence with a sampling rate of 1 MHz and a resolution of 16 bit. It has an internal oscillator generating a 40 MHz output frequency, which is converted to 20 MHz and distributed as a reference clock to the TBUS electronic stacks. The general purpose digital in-/ouputs (GPIO) on the module are used to control and monitor the chip safety boards.

5.5 Transportable rack

The laser and electronic system will be mounted into a 140 x 80 x 80 cm³ rack on wheels which has a volume of less than a cubic meter. The rack features a temperature stabilisation to improve the stability of the laser system in unstable environments. The temperature control is based on peltier elements instead of a conventional compressor to prevent vibrations. The sensor head will be connected with up to 10m long optical and electrical cables. No other components need to be connected or assembled, ensuring a fast set up time in the field.

5.6 Computer control

The experimental sequence which is executed on the electronic modules described above can be edited and send to the hardware using a graphical user interface. It is based on the Labview user interface created by Sebastian Bode for the QPort apparatus¹ and has been adopted with a custom hardware interface for the QG-1 apparatus within the scope of this thesis. It can run multi-dimensional parameter scans by linearly incrementing a set of specified values in the sequence as well as an optimisation routine based on the differential evolution (DE) method. A feedback controller was added to the software to implement an intensity stabilisation of the laser cooling light field. The same feedback method can be used in gravity measurements to lock the sweep rate α of the accelerated Bragg grating on mid fringe measurements of the atom interferometer phase. The control software presents a robust foundation for future additions for the operation of a gravimeter. For example, an auto lock routine for the reference laser can later be added with the goal to measure gravity with the push of a single button.

¹ PhD thesis in preparation

Part II

Magnetic trapping

CHAPTER 6

Atom-chip-based magnetic traps

In QG-1 an atom chip is used to prepare an ultra-cold atomic ensemble as test mass for the gravimeter. Atom chips produced by photolithography feature microscopic wire structures. Various wire configurations can be produced on a single chip substrate to realise multiple trap geometries. As the loading of the trap and the evaporative cooling have different requirements on the trap properties, two trap configurations are implemented: First, a shallow trap optimised for the initial loading of a high number of atoms is realised and then the confinement is increased by adiabatically changing the trap potential to a steep consecutive trap for effective evaporative cooling. This chapter will introduce the techniques for magnetic trapping using the conducting structures on the three-layer atom chip and present the results of a simulation of the used trap configurations.

6.1 Magnetic trapping of neutral atoms

A static magnetic field with a curvature is used to create a potential with a local minimum for atoms with a magnetic moment. The energy levels of the internal atomic states are shifted by the coupling between the magnetic moment of the atom $\vec{\mu}$ and an external magnetic field \vec{B} . This phenomenon has first been reported by Pieter Zeeman [Zee97] and is called Zeeman effect. The resulting potential at position \vec{r} is dependent on the magnetic field strength $B(\vec{r})$ as well as the orientation of the magnetic moment $\vec{\mu}$ with respect to the direction of the magnetic field and given as

$$V(\vec{r}) = -\vec{\mu} \cdot \vec{B}(\vec{r}). \quad (6.1)$$

For atoms with a single electron in the outer shell, such as alkali metals, and for weak magnetic fields, such that the Zeeman shift is small¹ compared to the hyperfine splittings, only the magnetic moment of the outer electron is relevant. The magnetic moment of the nucleus is neglected as it is orders of magnitudes smaller than the magnetic moment of the electrons

¹ For Rubidium this is the case for magnetic field strengths smaller than 10 mT (100 G).

[confer [Ste15](#)]. Therefore, the shift can be expressed as

$$V(\vec{r}) = \mu_B g_F m_F B(\vec{r}), \quad (6.2)$$

with the electron spin quantum number m_F , the Bohr magneton μ_B and the hyperfine Landé factor g_F for the hyperfine state $|F\rangle$. The potential energy of magnetic sublevels with a positive $m_F \cdot g_F$ term is minimal for a local minimum of the magnetic field. These magnetic sublevels are hence called low-field seekers, whereas magnetic sublevels with a negative $m_F \cdot g_F$ term are called high-field seekers. Only low-field seekers can be trapped, because in regions free of currents a static magnetic field can only have a local field minimum but not local maximum according to Earnshaw's theorem. The hyperfine ground state $|5S_{1/2}, F=2\rangle$ of ^{87}Rb has a positive Landé factor g_F . Therefore, the magnetic sublevels $m_F = +1$ and $m_F = +2$ are low-field seekers and magnetically trappable.

To prevent losses due to spin-flip Majorana transitions [[Bri06](#)], the magnetic trap needs to have a non-zero magnetic field strength at the location of the atomic ensemble. A magnetic trap with a non-zero potential minimum has been suggested [[Pri83](#)] and demonstrated [[Bag87](#)] by David E. Pritchard implementing a magnetic field configuration similar to the Ioffe configuration for plasma confinement. For the trapping of neutral atoms, this type is referred to as Ioffe-Pritchard trap.

6.2 Atom chip

Atoms can be trapped in proximity to current carrying wires build on-top a substrate by combining their magnetic field with a homogeneous offset field. A Ioffe-Pritchard trap can be realised with a Z or H shaped wire structure [[Rei11](#), p. 43]. It has first been realised on an atom chip by [[Rei02](#)]. Other configurations are possible but they are not within the scope of this thesis. To realise traps of different volumes, the atom chip in the QG-1 apparatus features three layers with structures of different sizes. The respective structures on each layer of the QG-1 atom chip to generate a Ioffe-Pritchard trap are highlighted in orange in [figure 6.1](#). The closer the layers are to the atoms, the thinner the wires and the higher the resulting trap confinement. These three layers are:

Mesoscopic layer The mesoscopic copper wires on the chip mount have a cross-sectional area of 0.65 mm^2 and carry currents up to 10 A. The mesoscopic U structure, depicted in blue in [figure 6.1\(a\)](#), is used to create the magnetic field for the MOT. Highlighted in orange is the mesoscopic H structure which realises large volume magnetic traps with weak confinement.

Base chip layer The base chip features gold wires with a cross-sectional area of $1000 \mu\text{m}^2$ for currents up to 5.6 A. The structures shown in [figure 6.1\(b\)](#) can be connected in various configurations to electrical current sources. The only configuration used within the scope

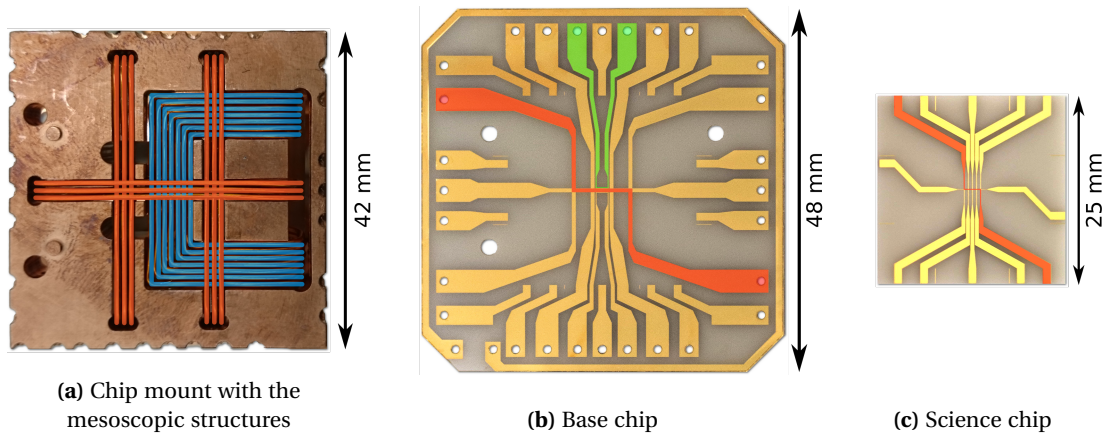


Figure 6.1: Layers of the atom chip. The images are printed on a 1:1 scale. The wire structures used for Ioffe-Pritchard traps in this chapter are marked in orange: The mesoscopic H on the chip mount, the outer Z on the base chip and the outer Z on the science chip. The mesoscopic U for the quadrupole field of the MOT is marked in blue on the chip mount. Highlighted in green on the base chip is the RF antenna used for forced RF evaporation and RF spectroscopy.

of this thesis is the outer Z structure marked in orange. The base chip features also an U-shaped RF antenna for the coupling of the magnetic sublevels using RF transitions for forced evaporation illustrated in green.

Science chip layer The science chip is closest to the atoms and provides gold wire structures with a cross-sectional area of $500 \mu\text{m}^2$ for currents up to 2 A. The resulting traps have a strong confinement due to the high magnetic field gradient in proximity to the wires. The outer Z structure used for the traps described in this thesis is highlighted in orange in figure 6.1(c).

6.3 Simulation

A simulation of the trap potential is a valuable tool for the optimisation of a magnetic trap, as it gives direct access to the properties of the trap. To be able to estimate how the experimental parameters change the trap confinement and the three-dimensional position of the trapped ensemble, the current carrying chip structures and coils in the QG-1 apparatus have been modelled within the scope of the Master's thesis of Jan Philipp Barbey [Bar18]. The trap potential is calculated using a numerical simulation of the magnetic field implemented by Prof. Reinhold Walser based on the method detailed in [Her13, p. 91]. From the simulation, the following important properties of a trap can be derived:

Eigenfrequencies The trap potential can be approximated as a three-dimensional harmonic oscillator with Eigenaxes x', y', z' and Eigenfrequencies $\omega'_x, \omega'_y, \omega'_z$. The higher the frequency

the smaller the Gaussian width of the atomic ensemble and the higher the atom density for a given temperature and atom number. The geometrical mean ω_{geo} of the Eigenfrequencies is a measure for the confinement in the trap and is defined as

$$(\omega_{\text{geo}})^3 = \omega_{x'} \omega_{y'} \omega_{z'}. \quad (6.3)$$

Field at the trap minimum The magnetic field strength $|B|$ in the potential minimum can be determined via radio frequency spectroscopy (see [section 9.1](#)). In the absence of external fields, the trap potential minimum is at the same position as the magnetic field minimum. By taking gravity into account, the position of the trap potential minimum is shifted.

Trap depth The trap depth is the difference between the trap potential minimum V_{min} and the smallest local maximum of the trap potential V_0 , where atoms with energies $\varepsilon > V_0 - V_{\text{min}}$ can leave the trap. To prevent losses caused by atoms with high kinetic energy leaving the trap, the temperature of the atomic ensemble T_{at} has to fulfil the condition

$$\eta k_{\text{B}} T_{\text{at}} < V_0 - V_{\text{min}}, \quad (6.4)$$

with empirical values for $\eta = 5 \dots 7$ according to [[Rei11](#), p. 38]. In the following a value of $\eta = 7$ will be used.

In this thesis, two basic trap configurations are used: The initial trap ① needs a high trap volume with low Eigenfrequencies and has a higher distance to the chip than the consecutive compressed trap with strong confinement and high trap frequencies in close proximity to the chip surface. For the the compressed trap, two configurations are used: ② and ③. During optimisation of the evaporative cooling sequence it was shown, that in trap configuration ③ with a higher magnetic field strength at the trap minimum a higher evaporation efficiency can be achieved than in trap configuration ②. For these three trap configurations, the empirically found optimum currents and the resulting trap properties are given in [table 6.1](#). [Figure 6.2](#) shows the simulated potentials of the configurations ① and ③ for the $m_F = +2$ sublevel.

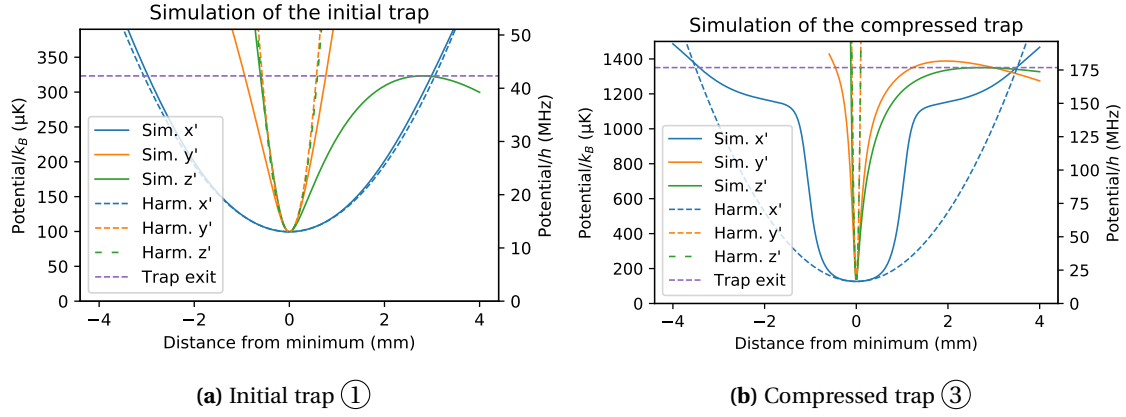


Figure 6.2: Numerical simulation of the trap potential for the parameters stated in table 6.1. The potential is approximated as a harmonic oscillator with the Eigenaxes x' , y' and z' . Both potentials are plotted along the Eigenaxes.

Table 6.1: Input and output parameters of the magnetic trap simulation. Eigenfrequencies and Eigenaxes are derived for the harmonic approximation at the trap minimum.

	Initial trap ①	Compressed trap ②	Compressed trap ③	
Input	Meso. H current	8.53 A	<i>off</i>	<i>off</i>
	Base chip current	4.86 A	4.86 A	4.86 A
	Science chip current	<i>off</i>	1.86 A	1.86 A
	X coil pair current	-0.37 A	-0.08 A	0.10 A
	Y coil pair current	-1.79 A	-2.92 A	-2.92 A
	Z coil pair current	-0.27 A	<i>off</i>	0.04 A
Output	X offset field component B_x	-269 μ T	-52 μ T	92 μ T
	Y offset field component B_y	-1468 μ T	-2425 μ T	-2425 μ T
	Z offset field component B_z	-175 μ T	3.8 μ T	27 μ T
	Eigenaxis x' frequency $\omega_{x'}/2\pi$	11 Hz	24 Hz	22 Hz
	Eigenaxis y' frequency $\omega_{y'}/2\pi$	58 Hz	1667 Hz	808 Hz
	Eigenaxis z' frequency $\omega_{z'}/2\pi$	56 Hz	1677 Hz	812 Hz
	Field B at trap minimum	177 μ T	45 μ T	195 μ T
Trap depth ($V_0 - V_{\min}$)	$7k_B \cdot 32\mu$ K	$7k_B \cdot 181\mu$ K	$7k_B \cdot 175\mu$ K	

CHAPTER 7

Loading of the magnetic trap

To optimise the mode-match between the MOT (see [section 3.2](#)) and the initial magnetic trap, two techniques described in detail in [\[Sah19\]](#) are applied in QG-1: Before the atomic ensemble is released from the MOT, the magnetic field gradient is increased and the laser frequency red detuned, which leads to a compression of the ensemble. This method is called compressed MOT (CMOT). Second, polarisation gradient cooling is applied to reduce the temperature to $6\ \mu\text{K}$. Afterwards, the atoms are equally distributed over the magnetic sublevels $m_F = -2, -1, 0, +1, +2$ of the hyperfine ground state $|5S_{1/2}, F = 2\rangle$. Only the magnetic sublevel $m_F = +2$ will be confined in a strong trap. Hence, for effective loading of the initial magnetic trap, the atoms should be prepared in the $m_F = +2$ sublevel.

7.1 Optical state preparation

Optical pumping is used to increase the atom number in the trappable magnetic sublevel. To break the degeneracy of the magnetic sublevels, a homogeneous magnetic field is applied to shift the energy levels as described by the Zeeman effect. The atoms are exposed to circular polarised light from the detection collimator parallel to the direction of the magnetic field, such that the light is resonant with the σ^+ transition between $|5S_{1/2}, F = 2\rangle$ and $|5P_{3/2}, F = 2\rangle$ increasing the m_F quantum number by $+1$ for each optical transition. Subsequently the excited state decays to the ground state. This process is repeated several times until the atoms are accumulated in the $|5S_{1/2}, F = 2, m_F = +2\rangle$ state, which is dark to the σ^+ light as the excited $|5P_{3/2}, F = 2\rangle$ hyperfine state has no $m_F = +3$ magnetic sublevel.

In the experiment, a homogeneous magnetic field of $430\ \mu\text{T}$ ($4.3\ \text{G}$) is applied parallel to the collimated pump light beam with circular polarisation. In [figure 7.1](#) the resulting atom number in the initial magnetic trap is depicted for positive and negative sign of the magnetic field. This switches the orientation of the atomic momentum with respect to the helicity of the light. Optical pumping to the $m_F = +2$ substate is plotted in blue whereas pumping to the not trappable high field seeking substate $m_F = -2$ is shown in red. As a reference the atom number without pump light is depicted in grey. The average of the reference measurements is $8.6 \cdot 10^6$ atoms. Compared to this value optical pumping improves the atom number in the initial magnetic trap by a factor of 3.27 at a detuning of $+9\ \text{MHz}$.

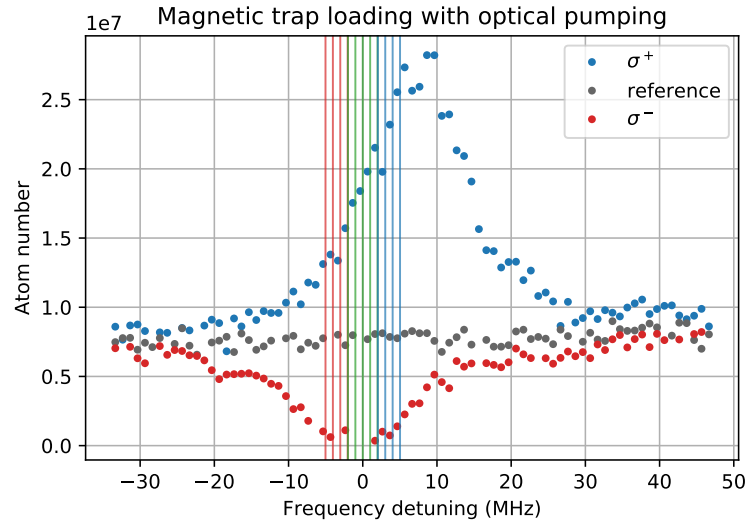


Figure 7.1: Atom number in the initial magnetic trap in dependence of the light frequency detuning from the $|5S_{1/2}, F = 2, m_F = 0\rangle$ to $|5P_{3/2}, F = 2, m_F = 0\rangle$ transition during the optical pumping phase. The measurement is taken for different orientations of the magnetic field such that the circular polarised light drives either the σ^+ (blue) or σ^- (red) transition. A reference measurement without optical pumping is depicted in grey. Vertical lines indicate the theoretical frequencies of the transitions between the magnetic substates given by the Zeeman shift for a homogeneous magnetic field of $430 \mu\text{T}$ (4.3 G). Green lines represent π transitions with $\Delta m_F = 0$, whereas σ^+ transitions are blue and σ^- transitions are red. This measurement data has previously been published in [Sah19].

7.2 Mode matching

To improve the loading of the magnetic trap the overlap with the CMOT needs to be optimised. One figure of merit is the transferred atom number. On the other hand no oscillations of the centre of mass (COM) position should be excited, because these can lead to heating and affect the subsequent compression step. After optimising the loading of the initial magnetic trap only on the atom number, a damped oscillation on the weak trap axis with an amplitude in the trap of $180 \mu\text{m}$ was observed for holding times between 240 ms and 450 ms. By shifting the CMOT position, this amplitude could be reduced to $69 \mu\text{m}$ while also reducing the loading efficiency by a factor of two.

To achieve both goals, high atom number and low oscillation amplitude, the position of the CMOT as well as of the initial magnetic trap are varied. This would be a 6-dimensional parameter scan over a wide range. To reduce the number of measurements, the respective coil pair currents creating the homogeneous offset field, which shifts CMOT and magnetic trap along the same axis, are evaluated simultaneously in a 2-dimensional parameter scan. The magnetic trap position can not be significantly moved along the weak trap axis with the homogeneous offset field. Instead the magnetic field strength at the trap bottom is scanned against the CMOT position along this axis. After each measurement, the optimum parameter

pair is applied for the next iteration.

For each parameter pair, the oscillation over the holding time is recorded. To quantify the amplitude of the oscillation, the model

$$y_{\text{detect}}(t) = y_{\text{trap}}(t) + t_{\text{TOF}} \cdot \dot{y}_{\text{trap}}(t) + y_{\text{center}} \quad (7.1)$$

is fitted to the data. However, the least-squares regression algorithm is unreliable for periodic models, because the problem has multiple minima for the phase. This is circumvented by expressing the oscillation in the trap as

$$y_{\text{trap}}(t) = A_1 \sin(\omega t) + A_2 \cos(\omega t). \quad (7.2)$$

Now, the in-trap amplitude is given by $A_{\text{trap}} = \sqrt{(A_1)^2 + (A_2)^2}$ and the phase is given by $\varphi = \arctan2(A_2, A_1)$ using the 2-argument arctangent function $\arctan2$ [Wik19]. To further improve the reliability of the fit algorithm, a guess for the oscillation frequency $f = \omega/(2\pi)$ is provided using the frequency with the strongest amplitude found in the discrete spectrum. It is calculated using the Fast Fourier Transform (FFT) algorithm.

Immediately after loading the trap, a high dynamic motion can be observed while the ensemble is rethermalising. The oscillation is evaluated separately for the rethermalisation phase and for longer holding times with the boundary chosen at 240 ms. Using this method, the respective positions of the CMOT and the initial magnetic trap have been optimised in 9 iterations on a high loaded atom number and low excitation both during the rethermalisation

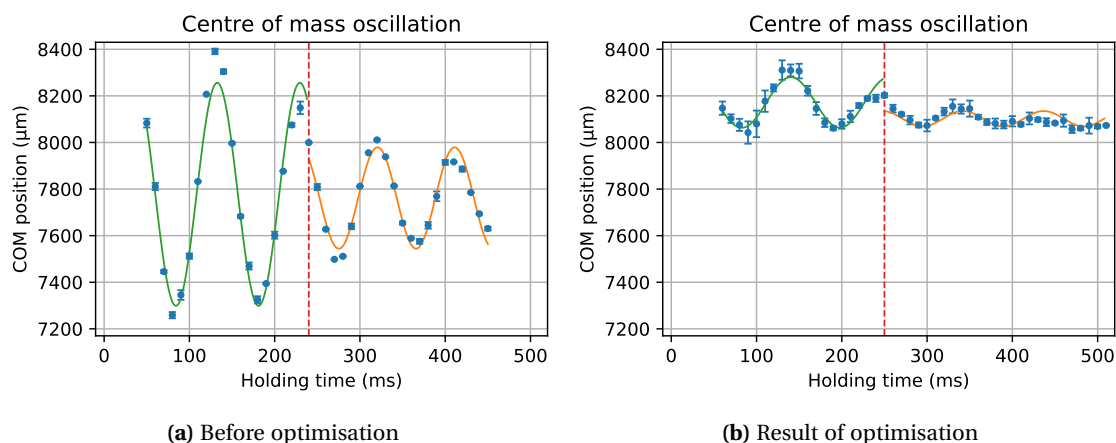


Figure 7.2: Centre of mass (COM) oscillation after loading the initial magnetic trap. The measured COM positions after 20 ms time of flight have been determined by fitting a Gaussian distribution to an absorption image of the atomic ensemble. These are depicted as blue dots with error bars showing the standard deviation of 2 (a) or 5 (b) repetitions. The fitted models for a harmonic oscillation during rethermalisation phase and for longer hold times are plotted as green and orange lines, respectively.

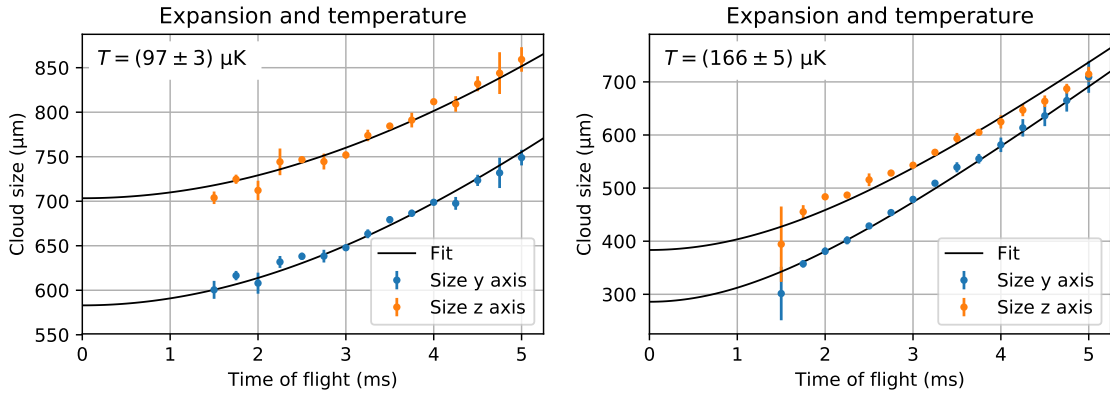
phase and for holding times between 240 ms and 540 ms.

The resulting motion after optimisation is shown in [figure 7.2\(b\)](#). Also visible is the shifted $y_{2,\text{center}}$ compared to [figure 7.2\(a\)](#). The residual amplitude is $32\ \mu\text{m}$. The oscillation has been reduced by a factor of 6 while not affecting the loading efficiency. The oscillation is damped by the anharmonicity of the trap and is smaller than the statistical error for holding times longer than 400 ms. Loading the atoms into a steeper trap and adding dispersion in the form of forced evaporation dampens the oscillation further.

7.3 Temperature in the magnetic trap

After capturing the atoms in the initial magnetic trap ① with large volume, they are transferred to a compressed trap ② to increase density and rethermalisation rate. The compressed trap is created by the currents in the science chip and the base chip given in [table 6.1](#). The current through the science chip Z structure is immediately switched on whereas the other currents are linearly ramped to the values of the compressed trap over a duration of 100 ms. As the atomic ensemble is being adiabatically compressed, the temperature rises. The respective temperature in the initial and the compressed magnetic trap is determined by releasing the atoms from the trap and recording a time of flight series of the width of the Gaussian cloud. The measured expansion can be seen in [figure 7.3](#). The following model for the thermal expansion is utilised to determine the temperature: The Gaussian width σ_i after expansion time t_{TOF} is given by

$$\begin{pmatrix} \sigma_y(t_{\text{TOF}}) \\ \sigma_z(t_{\text{TOF}}) \end{pmatrix} = \begin{pmatrix} \sqrt{(\sigma_{0,y})^2 + k_B T_{\text{at}} / m (t_{\text{TOF}})^2} \\ \sqrt{(\sigma_{0,z})^2 + k_B T_{\text{at}} / m (t_{\text{TOF}})^2} \end{pmatrix}, \quad (7.3)$$



(a) Expansion of the Gaussian cloud after release from the initial magnetic trap ①.

(b) Expansion of the Gaussian cloud after release from the compressed trap ②.

Figure 7.3: Temperature determination of the atomic ensemble after release from the magnetic trap. The depicted size is the width σ of a Gaussian distribution fitted to the atom density acquired via absorption imaging. A model for the expansion in two dimensions has been fitted to the data.

with the Boltzmann constant k_B and the atomic mass m . The parameters temperature T_{at} and initial size $\sigma_{0,y}, \sigma_{0,z}$ are fitted to the data.

After loading the polarisation gradient cooled atomic ensemble with a temperature of $(6.6 \pm 0.7) \mu\text{K}$ into the initial trap, the temperature increases to $(97 \pm 3) \mu\text{K}$. This temperature is higher than the estimated trap depth¹ in section 6.1 of $7k_B \cdot 32 \mu\text{K}$ and might lead to a loss of atoms due to evaporation. Compressing the magnetic trap increases the temperature further to $(166 \pm 5) \mu\text{K}$ while also increasing the estimated trap depth to $7k_B \cdot 181 \mu\text{K}$.

7.4 Loading efficiency and saturation of the magnetic trap

In every step, loading the polarisation gradient cooled atoms into the initial trap and compressing the trap, atoms are lost. The efficiency of the magnetic trap loading procedure is given by the atom number in the final compressed trap after 20 ms holding time compared to the initial atom number in the MOT. To characterise the saturation of the loading efficiency for higher atom numbers in the MOT, the efficiency is determined for different MOT atom numbers by varying the MOT loading time.

The resulting atom numbers are depicted in figure 7.4 (a similar figure is shown in [Sei14, p. 69] for the MAIUS-A apparatus). The optimum loading efficiency is 27 % at a MOT loading time of 200 ms. The loading efficiency in the initial magnetic trap is mostly limited due to a

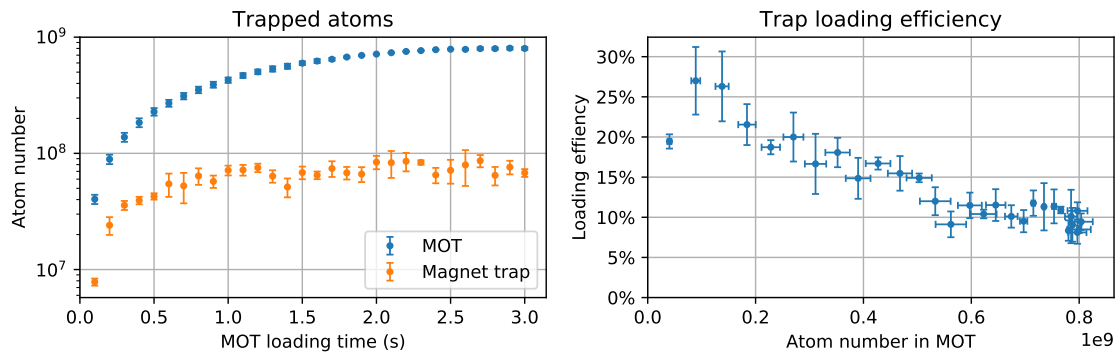


Figure 7.4: Characterisation of the magnetic trap loading efficiency. The left plot shows the atom number in the MOT (blue) and the atom number in the final compressed magnetic trap (orange) versus the MOT loading time. The atom number in the MOT is derived from the fluorescence of the atoms during MOT loading and the atom number in the magnetic trap after 20 ms hold time is acquired via absorption detection. The right plot shows the loading efficiency calculated for each single shot. The data points are averaged over three repetitions and the errors bars depict the standard deviation.

¹ Here, the trap depth $V_0 - V_{\text{min}} = \eta k_B T_{\text{max}}$ is stated in terms of the maximal temperature T_{max} of an ensemble that is confined in the trap with negligible losses due to evaporation with an empirical value of $\eta = 7$ [Reil1, p. 38].

poor match of the aspect ratio of the CMOT and the initial magnetic trap, because the weak trap axis of the MOT is perpendicular to the weak trap axis of the magnetic traps (see [section 3.3](#)). However, the size of the polarisation gradient cooled ensemble increases for longer MOT loading times and affects the magnetic trap loading efficiency. To maximise the transferred atom number, the system is operating with a MOT loading time of 700 ms, which leads to bigger cloud sizes and limits the magnetic trap loading efficiency further to 17 % resulting in $5.3 \cdot 10^7$ atoms in the compressed magnetic trap. In comparison [\[Sei14\]](#) demonstrated an atom number of $1.8 \cdot 10^8$ in the compressed magnetic trap after 800 ms MOT loading time in the MAIUS-A apparatus, where the weak trap axes of MOT and magnetic trap are aligned.

CHAPTER 8

Trap characterisation

The next step after the transfer to the compressed magnetic trap is evaporative cooling, which is described in [chapter 9](#). As mentioned before, the Eigenfrequencies and the loss rate are two important characteristics for evaporative cooling and will be analysed in this chapter.

8.1 Lifetime of the trapped ensemble

There are several mechanisms leading to atom loss in the trap, e.g. background gas collisions caused by the intrinsically worse vacuum quality in proximity to the atom chip. However, the residual pressure is estimated to be less than $10 \cdot 10^{-10}$ hPa in the main chamber¹. Another loss

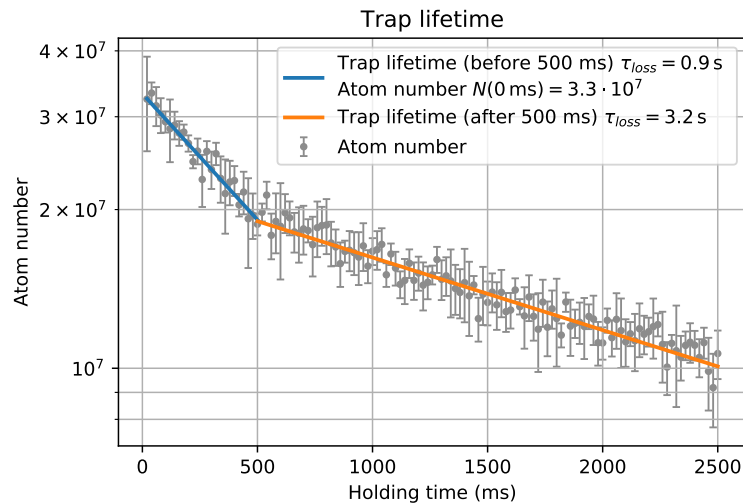


Figure 8.1: Lifetime measurement of the atomic ensemble in the magnetic trap. The atom number in the compressed magnetic trap ② in dependence of the holding time is depicted as grey dots with error bars indicating the standard deviation over five repetitions. An exponential decay model is fitted to the data for holding times longer than 500 ms giving a lifetime of 3.2 s and represented as orange line. The initial decay in the first 500 ms has a lifetime of 0.9 s and is shown as blue line.

¹ less than $10 \cdot 10^{-11}$ hPa at the pressure sensor, see [section 3.5](#).

channel for atomic ensembles with temperatures as high as the trap depth is particles with high kinetic energy escaping the trap. These loss mechanisms depend on the atom number N in the trap and can be characterised by the loss rate λ

$$\frac{dN}{dt} = -\lambda N, \quad (8.1)$$

which leads to an exponential decay

$$N(t) = N_0 \exp^{-t/\tau_{\text{loss}}}, \quad (8.2)$$

with the mean lifetime $\tau_{\text{loss}} = \frac{1}{\lambda}$.

The remaining atom number in the trap has been measured via absorption detection and is plotted versus the holding time in [figure 8.1](#). Fitting the exponential decay model to the data determines a trap lifetime of 3.2 s for holding times longer than 500 ms. The initial decay in the first 500 ms is much faster than the long-term decay because of rethermalisation processes and has a fitted lifetime of 0.9 s. After 500 ms holding time $1.9 \cdot 10^7$ atoms remain in the trap.

8.2 Eigenfrequencies

The Eigenfrequencies are a measure for the confinement of a harmonic trap as described in [section 6.1](#). To compare the simulated results to the actually implemented trap in the experiment, the Eigenfrequencies are measured by exciting an oscillation and detecting the position of the atomic ensemble in dependence of the duration of the oscillation.

An oscillation along the y axis (chip coordinate system see [figure 3.5](#)) is excited by shifting the trap potential in y direction at holding time $t = 0$ ms. [Figure 8.2\(a\)](#) shows the COM position after a time of flight of $t_{\text{TOF}} = 5$ ms in dependence of the holding time for a trap with $I_{\text{coil}} = (-0.08, -2.19, 0)$ A.

The following model is fitted to the data. Consider a damped harmonic oscillator

$$y_{\text{trap}}(t) = A_0 e^{-\delta t} \cos(\omega_d t + \varphi), \quad (8.3)$$

with a damping constant δ , phase φ , amplitude A_0 , damped angular frequency $\omega_d = \sqrt{\omega^2 - \delta^2}$ and harmonic Eigenfrequency $\omega = 2\pi f$. As the COM position is detected after a TOF of $t_{\text{TOF}} = 5$ ms, it is also dependent on the COM velocity in the trap at release:

$$y_{\text{detect}}(t) = y_{\text{trap}}(t) + t_{\text{TOF}} \cdot \dot{y}_{\text{trap}}(t) + y_{\text{centre}}, \quad (8.4)$$

with the time t in the trap.

The same measurement is done for several currents in the y coil for an excitation along both strong trap axes y and z respectively. The fitted frequencies are shown in [figure 8.2\(b\)](#) together with the simulated trap frequency for the strong Eigenaxis. Only the simulated fre-

quency for the z' Eigenaxis is plotted, because it differs from the simulated y' Eigenfrequency by less than 1%. The trap frequency in the weak Eigenaxis is simulated to be 25 Hz and measured separately as 20 Hz. The compressed trap ② with parameters given in table 6.1 has simulated trap Eigenfrequencies $\omega_{\text{sim}}/2\pi = (25, 1446, 1452)$ Hz with the geometric mean $\omega_{\text{geo,sim}}/2\pi = 374$ Hz. The frequencies were measured to be $\omega_{\text{meas}}/2\pi = (20, 1055, 1063)$ Hz. Therefore, the compressed trap ② has an empirical geometrical mean of the trap Eigenfrequencies of $\omega_{\text{geo,meas}}/2\pi = 282$ Hz.

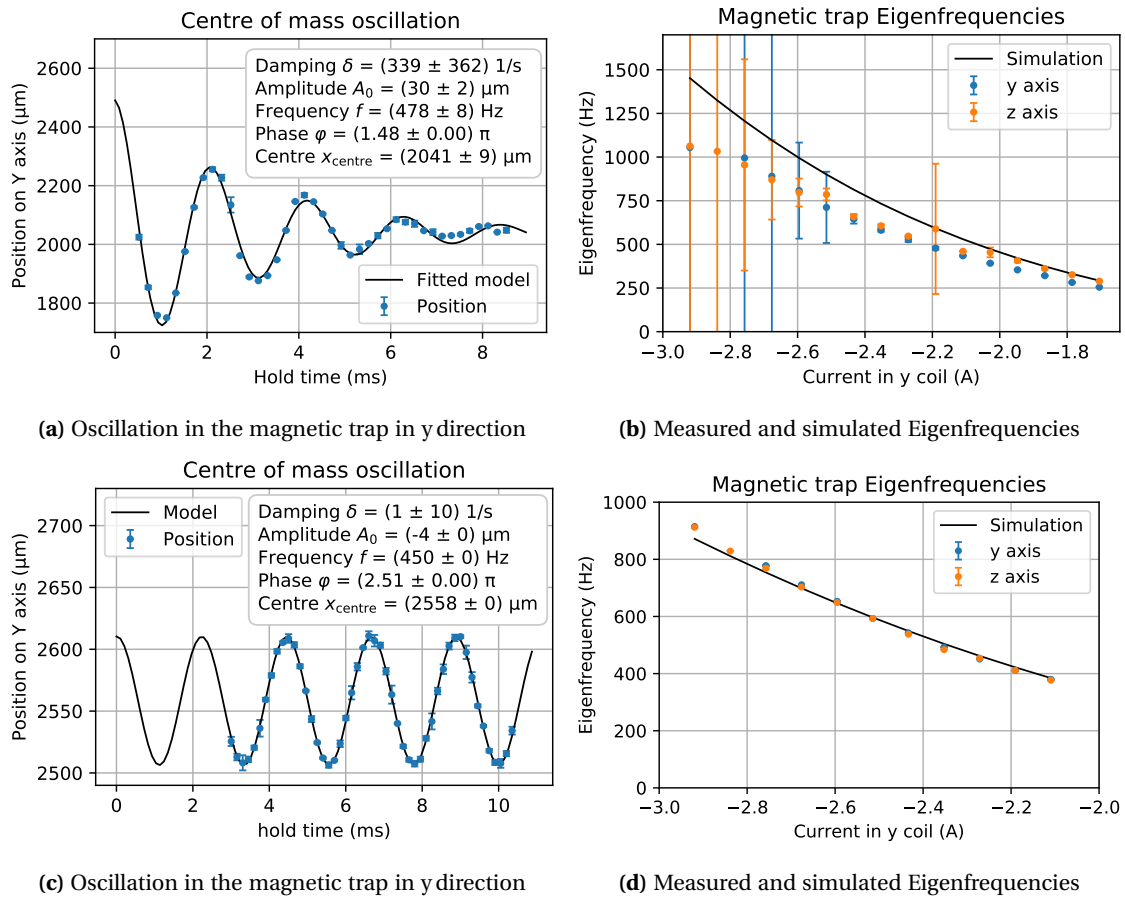


Figure 8.2: Measurement of trap Eigenfrequencies. (a, c) The COM position after a time of flight of $t_{\text{TOF}} = 5$ ms is derived from absorption detection images and is plotted versus the holding time in the trap. The error bars represent the standard deviation of two repetitions. The model described in equation (8.4) has been fitted to the data (black line). (b, d) Determination of the trap Eigenfrequency as in (a) for different offset magnetic fields varying the confinement of the trap. The simulated Eigenfrequency in the strong trap axis is shown as a black line. The measurements (a, b) have been performed with an ensemble at a temperature of (166 ± 6) μK in trap configuration ② and (c, d) at (620 ± 20) nK in trap configuration ③.

The simulated trap Eigenfrequencies are higher than the measurements because the simulation approximates the trap potential at the trap minimum. In [figure 6.2\(b\)](#) the simulated potential is shown as well as the harmonic approximation. The ensemble has a temperature of $(166 \pm 6) \mu\text{K}$. Thus, for atoms with higher energies, the trap has less confinement than the harmonic approximation resulting in lower trap Eigenfrequencies.

Determination of Eigenfrequencies at ultra-cold temperatures

The Eigenfrequency measurement is repeated after the first seven steps of evaporative cooling (see [chapter 9](#)) at a temperature of $(620 \pm 20) \text{nK}$. During optimisation of the evaporative cooling it was shown, that the cooling efficiency improves in a modified trap configuration with a higher magnetic field strength at the trap bottom. These measurements are therefore performed in the compressed trap ③ with parameters given in [table 6.1](#). [Figure 8.2\(c\)](#) shows the oscillation of the ultra-cold ensemble with negligible damping. As the harmonic approximation of the trapping potential has a better agreement with the potential observed by the atoms, the measured trap frequencies summarised in [figure 8.2\(d\)](#) follow the results of the simulation closely. The simulated trap Eigenfrequencies $\omega_{\text{sim}}/2\pi = (22,808,812) \text{Hz}$ have a geometric mean of $\omega_{\text{geo,sim}}/2\pi = 243 \text{Hz}$. The measurement of the Eigenfrequency of the weak axis is not repeated because of technical limitations. It is estimated to be unchanged from the previous value of 20Hz . The geometrical mean of the trap frequencies $\omega_{\text{meas}}/2\pi = (20,915,912) \text{Hz}$ of the compressed trap ③ is $\omega_{\text{geo,meas}}/2\pi = 256 \text{Hz}$.

8.3 Summary

With the procedures outlined in [chapter 7](#), $3.3 \cdot 10^7$ atoms have been transferred to a compressed magnetic trap. The atomic ensemble has a temperature of $166 \mu\text{K}$ and is confined with a geometrically averaged trap frequency of $\omega_{\text{geo,meas}}/2\pi = 256 \text{Hz}$. The trap has a lifetime of 3.2s , which is longer than the anticipated evaporation duration. For comparison, in the MAIUS-A apparatus $1.6 \cdot 10^8$ atoms at a temperature of $110.1 \mu\text{K}$ are confined in the compressed magnetic trap [[Sei14](#)].

CHAPTER 9

Evaporative cooling

Evaporation is a phenomenon that occurs in everyday life. When particles with a kinetic energy above average are able to leave a thermal ensemble, e.g. water molecules leaving a cup of tea as vapour, the remaining ensemble will cool down. The same process can be used to cool a trapped atomic ensemble. The particles in a closed trap elastically collide and exchange momentum, while the overall thermal distribution does not change. The probability density function of the kinetic energy ε of the particles is plotted in [figure 9.1](#). It is proportional to the product of the density of states in the harmonic trap $\rho(\varepsilon) \propto \varepsilon^2$ and the Maxwell-Boltzmann distribution

$$f(\varepsilon) = D \cdot e^{-\varepsilon/(k_B T_{\text{at}})}. \quad (9.1)$$

Here, D is the phase space density (PSD) of the thermal ensemble. When the trap is modified in way that only high energetic particles from the tail of the distribution are able to leave the trap, they remove more energy from the ensemble than the average energy per particle. As the

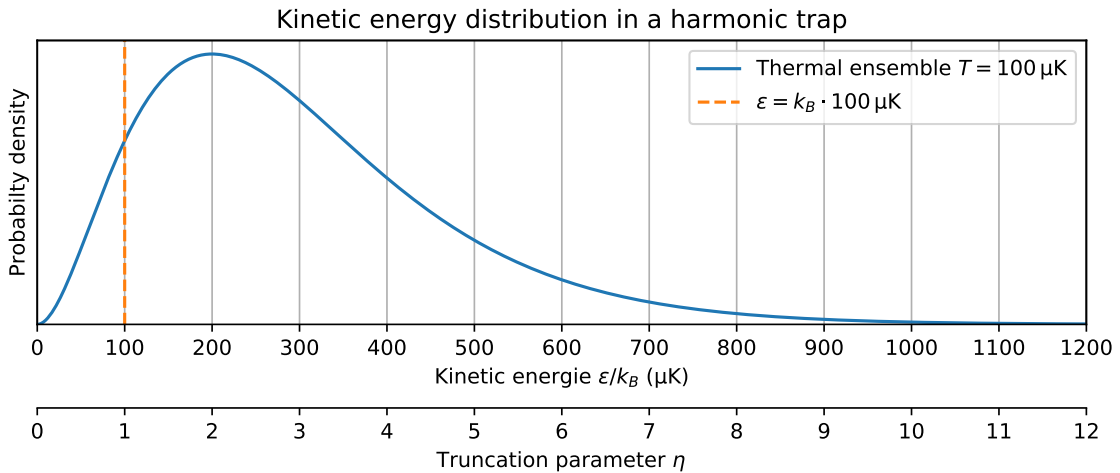


Figure 9.1: Distribution of kinetic energies in an ensemble with temperature $T_{\text{at}} = 100 \mu\text{K}$ in a harmonic trap. The kinetic energy is proportional to the truncation parameter η by $E_{\text{kin}} = \eta k_B T_{\text{at}}$.

remaining particles in the trap rethermalise via elastic collisions, again a Maxwell-Boltzmann distribution is reached with a lower average kinetic energy.

9.1 Radio frequency spectroscopy

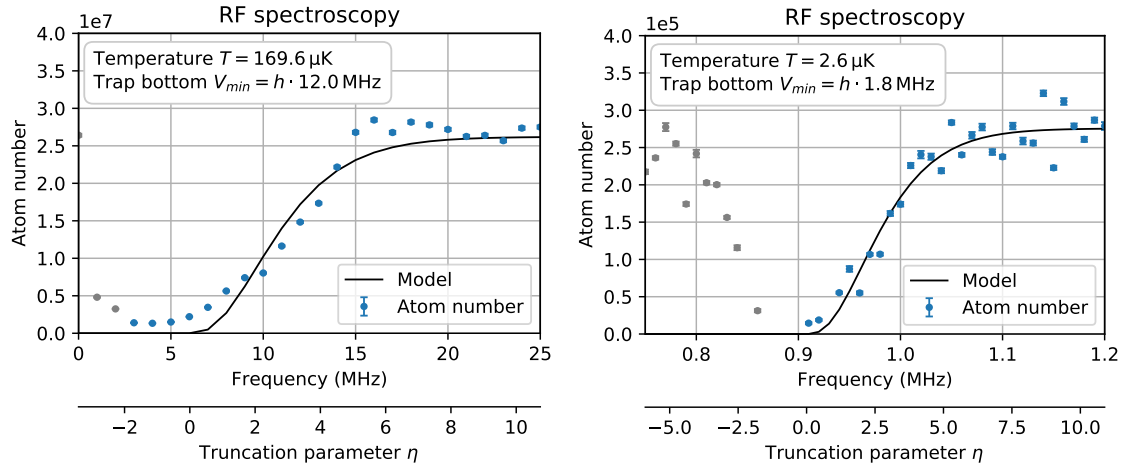
Radio frequency (RF) spectroscopy probes the distribution of kinetic energies in the magnetic trap. By addressing transitions between the magnetic substates with RF radiation, the atoms are pumped to a non-trappable state and are pushed out of the trap. In a magnetic trap, only particles above a certain kinetic energy ε_t can reach a location in the trap \vec{r}_t , where the resonance condition for the transition between two magnetic substates

$$h \cdot f_{\text{knife}} = \mu_B g_F \cdot B(\vec{r}_t) \quad (9.2)$$

is met. The potential at position \vec{r}_t is given by the Zeeman shift

$$V(\vec{r}_t) = \mu_B g_F m_F \cdot B(\vec{r}_t) \quad (9.3)$$

and can only be reached by atoms with a kinetic energy higher than $\varepsilon_t = V(\vec{r}_t)$. This technique is called RF knife, because it cuts away all particles with a kinetic energy higher than the threshold $\varepsilon_t = m_F \cdot h \cdot f_{\text{knife}} - V_{\text{min}}$ from the thermal distribution. Assuming the atoms get



(a) A thermal ensemble after adiabatic compression.

(b) A thermal ensemble after evaporative cooling.

Figure 9.2: RF spectroscopy of the distribution of kinetic energies of the trapped atoms. The atom number has been derived by absorption imaging and is plotted in blue with error bars denoting the uncertainty from fitting a Gaussian shape to the absorption image. The model described by equation (9.4) has been fitted to the data and is depicted as a black line. Measurement points in grey have been excluded from fitting the model.

instantly removed from the trap, the remaining atom number N_r is given by [Sim11, p. 52]

$$N_r = N e^{-\varepsilon_t / (k_B T_{\text{at}})} \left(1 + \frac{\varepsilon_t}{k_B T_{\text{at}}} + \frac{1}{2} \left(\frac{\varepsilon_t}{k_B T_{\text{at}}} \right)^2 \right). \quad (9.4)$$

The parameters temperature T_{at} and trap bottom potential V_{min} of this model are fitted to measurements of the remaining atom number N_r shown in figure 9.2. The RF spectroscopy is performed with a thermal ensemble in the compressed trap configuration ② with parameters given in table 6.1. For comparison the temperature has been determined by a time-of-flight series measurement as described in section 7.3. The derived temperatures are stated in table 9.1. The deviation can be explained by limitations of this model, as it is only valid for a harmonic, isotropic trap and does not include the influence of gravity nor power broadening of the RF frequency.

Table 9.1: Comparison of methods for deriving the temperature.

	After adiabatic compression	After evaporative cooling
RF spectroscopy	169.6 μK	2.6 μK
Time-of-flight series	166 μK	3.3 μK

9.2 Peak density of a Gaussian distribution

In the following, the increase in PSD will be used as a measure to analyse the cooling procedure. The PSD of a thermal ensemble is defined as

$$D = n_0 (\lambda_{\text{th}})^3 \quad (9.5)$$

with the peak density n_0 and the thermal de Broglie wavelength

$$\lambda_{\text{th}} = \sqrt{\frac{2\pi\hbar^2}{m_{\text{at}}k_B T_{\text{at}}}}. \quad (9.6)$$

The peak density of a three-dimensional Gaussian distribution is defined as

$$n_0 = \frac{N}{(2\pi)^{3/2} \sigma_x \sigma_y \sigma_z} \quad (9.7)$$

with the atom number N and the $1/e$ radii σ_i , $i \in (x, y, z)$. In a harmonic potential, the $1/e$ radii of the Gaussian distribution are governed by the atomic mass m_{at} , the temperature T_{at} and the trap frequencies ω_i as follows

$$\sigma_i = \sqrt{\frac{k_B T_{\text{at}}}{m_{\text{at}} (\omega_i)^2}}. \quad (9.8)$$

Using the geometrical mean of the trap frequencies $(\omega_{\text{geo}})^3 = \omega_x \omega_y \omega_z$, the definition of the peak density can be written as

$$n_0 = N (\omega_{\text{geo}})^3 \left(\frac{m_{\text{at}}}{2\pi k_B T_{\text{at}}} \right)^{3/2}. \quad (9.9)$$

Hence, the PSD

$$D = n_0 (\lambda_{\text{dB}})^3 = N \left(\frac{\hbar \omega_{\text{geo}}}{k_B T_{\text{at}}} \right)^3 \quad (9.10)$$

can be calculated from the geometric mean of the trap frequencies (see [section 8.2](#)), the atom number and the temperature. The two latter ones are derived from time-of-flight series as described in [section 7.3](#).

9.3 Optimisation of the forced evaporation procedure

To cool the trapped atomic ensemble, high energy particles are selectively removed from the trap using the RF knife technique. For a constant knife frequency, the rate of cooling eventually slows down, as less and less atoms have a kinetic energy above the threshold. Therefore, *forced evaporation* is realised by adjusting the knife frequency f_{knife} to keep the truncation parameter η constant while the distribution of the ensemble changes. As evaporative cooling naturally happens on an exponential scale, the important properties of the ensemble such as atom number, temperature, density, PSD and the rate of elastic collisions change exponentially. Therefore, also the knife frequency has to follow an exponential curve, which is approximated by eight consecutive linear ramps. The values of these properties are depicted in [figure 9.4](#) for an optimised cooling sequence in the compressed trap configuration ③ with parameters given in [table 6.1](#).

For the optimisation of the ramp slopes, the strategy described in [Ket96, 189ff] was followed. The efficiency of the evaporative cooling

$$\gamma = - \frac{d(\ln D)}{d(\ln N)} \quad (9.11)$$

is determined by acquiring the Phase space density D and the atom number N . The efficiency has to be optimised in every step, to achieve the largest efficiency in total

$$\gamma_{\text{total}} = \frac{\ln(D_{\text{final}}/D_{\text{initial}})}{\ln(N_{\text{final}}/N_{\text{initial}})}. \quad (9.12)$$

The upper limit for the knife frequency change is governed by the rate of elastic collisions. When the knife frequency is changed too fast, the ensemble can not rethermalise in time and atoms are lost without removing thermal energy from the system. On the other hand, atom

loss from background gas collisions gives a lower limit for the knife frequency change.

Figure 9.3 shows the efficiency γ for every step of the evaporative cooling sequence in QG-1 with a duration of 1.3 s. At the end of the sequence, the atom number is reduced by a factor of 3000 while the PSD is increased by six orders of magnitude. The thermal ensemble with 3000 atoms has a temperature of 160 nK and is close to the critical PSD of 1.202 for Bose-Einstein condensation in a three-dimensional harmonic trap, but the atom number is at the limit of the detection system to observe the expansion with a time-of-flight series. The decrease of efficiency towards the end of the sequence can be explained by a too low ratio of elastic to inelastic collisions, defined as the number of elastic collisions per trap lifetime $R = \tau_{\text{loss}}/\tau_{\text{el}}$, leading to decreasing values of R and γ in the subsequent steps [Ket96, p. 192]. This adds to the fact, that under the influence of gravity the effectiveness of the RF knife reduces during the evaporation sequence, because below a limiting temperature the region of resonance is no longer a three-dimensional shell but only a region at the bottom of the trap, where the gravitational potential varies by less than $k_B T_{\text{at}}$ [Ket96, 223f].

It has to be noted, that three-body collisions are another possible cause of a reduced efficiency. They lead to a loss of atom number and heating, because they occur close to the trap minimum where the density is highest and where atoms of the lower-energetic part of the thermal distribution are located. Thus, this process is the reverse of evaporative cooling, because the removed atoms carry away less than the average kinetic energy. This typically leads to a lower limit for the temperature [Ket96, 191f], which has not been observed (see figure 9.4). Furthermore, three-body collisions are expected for densities above 10^{20} m^{-3} while

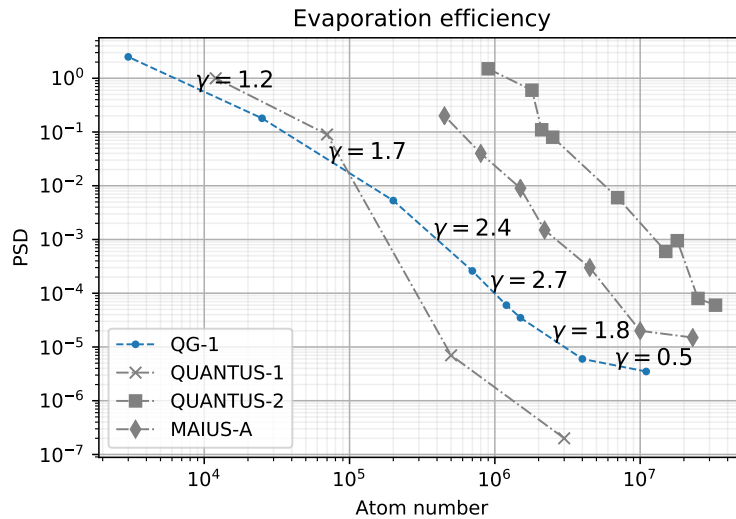


Figure 9.3: The evaporation efficiency γ compares the gain in PSD to the loss of atom number both on an exponential scale (see equation (9.11)). The blue circles depict the atom number and PSD after each step of evaporative cooling in QG-1. For comparison the evaporation process in QUANTUS-1, QUANTUS-2 [Her13] and MAIUS-A [Sei14] is shown in grey.

only a density of $2.5 \cdot 10^{19} \text{ m}^{-3}$ is reached in this work.

The efficiency of the described evaporative cooling sequence needs to be improved to increase the final atom number. To this end, the rate of elastic collisions has to be increased which is achievable with a higher initial atom number as well as with a stronger confinement in the trap. [Figure 9.3](#) shows the evaporation path for the Quantus-1 and Quantus-2 apparatuses which both feature a stronger trap confinement. Within the scope of this thesis, the confinement in the trap is limited by the maximum current of the low noise current driver for the y -component of the offset magnetic field. By replacing the current driver, the efficiency of the evaporative cooling procedure will be improved.

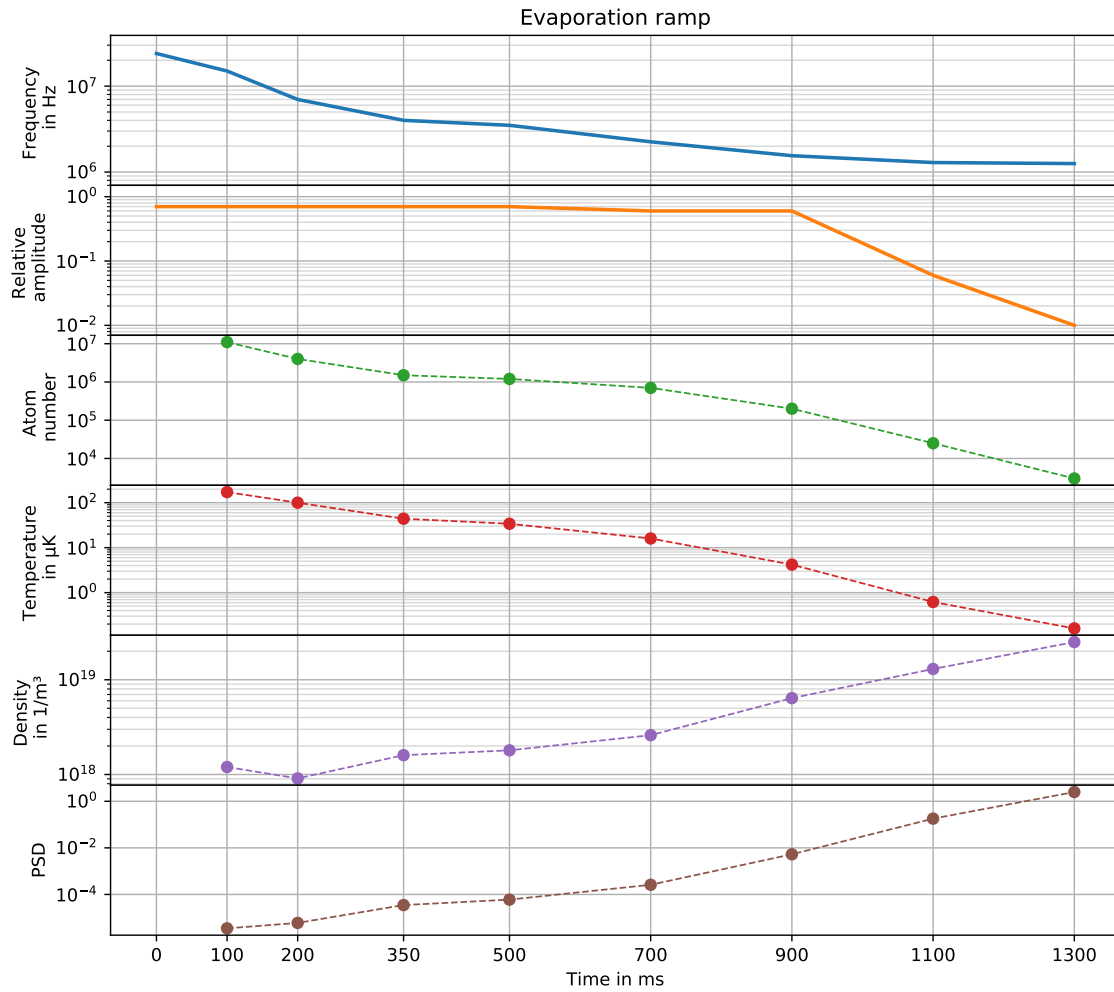


Figure 9.4: Evaporative cooling sequence. Solid lines depict the parameters for the RF knife. Dots represent values derived from a time-of-flight series measurement. The dashed lines are only a guide to the eye.

Part III

Conclusion

CHAPTER 10

Summary and outlook

The main objective of this thesis is the development and assembly of the transportable QG-1 apparatus which will allow to measure gravity with unprecedented accuracy. In [chapter 2](#) it was shown that an ultra-cold atom source is needed to overcome the two main limitations of current generation atom gravimeters. To attain this goal, the established design of an atom-chip-based BEC source pioneered in the QUANTUS collaboration was modified to fulfil the requirements of gravimetry with an instrumental measurement uncertainty below 1 nm/s^2 . Within the scope of this thesis, the gravimeter's sensor head integrating the atom chip source has been designed and assembled with the following key features: The retro-reflection mirror is placed inside the vacuum chamber to eliminate optical elements in the atom interferometer beam path. It is mounted on a custom designed tip/tilt-stage with minimal size and a large dynamic range of up to a hundredfold of the Earth's rotation rate for characterisation. A free optical aperture of 18 mm for the interferometry laser beam is realised by changing the orientation of the atom-chip-based BEC source. This required a new layout of the mesoscopic wire structure of the atom chip. The design, described in [chapter 3](#), features a baseline of 330 mm and a total free fall time of 256 ms for atom interferometry. Furthermore, all components needed for the operation and characterisation of the ultra-cold atom source and the gravimeter have been set up and integrated. These comprise a fibre based laser system ([chapter 4](#)), modular electronics and a computer control system ([chapter 5](#)) that are transportable, compact and robust.

Key result of this thesis is the reliable operation of the ultra-cold atomic source on the atom chip. The mesoscopic wire configuration of the atom chip was modified from the atom chip design of the QUANTUS collaboration and simulations of the corresponding trap properties are summarised in [chapter 6](#). The trap loading procedure was optimised as discussed in [chapter 7](#) and the results show that efficient loading of the magnetic trap with the new mesoscopic wire structure is possible. However, the MOT loading rate has to be optimised to shorten the preparation time. Within 700 ms $3.1 \cdot 10^8$ atoms are loaded in the MOT and subsequently $3.3 \cdot 10^7$ atoms are transferred to the compressed trap. The properties of the compressed trap are reported in [chapter 8](#). The trap has a geometrically averaged trap frequency of $2\pi \cdot 256 \text{ Hz}$ and the trapped ensemble has a lifetime of 3.2 s. As described in [chapter 9](#), the evaporative cooling procedure was started with $3.3 \cdot 10^7$ atoms at a temperature of $166 \mu\text{K}$. 3000 atoms have

been prepared at a temperature of 160 nK and a PSD close to 1.2 at the onset of Bose-Einstein condensation within a total duration of 2.3 s. This represents a very promising milestone towards gravimetry based on BEC interferometry as detailed in [chapter 2](#).

However, it is necessary to improve the evaporative cooling efficiency to reach a higher atom number at the end of the evaporative cooling procedure. Further research conducted by Nina Heine after the final measurements for this thesis showed that the main limitation of the presented design was the maximum output current of one of the current drivers for the offset field coils. It limits the trap confinement which is key for efficient evaporative cooling. This limitation was lifted by adding an additional current driver without changes to the sensor head. As described in [section 3.2](#) the Helmholtz coil pair for the y-component of the magnetic field consists of two individual coil pairs which were previously connected in series to a single low noise current driver which was limited by its maximum output voltage. After connecting each coil pair to a dedicated current driver, the individual low noise current drivers are able to provide a higher output current at a lower voltage. By increasing the y-component of the magnetic offset field a stronger confinement in the magnetic trap was achieved. Subsequently, the atomic ensemble was cooled towards Bose-Einstein condensation and an expanding BEC was observed after release from the trap. In the first realisation of a BEC in QG-1, the duration of the sequence was 2.5 s resulting in $1 \cdot 10^4$ atoms in the condensed fraction¹. A comparable performance to the QUANTUS-2 and MAIUS-A sources, which are based on a similar atom chip design, should be achievable by optimising the loading of the MOT and the evaporative cooling procedure. A comparison is given in [table 10.1](#).

For the gravity measurement, an atom interferometer sensitive to accelerations will be realised in QG-1 with Bragg diffraction on a moving lattice similar to the BEC gravimeter presented in [\[Abe17\]](#). To achieve the goal of the QG-1 gravimeter operating with an instrumental measurement uncertainty below 1 nm/s^2 , the following steps need to be completed.

Table 10.1: Comparison of preparation times and atom numbers of ultra-cold atom sources. The QUANTUS-2 and MAIUS-A sources operate with a similar atom chip setup as QG-1. The CAG gravimeter is stated for reference but operates with an optical dipole trap.

	QUANTUS-2 [Rud15]		MAIUS-A	CAG	QG-1	
	"Case 1"	"Case 3"	[Bec18]	[Kar18]	This work	N. Heine ¹
Atom number	$4 \cdot 10^4$	$4 \cdot 10^5$	$1 \cdot 10^5$	$1 \cdot 10^4$	$3 \cdot 10^3$	$1 \cdot 10^4$
Preparation time	850 ms	1.6 s	1.6 s	4.22 s	2.3 s	2.5 s
Phase	BEC	BEC	BEC	thermal gas	thermal gas	BEC

¹ Source: Private communication with Nina Heine.

Quantum projection noise

In order to be useful in geodetic applications, the gravimeter should reach a statistical uncertainty of $\sigma(\tau_{\text{avg}}) = 10 \text{ nm/s}^2$ within an averaging time of $\tau_{\text{avg}} = 100 \text{ s}$. This is limited by technical noise sources as e.g. the stability of the laser frequencies, environmental noise as e.g. acceleration noise from vibrations and fundamentally by quantum projection noise on the phase read out. The technical and environmental noise needs to be characterised and compensated. However, the quantum projection noise is an intrinsic limit and depends on the atom number N and measurement cycle time τ_{cycle} . The statistical uncertainty is given by

$$\sigma(\tau_{\text{avg}}) = \frac{1}{C\sqrt{N}k_{\text{eff}}T^2} \cdot \sqrt{\frac{\tau_{\text{cycle}}}{\tau_{\text{avg}}}} \quad (10.1)$$

with the interferometer evolution time T , the cycle time τ_{cycle} and the averaging time τ_{avg} . Here, the interferometer contrast is conservatively estimated at $C = 80\%$, although higher contrasts were shown in similar settings. For $2T = 160 \text{ ms}$, $\tau_{\text{cycle}} = 2 \text{ s}$, and $\tau_{\text{avg}} = 100 \text{ s}$, a per shot atom number of $3 \cdot 10^4$ is required to reach the target uncertainty. A comparable atom number to the BEC sources in the QUANTUS collaboration as stated in [table 10.1](#) should be feasible and exceeds the requirement.

Wave front aberrations

A low expansion rate of the atomic wavepacket corresponding to a temperature of 1 nK is crucial for an uncertainty of the wave front aberration bias below 0.2 nm/s^2 as explained in [section 2.4](#). The velocity spread of a BEC is determined by the strength of the trap confinement. A magnetic lens can slow the expansion as mentioned in [section 1.4](#). Expansion rates equivalent to effective temperatures as low as 1 nK have been demonstrated in the QUANTUS-1 apparatus operating on ground [[Kru14](#)].

After reducing the expansion rate, the remaining wave front bias and its uncertainty need to be characterised in QG-1. One approach for the determination of the wave front bias is the variation of the expansion rate of the atomic test mass as described in [[Kar18](#)]. A similar evaluation can be performed in QG-1 by controlling the expansion rate with the parameters of the magnetic lens within a wide range. Another approach is the simulation of the wave front bias based on a map of the wave front as illustrated in [[Sch15](#)]. Given the small size of a BEC compared to the size of the laser beams, the wave front can be mapped by launching the BEC from different trap positions on the atom chip or with different horizontal velocities.

Magnetic field gradients

The atoms released from the magnetic trap are in the magnetic substate $m_F = +2$. To lessen their susceptibility for magnetic fields they have to be prepared in the $m_F = 0$ substate, which is

to the first order unaffected by magnetic fields. This transfer is to be achieved via an adiabatic rapid passage by emitting an RF field from the atom chip as described in [Kru14]. While this technique succeeds to prepare 95 % of all atoms in the non-magnetic $m_F = 0$ substate, the remaining atoms in substates $m_F \neq 0$ are pushed away by a Stern-Gerlach-type deflection [Abe17]. During the interferometer sequence, a magnetisation field with a magnetic field strength of $10 \mu\text{T}$ (100 mG) is needed to prevent spin flips between the magnetic substates. Via the second order Zeeman effect the atoms are still susceptible to magnetic field gradients. The sensor head is equipped with a three-layer magnetic shielding made of mu metal which ensures a homogeneous magnetic environment on the inside (see section 3.7). Additional coils need to be positioned and calibrated to ensure a gradient of the quantisation field of less than $1 \mu\text{T/m}$ (10 mG/m) along the baseline of the atom interferometer which corresponds to a bias below 1 nm/s^2 . The measurement of the magnetic field can be conducted with the atom interferometer itself [Har16].

Characterisation of further systematic biases

As discussed in section 2.3 the susceptibility to rotations has to be characterised and compensated. When the leading order uncertainties of current generation atom gravimeters are reduced below 1 nm/s^2 , other effects become relevant. The influence of the black-body radiation shift in QG-1 caused by a temperature gradient in the sensor head has been simulated in [Hei20]. The gravity measurement bias is estimated at a value of 1 nm/s^2 and it will be characterised with an uncertainty of 0.3 nm/s^2 by monitoring the temperature distribution in the sensor head. The mean field shift related to unequal atom numbers in the two paths of the atom interferometer has been assessed in [Hei20]. For QG-1, an average instability of the splitting ratio of 10^{-4} corresponds to an uncertainty in the determination of gravity of 0.2 nm/s^2 . Furthermore, the influence of light shifts has to be studied. [Gie16] showed that the two-photon light shift for Bragg diffraction with Gaussian temporal pulse shapes and an initial momentum of the atoms is suppressed compared to Raman diffraction. By increasing the initial vertical momentum the effect will become negligible in QG-1.

In summary, the estimates for the error budget and its uncertainties give a perspective on the achievable instrumental measurement uncertainty below 1 nm/s^2 .

Geodetic measurement campaigns

Above all, the functionality of QG-1 needs to be assessed in comparison campaigns with current generation gravimeters. QG-1 is projected to eventually surpass the performance of established instruments. The low instrumental uncertainty will enable field measurements of signals that were previously inaccessible using state-of-the-art gravimeters. It will contribute valuable observations to various fields from volcanology and earthquake research to hydrology and understanding the effects of climate change [Cam17].

Bibliography

- [Abe16] ABEND, S., M. GEBBE, M. GERSEMANN, H. AHLERS, H. MÜNTINGA, E. GIESE, N. GAALOUL, C. SCHUBERT, C. LÄMMERZAHL, W. ERTMER, W. P. SCHLEICH, and E. M. RASEL: ‘Atom-Chip Fountain Gravimeter’. *Physical Review Letters* (Nov. 2016), vol. 117(20). DOI: [10.1103/physrevlett.117.203003](https://doi.org/10.1103/physrevlett.117.203003) (cit. on p. 30).
- [Abe17] ABEND, SVEN: ‘Atom-chip gravimeter with Bose-Einstein condensates’. eng. PhD thesis. 2017. DOI: [10.15488/8921](https://doi.org/10.15488/8921) (cit. on pp. 72, 74).
- [Amm97] AMMANN, HUBERT and NELSON CHRISTENSEN: ‘Delta Kick Cooling: A New Method for Cooling Atoms’. *Physical Review Letters* (Mar. 1997), vol. 78(11): pp. 2088–2091. DOI: [10.1103/physrevlett.78.2088](https://doi.org/10.1103/physrevlett.78.2088) (cit. on p. 4).
- [And95] ANDERSON, M. H., J. R. ENSHER, M. R. MATTHEWS, C. E. WIEMAN, and E. A. CORNELL: ‘Observation of Bose-Einstein Condensation in a Dilute Atomic Vapor’. *Science* (July 1995), vol. 269(5221): pp. 198–201. DOI: [10.1126/science.269.5221.198](https://doi.org/10.1126/science.269.5221.198) (cit. on p. 4).
- [Ant18] ANTONI-MICOLLIER, LAURA and JEAN LAUTIER-GAUD: ‘Gravity imager design review’. en. (2018), vol. DOI: [10.5281/zenodo.2542582](https://doi.org/10.5281/zenodo.2542582) (cit. on p. 4).
- [Bag87] BAGNATO, V. S., G. P. LAFYATIS, A. G. MARTIN, E. L. RAAB, R. N. AHMAD-BITAR, and D. E. PRITCHARD: ‘Continuous Stopping and Trapping of Neutral Atoms’. *Physical Review Letters* (May 1987), vol. 58(21): pp. 2194–2197. DOI: [10.1103/physrevlett.58.2194](https://doi.org/10.1103/physrevlett.58.2194) (cit. on p. 46).
- [Bar18] BARBEY, JAN PHILIPP: ‘Ein Atomchip hohen Flusses für die Quantengravimetrie’. MSc thesis. Leibniz Universität Hannover, 2018 (cit. on p. 47).
- [Bec18] BECKER, DENNIS et al.: ‘Space-borne Bose–Einstein condensation for precision interferometry’. *Nature* (Oct. 2018), vol. 562(7727): pp. 391–395. DOI: [10.1038/s41586-018-0605-1](https://doi.org/10.1038/s41586-018-0605-1) (cit. on pp. 4, 21, 72).
- [Bra95] BRADLEY, C. C., C. A. SACKETT, J. J. TOLLETT, and R. G. HULET: ‘Evidence of Bose-Einstein Condensation in an Atomic Gas with Attractive Interactions’. *Physical Review Letters* (Aug. 1995), vol. 75(9): pp. 1687–1690. DOI: [10.1103/physrevlett.75.1687](https://doi.org/10.1103/physrevlett.75.1687) (cit. on p. 4).

- [Bri06] BRINK, D. M. and C. V. SUKUMAR: ‘Majorana spin-flip transitions in a magnetic trap’. *Physical Review A* (Sept. 2006), vol. 74(3). DOI: [10.1103/physreva.74.035401](https://doi.org/10.1103/physreva.74.035401) (cit. on p. 46).
- [Cam17] CAMP, MICHEL VAN, OLIVIER de VIRON, ARNAUD WATLET, BRUNO MEURERS, OLIVIER FRANCIS, and CORENTIN CAUDRON: ‘Geophysics From Terrestrial Time-Variable Gravity Measurements’. *Reviews of Geophysics* (Nov. 2017), vol. 55(4): pp. 938–992. DOI: [10.1002/2017rg000566](https://doi.org/10.1002/2017rg000566) (cit. on pp. 2, 74).
- [Cha06] CHAUDHURI, SAPTARISHI, SANJUKTA ROY, and C. S. UNNIKRISHNAN: ‘Realization of an intense cold Rb atomic beam based on a two-dimensional magneto-optical trap: Experiments and comparison with simulations’. *Physical Review A* (Aug. 2006), vol. 74(2). DOI: [10.1103/physreva.74.023406](https://doi.org/10.1103/physreva.74.023406) (cit. on p. 21).
- [Coo65] COOK, A H: ‘The Absolute Determination of the Acceleration Due to Gravity’. *Metrologia* (July 1965), vol. 1(3): pp. 84–114. DOI: [10.1088/0026-1394/1/3/003](https://doi.org/10.1088/0026-1394/1/3/003) (cit. on p. 9).
- [Cox92] COX, F.L., W.B. KUHN, J.P. MURRAY, and S.D. TYNOR: ‘Code-level modeling in XSPICE’. *[Proceedings] 1992 IEEE International Symposium on Circuits and Systems*. IEEE, 1992. DOI: [10.1109/iscas.1992.230083](https://doi.org/10.1109/iscas.1992.230083) (cit. on p. 36).
- [Dav95] DAVIS, KENDALL B., MARC-OLIVER MEWES, MICHAEL A. JOFFE, MICHAEL R. ANDREWS, and WOLFGANG KETTERLE: ‘Evaporative Cooling of Sodium Atoms’. *Physical Review Letters* (June 1995), vol. 74(26): pp. 5202–5205. DOI: [10.1103/physrevlett.74.5202](https://doi.org/10.1103/physrevlett.74.5202) (cit. on p. 4).
- [Deb11] DEBS, J. E., P. A. ALTIN, T. H. BARTER, D. DÖRING, G. R. DENNIS, G. McDONALD, R. P. ANDERSON, J. D. CLOSE, and N. P. ROBINS: ‘Cold-atom gravimetry with a Bose-Einstein condensate’. *Physical Review A* (Sept. 2011), vol. 84(3). DOI: [10.1103/physreva.84.033610](https://doi.org/10.1103/physreva.84.033610) (cit. on p. 10).
- [Dra73] DRAKE, STILLMAN: ‘Galileo’s Discovery of the Law of Free Fall’. *Scientific American* (1973), vol. 228(5): pp. 84–93. URL: <http://www.jstor.org/stable/24923051> (cit. on p. 1).
- [Fan16] FANG, B, I DUTTA, P GILLOT, D SAVOIE, J LAUTIER, B CHENG, C L GARRIDO ALZAR, R GEIGER, S MERLET, F PEREIRA DOS SANTOS, and et AL.: ‘Metrology with Atom Interferometry: Inertial Sensors from Laboratory to Field Applications’. *Journal of Physics: Conference Series* (June 2016), vol. 723: p. 012049. DOI: [10.1088/1742-6596/723/1/012049](https://doi.org/10.1088/1742-6596/723/1/012049) (cit. on p. 4).
- [Far14] FARAH, T., C. GUERLIN, A. LANDRAGIN, PH. BOUYER, S. GAFFET, F. PEREIRA DOS SANTOS, and S. MERLET: ‘Underground operation at best sensitivity of the mobile LNE-SYRTE cold atom gravimeter’. *Gyroscopy and Navigation* (Oct. 2014), vol. 5(4): pp. 266–274. DOI: [10.1134/s2075108714040051](https://doi.org/10.1134/s2075108714040051) (cit. on p. 14).

- [Fre16] FREIER, C, M HAUTH, V SCHKOLNIK, B LEYKAUF, M SCHILLING, H WZIONTEK, H-G SCHERNECK, J MÜLLER, and A PETERS: ‘Mobile quantum gravity sensor with unprecedented stability’. *Journal of Physics: Conference Series* (June 2016), vol. 723: p. 012050. DOI: [10.1088/1742-6596/723/1/012050](https://doi.org/10.1088/1742-6596/723/1/012050) (cit. on p. 4).
- [Fry19] FRYE, KAI et al.: ‘The Bose-Einstein Condensate and Cold Atom Laboratory’. (Dec. 10, 2019), vol. (cit. on p. 4).
- [Ger16] GERSEMANN, MATTHIAS: ‘Coherent acceleration of atomic ensembles by optical lattices in quantum sensors’. MSc thesis. Leibniz Universität Hannover, 2016 (cit. on p. 27).
- [Gie16] GIESE, E., A. FRIEDRICH, S. ABEND, E. M. RASEL, and W. P. SCHLEICH: ‘Light shifts in atomic Bragg diffraction’. *Physical Review A* (Dec. 2016), vol. 94(6). DOI: [10.1103/physreva.94.063619](https://doi.org/10.1103/physreva.94.063619) (cit. on p. 74).
- [Gro17] GROVE, NINA: ‘A fiber-based laser system for a transportable quantum gravimeter’. MSc thesis. Leibniz Universität Hannover, 2017 (cit. on pp. 27, 31, 33).
- [Har16] HARDMAN, K. S., P. J. EVERITT, G. D. McDONALD, P. MANJU, P. B. WIGLEY, M. A. SOORIYABANDARA, C. C. N. KUHN, J. E. DEBS, J. D. CLOSE, and N. P. ROBINS: ‘Simultaneous Precision Gravimetry and Magnetic Gradiometry with a Bose-Einstein Condensate: A High Precision, Quantum Sensor’. *Physical Review Letters* (Sept. 2016), vol. 117(13). DOI: [10.1103/physrevlett.117.138501](https://doi.org/10.1103/physrevlett.117.138501) (cit. on p. 74).
- [Hau13] HAUTH, M., C. FREIER, V. SCHKOLNIK, A. SENGER, M. SCHMIDT, and A. PETERS: ‘First gravity measurements using the mobile atom interferometer GAIN’. *Applied Physics B* (Apr. 2013), vol. 113(1): pp. 49–55. DOI: [10.1007/s00340-013-5413-6](https://doi.org/10.1007/s00340-013-5413-6) (cit. on pp. 11, 19).
- [Hei20] HEINE, NINA, JONAS MATTHIAS, MARAL SAHELGOZIN, WALDEMAR HERR, SVEN ABEND, LUDGER TIMMEN, JÜRGEN MÜLLER, and ERNST MARIA RASEL: ‘A transportable quantum gravimeter employing delta-kick collimated Bose-Einstein condensates’. *The European Physical Journal D* (Aug. 2020), vol. 74(8). DOI: [10.1140/epjd/e2020-10120-x](https://doi.org/10.1140/epjd/e2020-10120-x) (cit. on p. 74).
- [Her13] HERR, WALDEMAR: ‘Eine kompakte Quelle quantenentarteter Gase hohen Flusses für die Atominterferometrie unter Schwerelosigkeit’. PhD thesis. Leibniz Universität Hannover, 2013. URL: <https://www.tib.eu/de/suchen/id/TIBKAT:746945310> (cit. on pp. 21, 47, 65).
- [JCG08] JCGM: *Evaluation of measurement data – Guide to the expression of uncertainty in measurement*. JCGM 100:2008. 2008. URL: <https://www.bipm.org/en/publications/guides/gum.html> (cit. on p. 10).

- [Kar18] KARCHER, R, A IMANALIEV, S MERLET, and F PEREIRA DOS SANTOS: ‘Improving the accuracy of atom interferometers with ultracold sources’. *New Journal of Physics* (Nov. 2018), vol. 20(11): p. 113041. DOI: [10.1088/1367-2630/aaf07d](https://doi.org/10.1088/1367-2630/aaf07d) (cit. on pp. 4, 72, 73).
- [Kas92] KASEVICH, M. and S. CHU: ‘Measurement of the gravitational acceleration of an atom with a light-pulse atom interferometer’. *Applied Physics B Photophysics and Laser Chemistry* (May 1992), vol. 54(5): pp. 321–332. DOI: [10.1007/bf00325375](https://doi.org/10.1007/bf00325375) (cit. on pp. 10, 12).
- [Kas91] KASEVICH, MARK and STEVEN CHU: ‘Atomic interferometry using stimulated Raman transitions’. *Physical Review Letters* (July 1991), vol. 67(2): pp. 181–184. DOI: [10.1103/physrevlett.67.181](https://doi.org/10.1103/physrevlett.67.181) (cit. on p. 3).
- [Ket96] KETTERLE, WOLFGANG and N.J. VAN DRUTEN: ‘Evaporative Cooling of Trapped Atoms’. *Advances In Atomic, Molecular, and Optical Physics*. Elsevier, 1996: pp. 181–236. DOI: [10.1016/s1049-250x\(08\)60101-9](https://doi.org/10.1016/s1049-250x(08)60101-9) (cit. on pp. 64, 65).
- [Kna13] KNAAK, KAI-MARTIN: *Photodiodenverstärker 20 MHz AC + DC Version 6*. 2013. URL: https://elektronik.iqo.uni-hannover.de/index.html/doku.php?id=eigenbau:photodiode:photodiodenverstaerker_20_mhz:start (cit. on p. 32).
- [Kru14] KRUTZIK, MARKUS: ‘Matter wave interferometry in microgravity’. PhD thesis. Humboldt-Universität zu Berlin, Mathematisch-Naturwissenschaftliche Fakultät I, 2014. DOI: <http://dx.doi.org/10.18452/17050> (cit. on pp. 4, 13, 73, 74).
- [Lau14] LAUTIER, J., L. VOLODIMER, T. HARDIN, S. MERLET, M. LOURS, F. PEREIRA DOS SANTOS, and A. LANDRAGIN: ‘Hybridizing matter-wave and classical accelerometers’. *Applied Physics Letters* (Oct. 2014), vol. 105(14): p. 144102. DOI: [10.1063/1.4897358](https://doi.org/10.1063/1.4897358) (cit. on p. 14).
- [Lib93] LIBBRECHT, K. G. and J. L. HALL: ‘A low-noise high-speed diode laser current controller’. *Review of Scientific Instruments* (Aug. 1993), vol. 64(8): pp. 2133–2135. DOI: [10.1063/1.1143949](https://doi.org/10.1063/1.1143949) (cit. on p. 32).
- [Lou11] LOUCHET-CHAUVET, ANNE, TRISTAN FARAH, QUENTIN BODART, ANDRÉ CLAIRON, ARNAUD LANDRAGIN, SÉBASTIEN MERLET, and FRANCK PEREIRA DOS SANTOS: ‘The influence of transverse motion within an atomic gravimeter’. *New Journal of Physics* (June 2011), vol. 13(6): p. 065025. DOI: [10.1088/1367-2630/13/6/065025](https://doi.org/10.1088/1367-2630/13/6/065025) (cit. on pp. 4, 12, 13, 23).
- [Mac12] MACDOUGAL, DOUGLAS W.: ‘Galileo’s Great Discovery: How Things Fall’. *Newton’s Gravity*. Springer New York, 2012: pp. 17–36. DOI: [10.1007/978-1-4614-5444-1_2](https://doi.org/10.1007/978-1-4614-5444-1_2) (cit. on p. 1).

- [Mén18] MÉNORET, VINCENT, PIERRE VERMEULEN, NICOLAS LE MOIGNE, SYLVAIN BONVALOT, PHILIPPE BOUYER, ARNAUD LANDRAGIN, and BRUNO DESRUELLE: ‘Gravity measurements below 10⁻⁹ g with a transportable absolute quantum gravimeter’. *Scientific Reports* (Aug. 2018), vol. 8(1). DOI: [10.1038/s41598-018-30608-1](https://doi.org/10.1038/s41598-018-30608-1) (cit. on p. 3).
- [Mer10] MERLET, SÉBASTIEN: ‘Absolute determination of g in the frame of the watt balance experiment’. Theses. Observatoire de Paris, July 2010. URL: <https://tel.archives-ouvertes.fr/tel-00517127> (cit. on p. 18).
- [Moo09] MOORE, JOHN H., CHRISTOPHER C. DAVIS, MICHAEL A. COPLAN, and SANDRA C. GREER: *Building Scientific Apparatus*. Cambridge University Press, 2009. DOI: [10.1017/cbo9780511609794](https://doi.org/10.1017/cbo9780511609794) (cit. on p. 91).
- [Mün13] MÜNTINGA, H. et al.: ‘Interferometry with Bose-Einstein Condensates in Microgravity’. *Physical Review Letters* (Feb. 2013), vol. 110(9). DOI: [10.1103/physrevlett.110.093602](https://doi.org/10.1103/physrevlett.110.093602) (cit. on p. 4).
- [muQ19] MUQUANS: *Absolute Quantum Gravimeter Datasheet*. Mar. 2019. URL: https://www.muquans.com/wp-content/uploads/2019/03/muquans_aqg.pdf (cit. on p. 4).
- [Myr00] MYRSKOG, S. H., J. K. FOX, H. S. MOON, J. B. KIM, and A. M. STEINBERG: ‘Modified “ δ -kick cooling” using magnetic field gradients’. *Physical Review A* (Apr. 2000), vol. 61(5). DOI: [10.1103/physreva.61.053412](https://doi.org/10.1103/physreva.61.053412) (cit. on p. 4).
- [Nag73] NAGEL, LAURENCE W. and D.O. PEDERSON: *SPICE (Simulation Program with Integrated Circuit Emphasis)*. Tech. rep. UCB/ERL M382. EECS Department, University of California, Berkeley, Apr. 1973. URL: <http://www2.eecs.berkeley.edu/Pubs/TechRpts/1973/22871.html> (cit. on p. 36).
- [Pet01] PETERS, A, K Y CHUNG, and S CHU: ‘High-precision gravity measurements using atom interferometry’. *Metrologia* (Feb. 2001), vol. 38(1): pp. 25–61. DOI: [10.1088/0026-1394/38/1/4](https://doi.org/10.1088/0026-1394/38/1/4) (cit. on p. 11).
- [Pop18] POPP, MANUEL ANDRÉ: ‘Compact, low-noise current drivers for quantum sensors with atom chips’. PhD thesis. Leibniz Universität Hannover, 2018. DOI: [10.15488/3688](https://doi.org/10.15488/3688) (cit. on pp. 35–37).
- [Pri83] PRITCHARD, DAVID E.: ‘Cooling Neutral Atoms in a Magnetic Trap for Precision Spectroscopy’. *Physical Review Letters* (Oct. 1983), vol. 51(15): pp. 1336–1339. DOI: [10.1103/physrevlett.51.1336](https://doi.org/10.1103/physrevlett.51.1336) (cit. on p. 46).
- [Raa87] RAAB, E. L., M. PRENTISS, ALEX CABLE, STEVEN CHU, and D. E. PRITCHARD: ‘Trapping of Neutral Sodium Atoms with Radiation Pressure’. *Physical Review Letters* (Dec. 1987), vol. 59(23): pp. 2631–2634. DOI: [10.1103/physrevlett.59.2631](https://doi.org/10.1103/physrevlett.59.2631) (cit. on p. 3).

- [Rei02] REICHEL, J.: 'Microchip traps and Bose-Einstein condensation'. *Applied Physics B: Lasers and Optics* (Apr. 2002), vol. 74(6): pp. 469–487. DOI: [10.1007/s003400200861](https://doi.org/10.1007/s003400200861) (cit. on p. 46).
- [Rei99] REICHEL, J., W. HÄNSEL, and T. W. HÄNSCH: 'Atomic Micromanipulation with Magnetic Surface Traps'. *Physical Review Letters* (Oct. 1999), vol. 83(17): pp. 3398–3401. DOI: [10.1103/physrevlett.83.3398](https://doi.org/10.1103/physrevlett.83.3398) (cit. on p. 22).
- [Rei11] REICHEL, JAKOB and VLADAN VULETIĆ, eds.: *Atom Chips*. Wiley-VCH Verlag GmbH & Co. KGaA, Feb. 2011. DOI: [10.1002/9783527633357](https://doi.org/10.1002/9783527633357) (cit. on pp. 46, 48, 55).
- [Rot12] ROTHLEITNER, CH. and S. SVITLOV: 'On the evaluation of systematic effects in atom and corner-cube absolute gravimeters'. *Physics Letters A* (Feb. 2012), vol. 376(12-13): pp. 1090–1095. DOI: [10.1016/j.physleta.2012.02.019](https://doi.org/10.1016/j.physleta.2012.02.019) (cit. on p. 9).
- [Rud15] RUDOLPH, JAN, WALDEMAR HERR, CHRISTOPH GRZESCHIK, TAMMO STERNKE, ALEXANDER GROTE, MANUEL POPP, DENNIS BECKER, HAUKE MÜNTINGA, HOLGER AHLERS, ACHIM PETERS, CLAUS LÄMMERZAHN, KLAUS SENGSTOCK, NACEUR GAALLOUL, WOLFGANG ERTMER, and ERNST M RASEL: 'A high-flux BEC source for mobile atom interferometers'. *New Journal of Physics* (June 2015), vol. 17(6): p. 065001. DOI: [10.1088/1367-2630/17/6/065001](https://doi.org/10.1088/1367-2630/17/6/065001) (cit. on pp. 4, 14, 21, 72).
- [Sah19] SAHELGOZIN, MARAL: 'Design and construction of a transportable quantum gravimeter and realization of an atom-chip magnetic trap'. eng. PhD thesis. 2019. DOI: [10.15488/5055](https://doi.org/10.15488/5055) (cit. on pp. 21, 23, 51, 52).
- [Sch15] SCHKOLNIK, V., B. LEYKAUF, M. HAUTH, C. FREIER, and A. PETERS: 'The effect of wavefront aberrations in atom interferometry'. *Applied Physics B* (June 2015), vol. 120(2): pp. 311–316. DOI: [10.1007/s00340-015-6138-5](https://doi.org/10.1007/s00340-015-6138-5) (cit. on pp. 4, 23, 73).
- [Sch17] SCHKOLNIK, VLADIMIR: *Probing gravity with quantum sensors*. 2017. DOI: [10.18452/17676](https://doi.org/10.18452/17676) (cit. on pp. 14, 18).
- [Sei14] SEIDEL, STEPHAN TOBIAS: 'Eine Quelle für die Interferometrie mit Bose-Einstein-Kondensaten in Höhenforschungsraketen'. PhD thesis. Leibniz Universität Hannover, 2014. DOI: [10.15488/8368](https://doi.org/10.15488/8368) (cit. on pp. 21, 55, 56, 60, 65).
- [Sim11] SIMONET, JULIETTE: 'Optical traps for Ultracold Metastable Helium atoms'. Theses. Université Pierre et Marie Curie - Paris VI, Mar. 2011. URL: <https://hal.archives-ouvertes.fr/tel-00651592/en/> (cit. on p. 63).
- [Ste15] STECK, DANIEL A.: *Rubidium 87 D Line Data*. revision 2.1.5, 13 January 2015. Jan. 2015. URL: <http://steck.us/alkalidata> (cit. on p. 46).
- [Szi12] SZIGETI, S S, J E DEBS, J J HOPE, N P ROBINS, and J D CLOSE: 'Why momentum width matters for atom interferometry with Bragg pulses'. *New Journal of Physics* (Feb. 2012), vol. 14(2): p. 023009. DOI: [10.1088/1367-2630/14/2/023009](https://doi.org/10.1088/1367-2630/14/2/023009) (cit. on p. 14).

- [Tex08] TEXAS INSTRUMENTS: *Getting Started with TINA-TI: A Quick Start Guide*. 2008. URL: <http://www.ti.com/tool/TINA-TI> (cit. on p. 36).
- [Tim11] TIMMEN, LUDGER, OLGA GITLEIN, VOLKER KLEMMANN, and DETLEF WOLF: ‘Observing Gravity Change in the Fennoscandian Uplift Area with the Hanover Absolute Gravimeter’. *Pure and Applied Geophysics* (Sept. 2011), vol. 169(8): pp. 1331–1342. DOI: [10.1007/s00024-011-0397-9](https://doi.org/10.1007/s00024-011-0397-9) (cit. on p. 2).
- [Wes17] WESCHE, JANNIK: ‘Entwicklung und Charakterisierung eines Abbildungssystems für die Absorptionsdetektion’. BSc thesis. Leibniz Universität Hannover, 2017 (cit. on p. 25).
- [Wik19] WIKIPEDIA: *atan2*. 2019. URL: <https://en.wikipedia.org/wiki/Atan2> (cit. on p. 53).
- [Wil04] WILDERMUTH, S., P. KRÜGER, C. BECKER, M. BRAJDIC, S. HAUPT, A. KASPER, R. FOLMAN, and J. SCHMIEDMAYER: ‘Optimized magneto-optical trap for experiments with ultracold atoms near surfaces’. *Physical Review A* (Mar. 2004), vol. 69(3). DOI: [10.1103/physreva.69.030901](https://doi.org/10.1103/physreva.69.030901) (cit. on pp. 21, 22).
- [Zee97] ZEEMAN, P.: ‘VII. Doublets and triplets in the spectrum produced by external magnetic forces’. *The London, Edinburgh, and Dublin Philosophical Magazine and Journal of Science* (July 1897), vol. 44(266): pp. 55–60. DOI: [10.1080/14786449708621028](https://doi.org/10.1080/14786449708621028) (cit. on p. 45).

List of Figures

2.1	Common mode wave front aberrations and radius of curvature	12
3.1	Sensor head.	17
3.2	Mirror holder assembly.	19
3.3	Arrangement of the three piezo stacks and the reference mirror.	20
3.4	Double MOT vacuum chamber.	21
3.5	Reflection of optical laser beams on the atom chip surface.	22
3.6	Interferometry laser beam path inside the sensor head.	23
3.7	Simplified sketch of the magnetic shield design	25
3.8	Measurement of the magnetic field components inside the magnetic shield. . .	26
4.1	Simplified diagram of the ECDL laser and spectroscopy module.	27
4.2	Overview of the laser frequencies for the operation of the QG-1 gravimeter. . . .	28
4.3	Simplified diagram of the laser system	29
5.1	Linear spectral density of the in-loop beat note frequency signal.	33
5.2	Step response of the unipolar chip current drivers.	38
5.3	Step response of the bipolar coil current drivers with Helmholtz coil pairs. . . .	39
5.4	Step response of the bipolar coil current drivers with small coil pairs.	40
6.1	Layers of the atom chip.	47
6.2	Numerical simulation of the trap potential	49
7.1	Atom number in the initial magnetic trap after optical pumping.	52
7.2	Centre of mass (COM) oscillation after loading the initial magnetic trap.	53
7.3	Temperature determination of the atomic ensemble.	54
7.4	Characterisation of the magnetic trap loading efficiency.	55
8.1	Lifetime measurement of the atomic ensemble in the magnetic trap.	57
8.2	Measurement of trap Eigenfrequencies.	59
9.1	Distribution of kinetic energies in a thermal ensemble in a harmonic trap. . . .	61
9.2	RF spectroscopy of the distribution of kinetic energies.	62
9.3	Evaporation efficiency γ for each evaporative cooling step.	65

9.4	Evaporative cooling sequence.	67
A.1	Flatness measurement of substrate #2.	89
A.2	Flatness measurement of the central region of substrate #2.	90

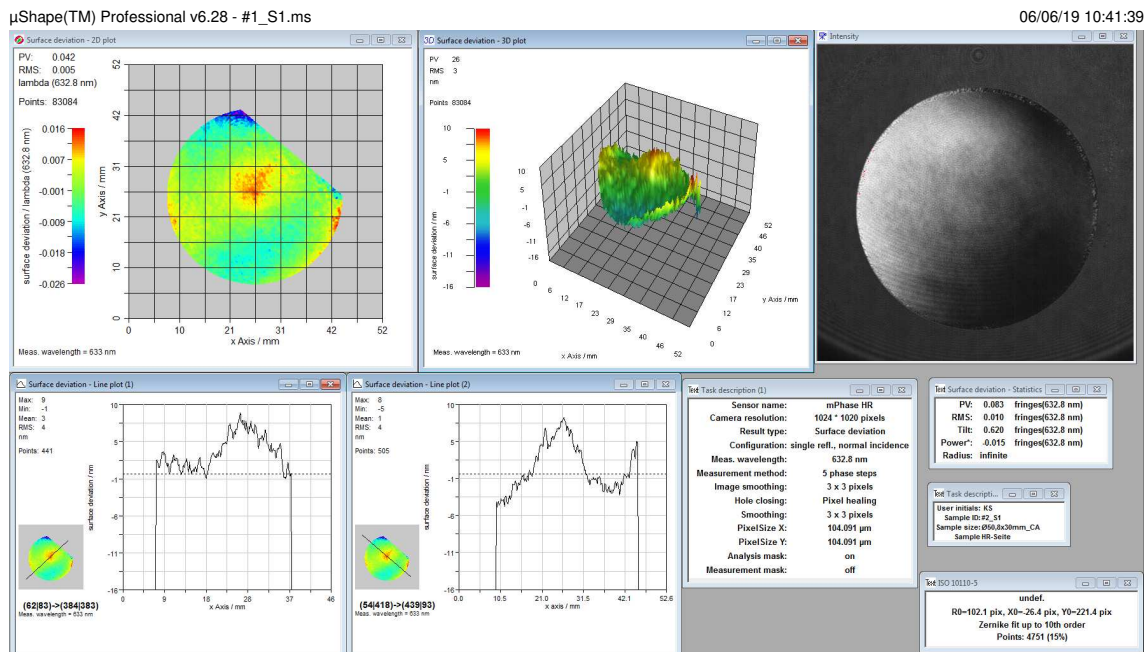
List of Tables

5.1	Number of windings for different configurations of the Helmholtz coil pairs. . .	36
6.1	Input and output parameters of the magnetic trap simulation.	49
9.1	Comparison of methods for deriving the temperature.	63
10.1	Comparison of preparation times and atom numbers of ultra-cold atom sources.	72
A.1	Calculation of the pump speed in the vacuum system.	91

A Appendix

A.1 Mirror surface flatness measurements

Below, the measurement protocols from Laseroptik Garbsen are included. The mirror substrate [Laseroptik Garbsen, S-05487-01] with an ion beam sputtering (IBS) dielectric coating [Laseroptik Garbsen, 26015ke2] has been characterised with an optical interferometer [TRIOPTICS, μ Phase plano down]. The author would like to thank Konrad Schrader from Laseroptik Garbsen for his support and for performing the measurements.



© TRIOPTICS Berlin GmbH

Laseroptik GmbH

Figure A.1: Flatness measurement of substrate #2. Areas with a phase jump in the observed fringe pattern have been excluded and only an area of 35 mm diameter has been evaluated.

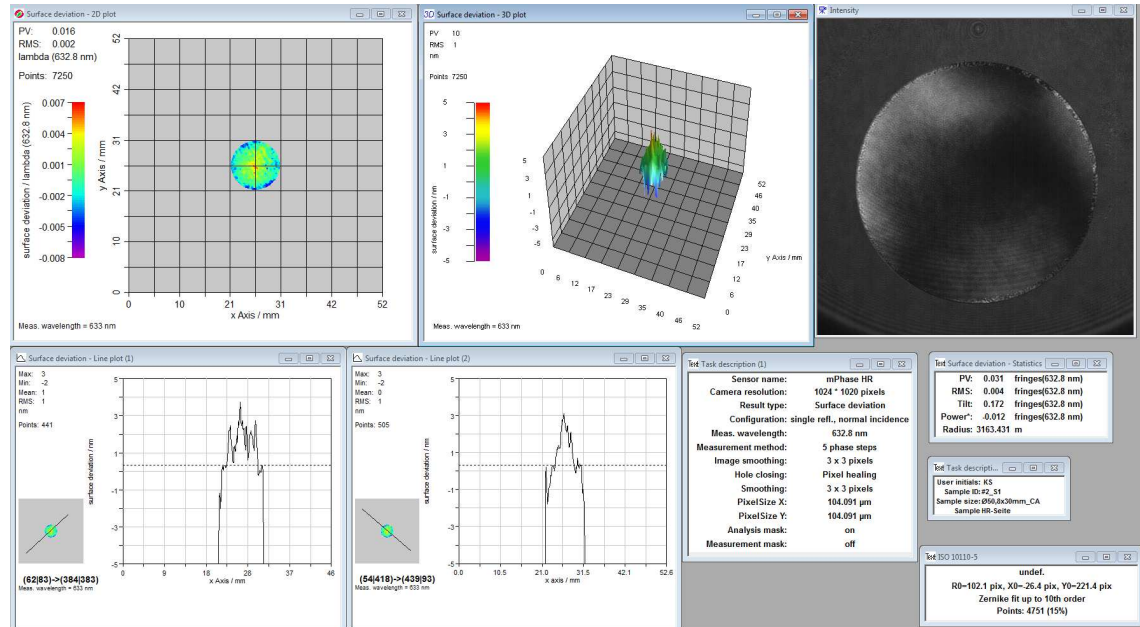


Figure A.2: Flatness measurement of substrate #2. Only the central region with a diameter of 10 mm has been evaluated.

A.2 Ultra-high vacuum initialisation

During the initialisation of the ultra-high vacuum (UHV) in the sensor head, a turbo-molecular pump was attached and the vacuum chamber was heated to 80 °C to accelerate the out-gassing of residual gas particles especially water absorbed by the surfaces of the vacuum chamber. Typically, UHV chambers are heated to temperatures above 100 °C for initialisation, but the indium sealings used for the viewports prevent temperatures higher than 80 °C. Instead, the bake-out time was extended to several weeks.

The target pressure of $10 \cdot 10^{-10}$ hPa could not be reached without keeping the turbo-molecular pump attached. This is usually caused by an insufficient pump speed compared to the outgassing rate. A high out-gassing rate can be caused by the epoxy glue used in the atom chip and the tip/tilt mount for the reference mirror at the bottom of the vacuum system. As the regular vacuum pumps are attached at the top the pump speed is limited by the conduction of the vacuum chamber. The results of a simple estimation of the conductance of the QG-1 vacuum system following the conductance formulae given in [Moo09, 96f] are stated in [table A.1](#).

Table A.1: Calculation of the pump speed at the bottom of the vacuum system of the vacuum pumps located at the top.

	Ion getter pump (IGP)	Non-evaporable getter (NEG)
Nominal pump speed	5 l/s	200 l/s
Pump speed in the mirror chamber	3.5 l/s	18.4 l/s

As a provisional mitigation, the pump speed was increased by an additional IGP Varian, VacIon Plus 20 Noble Diode 919-1124 with 20 l/s pump speed at the site of the free-fall tube located at bottom of the vacuum system. After the final bake-out over 12 days, the target pressure of $10 \cdot 10^{-10}$ hPa was reached. In the following months, the pressure decreased continuously and fell below the measurement range of the vacuum gauge with less than $10 \cdot 10^{-11}$ hPa after 18 months. This indicates a decreasing out-gassing rate. The provisional IGP needs to be detached from the vacuum chamber in order to close the magnetic shield. As this requires breaking the UHV seal it will again lead to the absorption of gases on the vacuum chamber surface. To avoid recurring problems with a too low pump speed, the provisional pump could be replaced by a non-magnetic NEG which can be enclosed in the magnetic shield.

Publications in peer-reviewed journals

1. HEINE, NINA, **JONAS MATTHIAS**, MARAL SAHELGOZIN, WALDEMAR HERR, SVEN ABEND, LUDGER TIMMEN, JÜRGEN MÜLLER, and ERNST MARIA RASEL: 'A transportable quantum gravimeter employing delta-kick collimated Bose–Einstein condensates'. *The European Physical Journal D* (Aug. 2020), vol. 74(8). DOI: [10.1140/epjd/e2020-10120-x](https://doi.org/10.1140/epjd/e2020-10120-x).

Curriculum Vitae

Zur Person

Name Jonas Matthias
geboren am 29.07.1985 in Hannover

Ausbildung

2005 Abitur, Gymnasium Bad Nenndorf

10/2005 – 8/2013 Studium der Physik, Leibniz Universität Hannover

Thema der Diplomarbeit: 'Analyse einer optischen Dipolfalle für Kalium und Rubidium als Quelle für die Atominterferometrie', durchgeführt am Institut für Quantenoptik

9/2013 – heute Promotionsstudium Physik, Leibniz Universität Hannover

Anstellungen

9/2013 – 7/2019 Wissenschaftlicher Mitarbeiter, Institut für Quantenoptik, Leibniz Universität Hannover

8/2019 – heute Data Analyst, Graphmasters GmbH, Hannover

Danksagung

Diese Arbeit ist durch viele Menschen geprägt, von denen ich lernte und die mich unterstützten. Vielen Dank.

Ich danke meinen Kolleginnen Maral und Nina für die Zeit, die wir gemeinsam an QG-1 gearbeitet haben. Danke an Maral, die den Aufbau gemeinsam mit mir begonnen hat. Und danke an Nina, die fast von Anfang an, zunächst als Hiwi, dabei war und nun als Doktorandin das Projekt übernommen hat. Danke an die Studierenden, die im Rahmen ihrer Bachelor-, Masterarbeit und/oder als Hiwi zu QG-1 beigetragen haben: Waldemar F., Philipp, Janina, Tobias, Allen und Jannik.

Weiterhin danke ich Ernst für die Möglichkeit in seiner Arbeitsgruppe zu promovieren. Danke an Ernst, Jürgen, Gunnar und Waldemar, die das Projekt Quantengravimeter ersonnen und Forschungsgelder beantragt haben. Ich danke Ernst, Gunnar, Waldemar und Sven für die Betreuung und all die Anregungen und die Erfahrung, die zu QG-1 beigetragen haben. Vielen Dank an Ludger für spannende Gespräche über Gravimeter.

Ein großer Dank geht an die AG Rasel für die Zusammenarbeit und die Arbeitsatmosphäre, in der man jeden um Rat fragen kann. Danke an Baptist und Jung-Bin für die Zusammenarbeit im Reinraum. Danke an Sven, Matthias, Hendrik, es war mir eine Ehre mit euch ein Labor zu teilen. Danke an Étienne, Christian M., Dorothee und Bob für die gute Labornachbarschaft. Danke an Sebastian für die Labview-Unterstützung und für die Möglichkeit, seine Experimentsteuerung als Vorlage zu nehmen. Danke an Thijs, Manuel, Wolfgang und Alex für das Bestellen und Bereitstellen zahlreicher Elektronik-Module und den Support. Danke an Maike, Baptist und Stephan für den Austausch über MAIUS.

Ich danke der Arbeitsgruppe von Christian Ospelkaus, mit der wir uns den Reinraum im LNQE teilen und insbesondere Martina und Amado für die Unterstützung in der Chip-Anfertigung.

Den Mitarbeitenden der Feinmechanikwerkstatt danke ich für die Geduld beim Besprechen von CAD-Zeichnungen und die vielen gefertigten Einzelteile, die nun ein ganzes Experiment ergeben. Danke an Alex für das aufwendige Fräsen der Vakuumkammer. Danke an Kai-Martin, der die Elektronikwerkwerkstatt betreut und fast immer mit einem Ratschlag zur Stelle ist.

Vielen Dank an Nina, Waldemar, meiner Tante Annemarie, Hendrik, Jonas B., Matthias und Ernst für Kommentare, Rat und kritischen Anmerkungen zum Entwurf dieser Dissertation. Insbesondere danke an Nina, für die Unterstützung und motivierende Gespräche.

Meinen Eltern und Steffen und Tini danke ich für die lebenslange Unterstützung und das Interesse an meiner Arbeit.

Und am Wichtigsten: Danke an Steffi, Jonathan und Samuel, dass es euch gibt, dass ihr für mich da seid und mich auch manchmal von der Doktorarbeit abgelenkt habt. Ihr seid wunderbar.

Danke.

